



Magneto-optical and microscopic properties of organo lead halide perovskites

Krzysztof Galkowski

► To cite this version:

Krzysztof Galkowski. Magneto-optical and microscopic properties of organo lead halide perovskites. Material chemistry. Université Paul Sabatier - Toulouse III, 2017. English. NNT : 2017TOU30265 . tel-01941070

HAL Id: tel-01941070

<https://theses.hal.science/tel-01941070>

Submitted on 30 Nov 2018

HAL is a multi-disciplinary open access archive for the deposit and dissemination of scientific research documents, whether they are published or not. The documents may come from teaching and research institutions in France or abroad, or from public or private research centers.

L'archive ouverte pluridisciplinaire **HAL**, est destinée au dépôt et à la diffusion de documents scientifiques de niveau recherche, publiés ou non, émanant des établissements d'enseignement et de recherche français ou étrangers, des laboratoires publics ou privés.



THÈSE

En vue de l'obtention du

DOCTORAT DE L'UNIVERSITÉ DE TOULOUSE

Délivré par :

Université Toulouse 3 Paul Sabatier (UT3 Paul Sabatier)

Cotutelle internationale avec Uniwersytet Warszawski, Varsovie, Pologne

Présentée et soutenue par :
Krzysztof Gałkowski

le jeudi 12 janvier 2017

Titre :

Magneto-optical and microscopic properties of organo lead halide perovskites

Propriétés magnéto-optiques et microscopiques de perovskites organique -
halogénure de plomb

École doctorale et discipline ou spécialité :

ED SDM : Physique de la matière - CO090

Unité de recherche :

Laboratoire National des Champs Magnétiques Intenses (UPR 3228)

Directeur/trice(s) de Thèse :

Paulina PŁOCHOCKA-MAUDE
Piotr KOSSACKI

Jury :

Adnen MLAYAH	Président du Jury
Jacky EVEN	Rapporteur
Jacek KOSSUT	Rapporteur
Paulina PŁOCHOCKA-Maude	Directrice de Thèse
Piotr KOSSACKI	Co-Directeur de Thèse
Adam BABIŃSKI	Invité
Krzysztof DOROBA	Invité

Auteur: Krzysztof Gałkowski

Titre: Propriétés magnéto-optiques et microscopiques de perovskites organique – halogénure de plomb

Directeurs de Thèse: Paulina PLOCHOCKA-MAUDE et Piotr KOSSACKI

Spécialité: Physique de la matière

Résumé

Les perovskites hybrides organique-halogénure de plomb représentent une classe de matériaux émergents, proposés en tant qu'absorbeur de lumière dans le cadre d'une nouvelle génération de cellules solaires. La formule chimique de ces composés est ABX₃, où A est un cation organique, X représente un anion halogénure (normalement Cl-, Br-, ou I-, ou alors un alliage composé par ces éléments). Les perovskite hybrides combinent d'excellentes propriétés d'absorption avec une grande longueur de diffusion et des longues durée de vie des porteurs de charge, ce qui permet d'atteindre des efficacités de conversion de photons de 22%. Un autre avantage est représenté par leur bas coût de fabrication. Par conséquent, avec le développement de cette classe de matériaux, le photovoltaïque basé sur les perovskites sera potentiellement capable d'améliorer fortement les performances de la technologie photovoltaïque actuelle, basée sur le silicium.

Dans cette thèse, nous utilisons des méthodes optiques pour étudier les propriétés électroniques de base et la morphologie de couches minces de plusieurs représentants des perovskites. Nous étudions notamment des composés ayant le methylammonium et le formamidinium en tant que cations organiques ainsi que les iodures et les bromures à large bande interdite et nous montrons comment la composition chimique influence les paramètres étudiés.

Par magnéto-transmission, nous déterminons directement l'énergie de liaison de l'exciton et sa masse réduite. Nous trouvons que les énergies de liaison à T = 2K sont comprises de 14 à 25 meV, plus petites ou comparables à l'énergie thermique moyenne à la température ambiante (25meV). De plus, ces valeurs diminuent à T=160K jusqu'à 10-24meV. Suite à ces résultats, nous concluons que les porteurs photocréés dans les perovskites peuvent être considérés ionisés thermiquement à la température ambiante. Les valeurs de masse effective sont comprises entre 0.09-0.13 de la masse de l'électron libre. Nous montrons également que l'énergie de liaison de l'exciton ainsi que la masse effective dépendent linéairement de la valeur de la bande interdite. Nos résultats permettent donc d'estimer la valeur de ces paramètres des nouveaux composés perovskites.

Nous avons étudié la morphologie de couches minces de perovskite par photoluminescence résolue spatialement avec une résolution micrométrique. Cette technique nous a permis d'observer des grains cristallins uniques. Nous démontrons que la transitions de la phase tétragonale à orthorhombique à basse température est incomplète dans tous les matériaux étudiés, comme montré par les résidus de phase tétragonale trouvés à T =4K. En étudiant structurellement régions endommagées et photo-recuites, nous montrons que la présence de la phase tétragonale à basse température est augmentée, causée par une déplétion de l'halogène.

Mots-clés: perovskites hybrides, photovoltaïque, énergie de liaison de l'exciton, masse effective, transition de phase.

Author: Krzysztof Gałkowski

Title: Magneto-optical and microscopic properties of organo lead halide perovskites

Supervisors: Paulina Płochocka-Maude, Piotr Kossacki

Specialty: Solid state physics

Abstract

The hybrid organo-lead halide perovskites are an emerging class of materials, proposed for use as light absorbers in a new generation of photovoltaic solar cells. The chemical formula for these materials is $APbX_3$, where A is an organic cation and X represents halide anions (most commonly Br^- , Cl^- or I^- , or alloyed combination of these). The hybrid perovskites combine excellent absorption properties with large diffusion lengths and long lifetime of the carriers, resulting in photon conversion efficiencies as high as 22%. Another advantage is the inexpensiveness of the fabrication process. Therefore, with the rapid development of this class of materials, the perovskite photovoltaics has perspectives to outperform the well-established silicon technology.

Here, we use optical methods to investigate the basic electronic properties and morphology in the thin films of several representatives of the hybrid perovskites. We study the compounds based on Methylammonium and Formamidinium organic cations; the iodides and wide band-gap bromides, showing how the chemical composition influences the investigated parameters.

Using magneto-transmission, we directly determine the values of exciton binding energy and reduced mass. We find that the exciton binding energies at $T = 2$ K, varying from 14 to 25 meV, are smaller or comparable to the average thermal energy at room temperature (≈ 25 meV). Moreover, these values fall further at $T = 160$ K, to 10–24 meV. Based on that we conclude that the carriers photocreated in a perovskite material can be considered to be thermally ionized at room temperature. The measured reduced masses are in the range of 0.09–0.13 of the electron rest mass. We also show that both exciton binding energy and reduced mass depend linearly on the band gap energy. Therefore, the values of these parameters can be easily estimated for the synthesis of new perovskite compounds.

Using spatially resolved photoluminescence, we probe the morphology of perovskite films with micrometer resolution, which enables us to observe single crystalline grains. The resulting maps show that all investigated thin films are composed from the dark and bright crystalline grains. We demonstrate that the low temperature phase transition from tetragonal to orthorhombic phase is incomplete in all studied materials, as the remains of the tetragonal phase are found even at $T = 4$ K. By investigating structurally damaged and photo annealed regions, where the occurrence of the tetragonal phase at low temperatures is enhanced, we attribute its presence to the depleted halide content.

Keywords: hybrid perovskites, photovoltaics, exciton binding energy, effective mass, phase transition

Autor: Krzysztof Gałkowski

Tytuł: Magnetoptyczne i mikroskopowe właściwości perowskitów – halogenków ołowiu i kationu organicznego

Promotorzy: Paulina Płochocka-Maude, Piotr Kossacki

Dyscyplina: Fizyka ciała stałego

Streszczenie

Hybrydowe perowskity – halogenki ołowiu i kationu organicznego - stanowią nową klasę materiałów, mogących znaleźć zastosowanie jako konwertery energii słonecznej w kolejnej generacji ogniw fotowoltaicznych. Struktura chemiczna tych materiałów opisywana jest wzorem $APbX_3$, gdzie A jest kationem organicznym a X anionem halogenkowym (najczęściej Br^- , Cl^- lub I^- , lub ich kombinacją). Hybrydowe perowskity charakteryzują się efektywną absorpcją światła w szerokim zakresie spektralnym, długimi drogami dyfuzji oraz długimi czasami życia nośników. Własności te przekładają się na wysoką wydajność konwersji fotonów, która w przypadku najlepszych ogniw perowskitowych sięga 22%. Niski koszt wytwarzania oraz szybki rozwój tej klasy materiałów stawia fotowoltaikę opartą na perowskitach wśród potencjalnych rozwiązań zastępujących obecnie wiodącą technologię krzemową.

Niniejsza praca poświęcona jest optycznym badaniom własności elektronowych oraz morfologii cienkich warstw hybrydowych perowskitów. Wykorzystano związki oparte na kationie metylamoniowym lub formamidynie, z jodem lub bromem jako anionami dominującymi. Uzyskane wyniki pozwalają określić wpływ składu chemicznego na badane parametry materiału.

Na podstawie pomiarów magnetotransmisji bezpośrednio wyznaczono wartość energii wiązania ekscytonu i masy zredukowanej. Energie wiązania ekscytonu w temperaturze $T = 2$ K wynoszą od 14 do 25 meV. Są to wartości mniejsze lub porównywalne do średniej energii termicznej w temperaturze pokojowej (25 meV). Co więcej, wartości te maleją wraz ze wzrostem temperatury, do 10-24 meV w $T = 160$ K. Tym samym wnioskujemy, że nośniki wzbudzone światłem w temperaturze pokojowej można uznać za termicznie zjonizowane. Zmierzone wartości masy zredukowanej mieszczą się w zakresie 0.09-0.13 masy spoczynkowej elektronu. Pokazaliśmy również, że zarówno energia wiązania ekscytonu, jak i jego masa zredukowana zależą w przybliżeniu liniowo od wartości przerwy energetycznej. Uzyskane zależności pozwalają w łatwy sposób oszacować wartości tych parametrów dla nowo zsynetyzowanych związków perowskitowych.

Metodą przestrzennie rozdzielonej fotoluminescencji zbadano morfologię warstw perowskitowych z mikrometrową rozdzielcością, co pozwoliło zaobserwować pojedyncze ziarna krystaliczne. Otrzymane mapy luminescencji powierzchni próbek pokazują, że wszystkie badane warstwy składają się z ciemnych i jasnych ziaren. Pokazujemy, że w niskotemperaturowa przemiana z fazy tetragonalnej w ortorombiczną jest niepełna, a pozostałość fazy tetragonalnej są obserwowane nawet w $T = 4$ K. Zauważając zwiększone występowanie tych inkluzji w okolicach obszarów uszkodzonych strukturalnie, korelujemy obecność niskotemperaturowej fazy tetragonalnej z lokalnymi zubożeniami zawartości halogenków.

Słowa kluczowe: hybrydowe perowskity, fotowoltaika, energia wiązania ekscytonu, masa efektywna, przemiana fazowa

Acknowledgements

My first words of gratitude are directed to my supervisors, Paulina Plochocka-Maude and Piotr Kossacki. I owe a lot to their support - both on the professional or personal level - continuing until the very last moment of my PhD course. I also acknowledge a significant support from Duncan K. Maude, reflecting in both scientific and editorial advice. And the numerous problems have become clearer after long discussions with Robin J. Nicholas (Clarendon Laboratory, University of Oxford).

I also would like to thank all my colleagues from both the National Laboratory of High Magnetic Fields (LNCMI-Toulouse, France) and Solid State Physics Division, University of Warsaw, Poland. They were always there - to give a piece of advice, to provide some urgent help, or to enjoy the out-of-the-lab moments. For the greatest contribution to this particular work, Anatoilie Mitioglou, Alessandro Surrente and Zhuo Yang should be named. It is also an opportunity to thank to the technical staffs of both laboratories - always helpful and responsive.

Last but not least, my loved ones were extremely understanding and supportive during those periods of my limited availability.

The financing for the co-tutelle program was approved by the French Embassy in Warsaw and supported my permanent scholarship provided by the University of Warsaw. I would also like to thank to the authorities of the LNCMI-Toulouse for an additional contract, which enabled an extension to my stay there.

Toulouse and Warsaw,

January 2017

Contents

1	Introduction	3
1.1	Interband absorption in the semiconductors: excitons	3
1.2	Perovskite structure	6
1.3	Hybrid perovskites	9
1.3.1	The role of halides: the inorganic cage	9
1.3.2	The role of organic cations: hydrogen bonds and octahedra tilting	10
1.3.3	Temperature dependence of the structural properties	11
1.3.4	Stability of organic-inorganic perovskites	13
1.4	Electronic properties of hybrid organic-inorganic perovskites	15
1.4.1	Band structure	15
1.4.2	Carrier diffusion lengths and mobilities	18
1.5	The evolution of hybrid perovskite materials	20
1.5.1	Towards the perovskite solar cells: the requirements for the photoactive material	20
1.5.2	The perovskite light absorbers beyond MAPbI_3	21
1.5.3	A key to the stability: mixed-cation mixed-halide hybrid perovskites	22
2	Experimental techniques	25
2.1	Spectroscopy in high magnetic field	25
2.1.1	Pulsed magnetic field generation	25
2.1.2	Transmission measurements	28
2.1.3	Temporal synchronization	31
2.2	Micro-Photoluminescence measurements	32
3	Preparation and characterization of the samples	35
3.1	Description of samples	35
3.2	Fabrication of the samples	36
3.3	Maintaining the perovskite phase	38
3.4	Sample characterization	40
4	Magneto transmission	45
4.1	Introduction	45
4.1.1	Electronic transitions in magnetic field	46
4.2	Low - temperature magneto-spectroscopy	51
4.2.1	Iodine-based compounds: $\text{MAPbCl}_x\text{I}_{3-x}$ and FAPbI_3	51
4.2.2	Tri-bromides: FAPbBr_3 and MAPbBr_3	53
4.2.3	Analysis	54
4.3	High temperature magneto-spectroscopy	60

4.4 Discussion	63
4.5 Conclusions	66
5 Spatially resolved micro - photoluminescence studies of organo-lead halide perovskites	67
5.1 Introduction	67
5.2 Temperature dependence studies	68
5.3 Spatially resolved μ -PL at room temperature	71
5.4 Spatially resolved μ -PL below the phase transition temperatures . .	72
5.4.1 MAPbI ₃ and FAPbI ₃	72
5.4.2 MAPbCl _x I _{3-x}	75
5.4.3 FAPbBr ₃	76
5.5 The coexistence of crystalline phases in the proximity of strain or defects	77
5.6 Conclusions	80
6 Caesium lead halide perovskites - characterization and magneto-optical studies	81
6.1 Fully inorganic caesium-based perovskite compounds	81
6.2 Characterization of the samples	83
6.3 Low-temperature magneto - transmission	84
6.4 Discussion	87
7 Conclusions	89
A Publications	91
B Résumé de la thèse en français	93
B.1 Introduction	93
B.2 Techniques expérimentales	93
B.3 La description et caractérisation des échantillons	94
B.4 Magnéto-transmission	96
B.5 Études de micro-photoluminescence résolues en temps de pérovskites d'halogénure d'organo-plomb	104
B.6 Les pérovskites halogénure d'plomb - et études magneto-optique . .	109
B.7 Conclusions	110
Bibliography	113

List of Figures

1.1	Energy states of an exciton	5
1.2	Ideal cubic structure in perovskites	7
1.3	Comparison of orthorhombic, tetragonal and cubic crystal structures	8
1.4	Influence of the halide composition on the band gap energy	10
1.5	Schematic representation of Methylammonium and Formamidinium cations	11
1.6	Temperature dependence of the crystal structure in MAPbI_3 , MAPbBr_3 and MAPbCl_3	12
1.7	Hydration in perovskites	14
1.8	Band structure of MAPbI_3	16
1.9	Comparison of absorption coefficients of MAPbI_3 , GaAs and c-Si	17
1.10	Lifetimes of the carries in MAPbI_3 and $\text{MAPbCl}_x\text{I}_{3-x}$ with and in the absence of electron/hole absorbing layers	19
2.1	High magnetic field installation of the LNCMI laboratory	26
2.2	Temporal profiles of typical magnetic field pulses	27
2.3	The elements of high magnetic field coils	28
2.4	Schematic representation of the setup used for transmission measurements in pulsed magnetic fields	29
2.5	Magneto-transmission probe	30
2.6	Temporal synchronization of the magnetic field pulse and the acquisition of optical signal	32
2.7	Schematic diagram of synchronization sequence	33
2.8	Schematic drawing of the μPL experimental setup	34
3.1	Photograph showing the typical Formamidinium - based samples with different halide content	36
3.2	Sequence of procedures in the one-step perovskite deposition method	37
3.3	Schematic representation of the two-step deposition method	37
3.4	Decomposed MAPbI_3 sample	38
3.5	Micro-PL spectra for pristine and degraded MAPbI_3	39
3.6	Typical transmission spectra for MAPbI_3 measured at different temperatures and absorption energies plotted as the function of temperature	41
3.7	Typical transmission spectra measured at different temperatures for $\text{MAPbCl}_x\text{I}_{3-x}$, FAPbI_3 , FAPbBr_3 and MAPbBr_3	42
3.8	The energies of near band edge absorption as a function of temperature for different perovskite materials	43
4.1	A schematic view of the Landau levels in the valence and conduction band.	48

4.2	Schematic view of energies of 1s, 2s and 2p hydrogen - like states calculated in magnetic field	50
4.3	The Zeeman band splitting	51
4.4	Typical magneto-absorption spectra for $\text{MAPbCl}_{x}\text{I}_{3-x}$ and FAPbI_3 at 2 K	52
4.5	Typical magneto-absorption spectra for FAPbBr_3 and MAPbBr_3 at 2 K	54
4.6	An example of typical magneto-transmission data with a fit of the excitonic and Landau transitions	55
4.7	Magneto-transmission results for the low temperature orthorhombic phase ($T \approx 2$ K)	57
4.8	Comparison of magneto-transmission results for FAPbBr_3 and MAPbBr_3	58
4.9	Zeeman splitting and Lande factors for $\text{MAPbCl}_{x}\text{I}_{3-x}$ and FAPbI_3	59
4.10	Typical magneto-absorption spectra for the tetragonal phase ($T \approx 160$ K)	60
4.11	Magneto-transmission results for the tetragonal phase ($T \approx 160$ K)	61
4.12	Reduced mass and binding energy in hybrid perovskites as the function of the band gap energy	63
5.1	Temperature dependence of absorption and micro-photoluminescence spectra in MAPbI_3	69
5.2	Temperature dependence of micro-photoluminescence spectra in $\text{MAPbCl}_{x}\text{I}_{3-x}$ and FAPbBr_3	70
5.3	Spatially resolved micro-photoluminescence for MAPbI_3 , $\text{MAPbCl}_{x}\text{I}_{3-x}$ and FAPbBr_3 at 300 K	72
5.4	Spatially resolved micro-photoluminescence for MAPbI_3 at 2 K	73
5.5	Spatially resolved micro-photoluminescence for FAPbI_3 at 2 K	74
5.6	Spatially resolved micro-photoluminescence for $\text{MAPbCl}_{x}\text{I}_{3-x}$ at 2 K	76
5.7	Spatially resolved micro-photoluminescence for FAPbBr_3 at 2 K	77
5.8	Tetragonal and orthorhombic phases in $\text{MAPbCl}_{x}\text{I}_{3-x}$ in the region exposed to the focused laser spot	78
5.9	Schematic drawn of photo-annealing induced distribution of iodine ions as a function of the distance from the point of exposure	79
5.10	Tetragonal and orthorhombic phases in FAPbI_3 in the vicinity of a structural defect	80
6.1	Two polymorphs of CsPbI_3	82
6.2	Temperature-dependent transmission for Cs-based compounds	84
6.3	Magneto-transmission spectra for Cs-based compounds	86
6.4	[Magnetotransmission results at low temperature ($T \approx 2$ K)]	87
6.5	Reduced mass and binding energy as the function of the band gap energy in hybrid and CsPbX_3 perovskites at $T = 2$ K	88
B.1	94

B.2	95
B.3	96
B.4	97
B.5	98
B.6	100
B.7	101
B.8	102
B.9	105
B.10	106
B.11	107
B.12	108
B.13	109

Preface

The hybrid organo-lead halide perovskites are an emerging class of materials, proposed for use as the light absorbers in a new generation of photovoltaic solar cells. The chemical formula for these materials is $APbX_3$, where A is a monovalent organic cation and X represents halide anions (most commonly Br^- , Cl^- or I^- , or alloyed combination of these). In contrast with state of the art photovoltaic materials, such as silicon or gallium arsenide, hybrid perovskites offer wide possibilities to manipulate the chemical composition, resulting in an advanced tunability of the optoelectronic properties. Another advantage is the inexpensiveness of the deposition process used to obtain thin perovskite films for solar cell applications. Furthermore, these compounds combine excellent absorption properties with large diffusion lengths and long lifetime of the carriers, while the high recombination rate of the photocreated carriers limits the photovoltaic photon conversion efficiencies in other low-temperature processed materials. For the hybrid perovskites, record efficiencies as high as 22% have been demonstrated in structurally stable compounds. Therefore, with the rapid development of this class of materials, the perovskite photovoltaics has perspectives to outperform the well-established silicon technology.

Despite the extensive research efforts since the first demonstration of a perovskite solar cell in 2009, many questions concerning the fundamental properties of hybrid perovskites remain unanswered. Among them is the value of exciton binding energy, determining the nature of the photocreated carriers. It is also important to precisely define the role of morphology, in particular the differences in optical quality between the adjacent crystalline grains within the perovskite thin films, on the performance of the photovoltaic devices.

In this thesis, we use optical methods to investigate the basic electronic properties and morphology in several representatives of the hybrid perovskites. We study the compounds based on Methylammonium and Formamidinium organic cations; the iodides and wide band-gap bromides. Using magneto-transmission, we determine the values of exciton binding energy and reduced mass with an improved accuracy surpassing previously reported results, obtained with indirect methods. Using spatially resolved photoluminescence, we investigate the morphology of perovskite films between 4 K and the room temperature with 1 μm resolution, which enables us to observe single crystalline grains. Our results determine the influence of chemical composition on the studied parameters, which is crucial for the synthesis and optimization of new perovskite hybrid compounds.

Chapter 1 introduces the topic of the thesis, starting from the properties of the excitons. Then, the general information about the perovskite crystalline structure are provided. Further sections are devoted to the hybrid perovskites; we discuss the influence of chemical composition on the structural and optoelectronic properties, the band structure, carrier diffusion lengths and lifetimes, and structural stability of these compounds. Finally, we present the advantages and disadvantages of the

most popular hybrid perovskite compounds synthesized until now, showing also a most probable evolution of this research field.

Chapter 2 presents the experimental techniques and equipment used for the measurements in this thesis. In Chapter 3, we describe the investigated thin-film samples and the methods of their fabrication. We also characterize the samples, performing temperature-dependent transmission. We demonstrate that the progress of the phase transition from the low-temperature orthorhombic phase to the tetragonal phase with increasing temperature depends on the chemical composition.

Chapter 4 is devoted to high-field magneto-spectroscopy. First, we discuss the influence of magnetic field on the optical transitions. Then, we present our magneto-transmission studies in the low temperature, orthorhombic phase and higher temperature tetragonal phase. We extract the exciton binding energies and reduced masses, showing that these parameters depend linearly on the band gap energy, without the influence of the type of the organic cation. We find that the exciton binding energies at low temperatures are smaller or comparable to the average thermal energy at room temperature, and that these values fall further at higher temperatures. Based on that we conclude that the carriers photocreated in a perovskite solar cell can be considered to be thermally ionized at room temperature.

In Chapter 5, we present our results on spatially-resolved photoluminescence. We demonstrate that all investigated perovskite thin films are composed from the dark and bright crystalline grains. We show that the low temperature transition from the tetragonal to orthorhombic phase is incomplete, as the remains of the tetragonal phase are found even at $T = 4$ K. The size of the tetragonal phase inclusion is comparable to the dimensions of single crystalline grains, while macroscopic phase domains, containing hundreds of single grains, have been observed only in the high band-gap tri-bromide compound. Furthermore, we find that the occurrence of the tetragonal phase inclusions is enhanced in structurally damaged and photo annealed regions.

Chapter 6 contains our preliminary results from studies of fully inorganic, caesium-based CsPbX_3 compounds. By comparing the exciton binding energies and reduced masses in the inorganic and hybrid compounds, we aim at understanding the role of the organic cation in determining the properties of organo-lead halide perovskites.

CHAPTER 1

Introduction

Contents

1.1	Interband absorption in the semiconductors: excitons	3
1.2	Perovskite structure	6
1.3	Hybrid perovskites	9
1.3.1	The role of halides: the inorganic cage	9
1.3.2	The role of organic cations: hydrogen bonds and octahedra tilting	10
1.3.3	Temperature dependence of the structural properties	11
1.3.4	Stability of organic-inorganic perovskites	13
1.4	Electronic properties of hybrid organic-inorganic perovskites	15
1.4.1	Band structure	15
1.4.2	Carrier diffusion lengths and mobilities	18
1.5	The evolution of hybrid perovskite materials	20
1.5.1	Towards the perovskite solar cells: the requirements for the photoactive material	20
1.5.2	The perovskite light absorbers beyond MAPbI_3	21
1.5.3	A key to the stability: mixed-cation mixed-halide hybrid perovskites	22

1.1 Interband absorption in the semiconductors: excitons

In the semiconductor material, the interband absorption of a photon promotes an electron from the valence band to the conduction band. The resulting electron - hole pair, interacting via the attractive Coulomb force, is known as the neutral exciton. Excitons have been predicted theoretically in 1930s [Frenkel 1931, Peierls 1932, Wannier 1937] and observed for the first time in the absorption spectra of Cu_2O [Hayashi 1950]. The properties of excitons in semiconductor materials have been summarized, among other works, in the book of Yu and Cardona [Yu 2010], used here as the reference.

Due to an analogy of the electron - hole pair to the electron - proton pair, the excitons can be described within a hydrogen atom - like model. However, in a

crystal, the presence of mobile charges screens the Coulomb interaction between the electron-hole pair, thus, the relative dielectric constant ε_r is larger than 1. Therefore, when compared to the hydrogen atom, the binding energy of the exciton is lowered, leading to an increase of the Bohr radius. Depending on the ratio of the Bohr radius to the size of the unit cell in the crystal, the Frenkel or Wannier-Mott excitons are considered. The excitons in semiconductors are usually large-radius Wannier-Mott excitons [Liang 1970, Yu 2010], in contrast to tightly bound Frenkel excitons, observed e.g. in the organic semiconductors and ionic crystals [Muto 1958, Lidzey 2000].

Below, we discuss the properties of Wannier-Mott excitons within the effective mass approximation, assuming parabolic, non-degenerate bands of isotropic dispersion. In this approach, the motion of the electron and hole can be described using separable coordinates of the excitonic center of the mass \vec{R} and the relative coordinates of electron and hole \vec{r} :

$$\vec{R} = \frac{m_e^* \vec{r}_e + m_h^* \vec{r}_h}{m_e^* + m_h^*} \quad \vec{r} = \vec{r}_e - \vec{r}_h, \quad (1.1)$$

where \vec{r}_e , \vec{r}_h and m_e^* , m_h^* are vectors of the positions and effective masses of electron and hole, respectively. The \vec{R} coordinate describes the motion of a particle of a mass $M = m_e^* + m_h^*$. The Coulomb interaction between the electron and hole depends only on the relative coordinate \vec{r} . The envelope of the excitonic wavefunction is given by [Yu 2010]:

$$\Psi(\vec{r}_e, \vec{r}_h) = N^{-1/2} \exp(i\vec{K}\vec{R}) \phi(\|\vec{r}\|), \quad (1.2)$$

where $\vec{K} = \vec{k}_e + \vec{k}_h$ is the exciton wavevector and N is the unit cell volume. The ground state of an exciton is described with a wavefunction analogous to the wavefunction of the 1s state of hydrogen atom:

$$\phi(\|\vec{r}\|) = \frac{1}{\sqrt{\pi a_B^{*3}}} \exp\left(-\frac{\|\vec{r}\|}{a_B^*}\right) \quad (1.3)$$

where $a_B^* = \frac{\hbar^2 \varepsilon}{\mu e^2}$ is the excitonic Bohr radius. Here, e and $\varepsilon = \varepsilon_0 \varepsilon_r$ are the fundamental electric charge and the effective dielectric constant of the semiconductor, respectively, while μ is the reduced excitonic mass, related to the effective masses of the electron and hole as:

$$\frac{1}{\mu} = \frac{1}{m_e^*} + \frac{1}{m_h^*} \quad (1.4)$$

In a material with the band gap energy E_g , the energy of the n th excitonic level has a following form:

$$E_n(\vec{K}) = E_g + \frac{\hbar^2 \vec{K}^2}{2M} - \frac{R^*}{n^2}. \quad (1.5)$$

The second term in the Equation 1.5 corresponds to the kinetic energy of the excitonic center of the mass, while the last term is the exciton binding energy, equal

to the effective Rydberg constant R^* for the $n = 1$ ground state. A typical plot of $E_n(\vec{K})$ dependence from Equation 1.5 is presented in Fig. 1.1 (a), for the values of n from 1 to 3. For excitons in semiconductors, the continuum of states with energy closest to the band gap can be considered as effectively ionized [Yu 2010]. According to Equation 1.5 and Fig. 1.1 (a), the excitonic lines in the optical spectra are observed below the band edge. This is schematically presented in Fig. 1.1 (b), which compares the absorption spectra with and without excitonic effects.

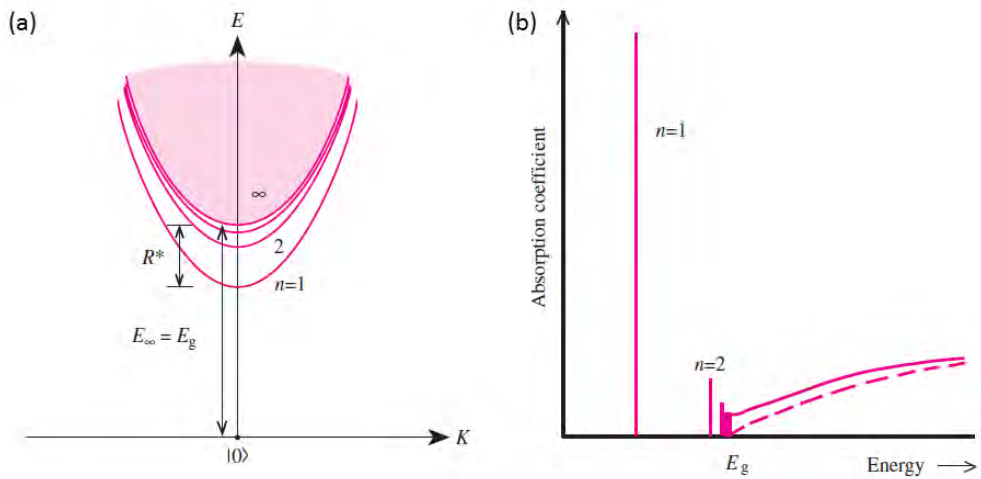


Figure 1.1: (a) The energy states of an exciton showing both its lowest states of $n = 1$ to 3 and the continuum states. E_g is the bandgap and R^* the exciton binding energy. (b) Comparison between the absorption spectra in the vicinity of the bandgap of a direct-gap semiconductor with (solid lines) and without (broken curve) excitonic effects. After Reference [Yu 2010].

Apart from the dielectric screening, the exciton binding energy is also modified by the ratio of the excitonic reduced mass μ and the rest mass of the electron m_0 . Therefore, the effective Rydberg constant R^* is related to the atomic Rydberg constant $Ry = -13.6$ eV as:

$$R^* = Ry \cdot \frac{\mu}{m_0 \varepsilon_r^2}. \quad (1.6)$$

The exciton binding energies in semiconductor materials usually vary from a few to tens of meV, e.g. 4.9 meV in GaAs and 59 meV in ZnO [Yu 2010]. In the organic-inorganic perovskites, the values of exciton binding energies remains controversial, as the reported results are in the range of 2 – 80 meV [DInnocenzo 2014, Lin 015, Miyata 2015].

The ratio of the exciton binding energy to the mean thermal energy, $E_T = k_B T$, determines the nature of the photocreated carriers. If R^* is smaller than E_T , which is around 25 meV at the room temperature, the fraction of the electrons and holes bound as the excitons is small when compared to the population of free carriers.

This has a particular significance for the photovoltaic devices, where the efficient extraction of the photoexcited carriers substantially contributes to the photon conversion efficiency. In contrast, if $R^* > E_T$, the electron-hole pair remains bound by the Coulomb interaction.

Apart from the neutral excitons, more complex excitonic systems can be formed in the semiconductors. The electrically neutral potential traps, such as the intrinsic or intentionally introduced impurity atoms or defects, capture the free excitons. Due to such localization, a free exciton becomes a bound exciton [Pelant 2012, Yu 2010]. If the binding impurities are not electrically neutral, the Coulomb interactions with the electron-hole pair further increases the binding energy. Therefore, as in e.g. the luminescence spectra of GaAs, the bound excitons are detected at energies lower than the free exciton, and the emission energy of the excitons bound on the charged impurities is lower than those formed on electrically neutral traps.

Due to the large Bohr radius of the Wannier-Mott excitons, the cross section for the localization on the impurities is high. Therefore, the photoluminescence spectra can be dominated by the bound exciton emission even for materials with a low impurity level.

In a semiconductor which is doped *n*- or *p*-type (with excess of free carriers), the charged excitons (also known as trions) can be created. When compared to the neutral exciton, the trions have an additional electron or hole, thus their net charge is $-e$ (negative trion) or $+e$ (positive trion). The existence of charged excitons has been predicted by Lampert [Lampert 1958] with a suggested first demonstration in bulk silicon and germanium [Kawabata 1977, Thomas 1977]. However, as the binding energy for the additional charged particle is relatively low, the confinement resulting from a reduced dimensionality of the semiconductor structure is crucial for the observation of the trions. The first observation of spectrally well-resolved absorption lines corresponding to the trions has been reported in modulation doped CdTe quantum wells by Kheng et al. [Kheng 1993]. Apart from the quantum wells, the trions have been observed in low-dimensional structures as quantum dots [Kossacki 2000, Jha 2009, Gong 2015], and two dimensional transition metal dichalcogenides [Mak 2012, Mitioglu 2013]. Another excitonic complex characteristic for the low-dimensional structures is a biexciton, a state composed of two neutral excitons, observed at high excitation power densities [Kalt 2013].

1.2 Perovskite structure

The perovskites are a class of compounds which have the same crystal structure as calcium titanate (CaTiO_3), the mineral originally named perovskite. The general chemical formula of perovskites is ABX_3 , as the unit cell consists of two cations (a large cation A and smaller cation B) and three anions, denoted by X. A remarkable perovskite material is lead zirconate titanate $\text{Pb}[\text{Zr}_x\text{Ti}_{1-x}]\text{O}_3$, known also as PZT, a ferroelectric compound which has dominated the industry of piezoelectric devices [Uchino 2015]. The perovskites are also investigated, among other applications,

as superconductors [He 2001, Gordon 2016] or topological insulators [Haldane 1988, Jin 2012].

The perovskite structure in its simplest, cubic form, is schematically presented in Fig. 1.2. Such structure can be described as cubic close packed lattice of A and X ions, with B ions in a 6-fold coordination, as they are located at the octahedral vacancies of the X ions [Johnsson 2007]. Therefore, the B and X ions form a grid of corner-sharing BX_6 octahedra, with the A cations incorporated inbetween the grid. The A cation is then surrounded by cuboctahedron of anions (12-fold coordination).

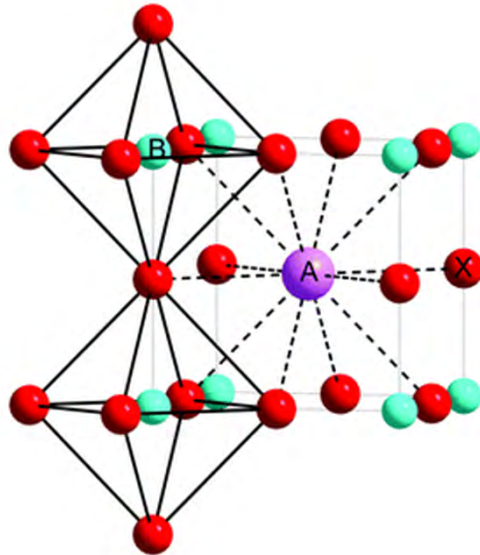


Figure 1.2: The ideal cubic perovskite structure: corner-sharing BX_6 octahedra (B = blue spheres, X = red spheres) and the A cation (violet sphere) in the center of the unit cell in 12-fold cuboctahedral coordination. After Reference [Johnsson 2007].

In the ideal perovskite cubic structure, the length of the unit cell a is equal to:

$$a = \sqrt{2}(r_A + r_X) = 2(r_B + r_X), \quad (1.7)$$

where $r_{A,B,X}$ are the ionic radii of A, B and X ions, respectively. However, this identity relation is not fulfilled for the majority of perovskite compounds. This causes a tilt or rotation of the BX_6 octahedra in order to fill in the space. As a result, the symmetry of the crystal structure is lowered. Two examples of such distorted lattices, orthorhombic and tetragonal, are schematically shown in Fig. 1.3 (a) and (b), respectively. The undistorted cubic structure for comparison is shown in panel (c). In order to determine the degree of distortion, a parameter named Goldschmidt's tolerance factor t [Johnsson 2007, Amat 2014, Kieslich 2015] is commonly used:

$$t = \frac{\sqrt{2}(r_A + r_X)}{2(r_B + r_X)}. \quad (1.8)$$

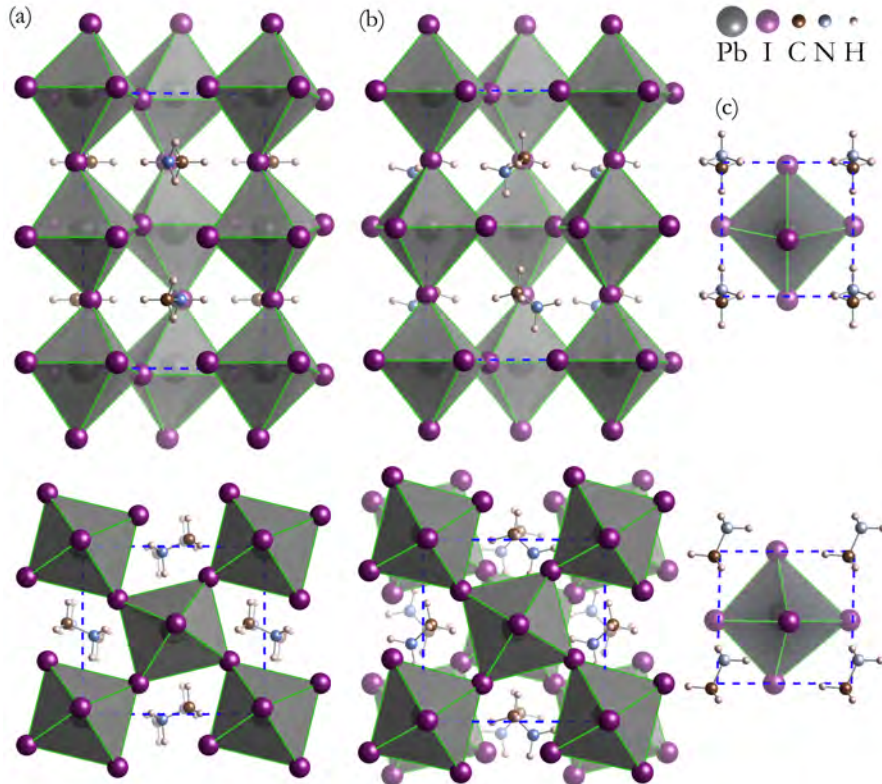


Figure 1.3: The crystal structures of the (a) orthorhombic, (b) tetragonal and (c) cubic phases of MAPbI₃. The upper and lower panels are oriented through $<100>$ and $<001>$, respectively. The PbI₆ octahedra are shaded grey. After Reference [Brivio 2015].

It is a ratio of the lengths of the unit cell from Equation 1.7. The SrTiO₃ is an ideal cubic perovskite with $t = 1$ [Johnsson 2007]. The cubic structure is expected to be stable in the range of $0.89 < t \leq 1$. For lower values of t , the perovskites form the tetragonal $0.81 < t < 0.87$ and orthorhombic $t < 0.81$ structures. The hexagonal phase occurs for $t > 1$ (e.g. BANiO₃) [Johnsson 2007]. It should be noticed, that Goldschmidt's tolerance factor is only a rough approximation for the distortion effects. As this parameter considers exclusively the ionic bonds, it becomes highly inaccurate in the case when the molecules are incorporated into the perovskite lattice [Johnsson 2007, Amat 2014, Kieslich 2015].

Moreover, the relative cation size is only one of the factors influencing the lattice symmetry. Among the others are e.g. the distortions due to deviation from the ideal ABX₃ formula. This is most common in the perovskite oxides, where due to oxygen vacancies, less symmetric structures are formed instead of the BX₆ octahedra [Vidyasagar 1985, Yang 2003]. Also, in perovskites with transition metal ions incorporated in the B position, the Jahn-Teller effect can be observed if the d

orbitals are unevenly occupied. This results in the elongation of the BX_6 octahedra, leading to their rotation, as observed in LaMnO_3 [Johnsson 2007, Aguado 2012].

It is also important to note that the perovskite structure depends on the temperature. Due to the differences in the temperature evolution of particular lattice constants, the level of distortion changes, inducing transitions between different crystal structures. As an example, BaTiO_3 exhibits three phase transitions (consecutively the rhombohedral, orthorhombic, tetragonal and cubic phases) between -90 °C and 120 °C [Johnsson 2007]. The temperature dependence of the crystals structure of organic-inorganic perovskites is further discussed in Section 1.3.3.

1.3 Hybrid perovskites

In the hybrid perovskites, the large cation (A in the ABX_3 general formula) is an organic molecule. The most common organic compounds are Methylammonium (MA: CH_3NH_3^+) or Formamidinium (FA: $\text{CH}(\text{NH}_2)_2^+$). Usually, the lead ions Pb^{2+} are incorporated in the small-cation B positions (lead-free materials, containing tin, $\text{B}=\text{Sn}^{2+}$, have also been investigated [Noel 2014, Anaraki 2016]). The X positions are occupied by the anions of group VII halides (Br^- , Cl^- , I^-), either in homogeneous or mixed compositions. The most recognized representative of this family is MAPbI_3 , used for the first demonstration of a perovskite solar cell [Kojima 2009]. This widely investigated compound is now being surpassed by newly synthesized materials, as the large number of available combinations in the ionic content allows an advanced tailoring of the perovskites' properties [Amat 2014, Hoke 2015], which will be briefly discussed below.

1.3.1 The role of halides: the inorganic cage

In hybrid perovskites, the conduction and valence band originate from the orbitals of the inorganic lattice [Umebayashi 2003]. Therefore, the chemical composition of the octahedral anionic cage has a significant impact on the electronic properties of perovskites, in particular, the band gap energy. Substitution- partial or total - of the halide anions in the perovskite lattice with lighter halides (thus, the elements of higher electronegativity), results in an increase of the band gap [Kulkarni 2014, Hoke 2015, yi Huang 2016]. Such an evolution of the band gap energy is demonstrated in Fig. 1.4, which contains a photograph of the Methylammonium - based photovoltaic devices of different halide content. This figure shows a sequential change from pure tri-iodide to pure tri-bromide from left to right, with corresponding absorption coefficients as the function of wavelength/energy. The MAPbI_3 has a band gap $E_g \simeq 1.6$ eV, which blue-shifts to the visible range as the iodine ions are gradually substituted with bromine ($E_g \simeq 2.2$ eV for MAPbBr_3). Introducing the lightest chlorine ions, it is possible to increase the band gap even to the UV range ($E_g \simeq 3.1$ eV for MAPbCl_3 [Suarez 2014]).

The influence of the halide composition on the lattice parameters reflects in the size-induced alignment of the BX_6 octahedra, leading to changes in the crystal

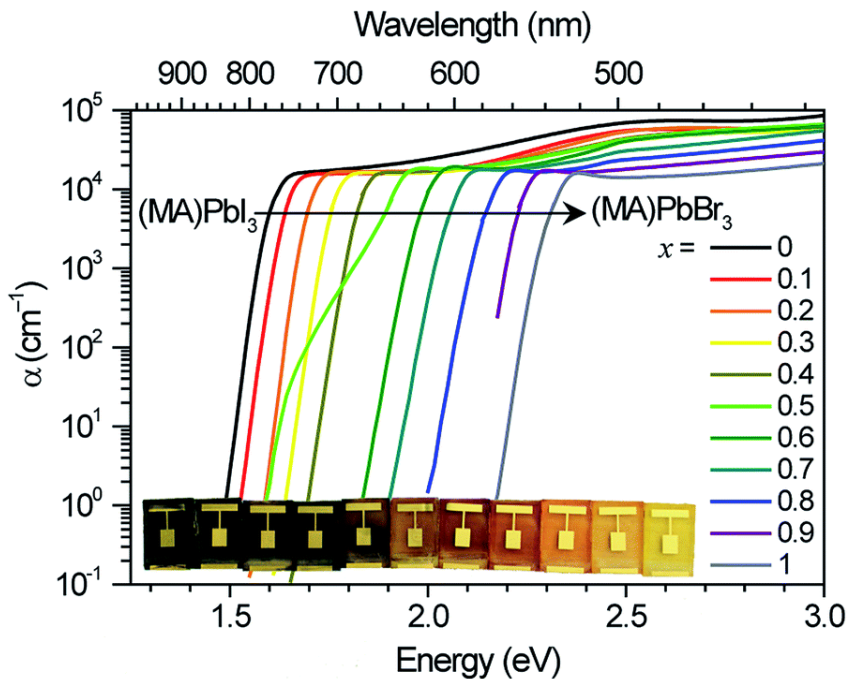


Figure 1.4: Absorption coefficient of $\text{MAPb}(\text{Br}_x\text{I}_{1-x})_3$. Inset: photograph of $\text{MAPb}(\text{Br}_x\text{I}_{1-x})_3$ photovoltaic devices from $x = 0$ to $x = 1$ (left to right). Reprinted from Reference [Hoke 2015].

structure. The bromide compounds are cubic at the room temperature, while the iodides, which have larger octahedra, form the tetragonal [Noh 2013, Eperon 2014a] or trigonal [Amat 2014] phase. In the family of Formamidinium based compounds, $\text{FAPbBr}_{3-x}\text{I}_x$, the transition to the tetragonal phase occurs at an iodine content of around $x = 0.6$ [Eperon 2014a].

1.3.2 The role of organic cations: hydrogen bonds and octahedra tilting

Although the organic cations do not contribute directly to electron related-phenomena, the orientation and symmetry of the organic molecules play a significant role in determining the disorder of the perovskite structure. The effects of substitution of Methylammonium with Formamidinium cations have been discussed by Amat et al. [Amat 2014]. The schematic representations of Methylammonium and Formamidinium molecules are shown in Fig. 1.5. The ionic radius of Formamidinium (2.79 Å) is only slightly larger than for Methylammonium (2.70 Å). Therefore, differences in the band gap energy - in the MAPbI_3 around 0.12 eV higher than in its FAPbI_3 analogue - cannot be fully justified by the different relative size. An analysis of the lowered symmetry of the Formamidinium molecule and the distribution of the hydrogen atoms within it suggests an enhanced ability of formation of the hydrogen

bonds with the inorganic lattice, when compared to Methylammonium. Amat et al. [Amat 2014] postulate, that the increased number of hydrogen bonds results in a tilt of the inorganic octahedra, and therefore the FAPbI_3 crystallizes in the trigonal pseudocubic structure, as previously suggested by Pang et al. [Pang 2014]. The theoretical calculations of Amat et al. [Amat 2014] indicate that the trigonal structure amplifies the Pb-like character of the conduction band. This results in an increased spin-orbit coupling, which lowers the band gap energy.

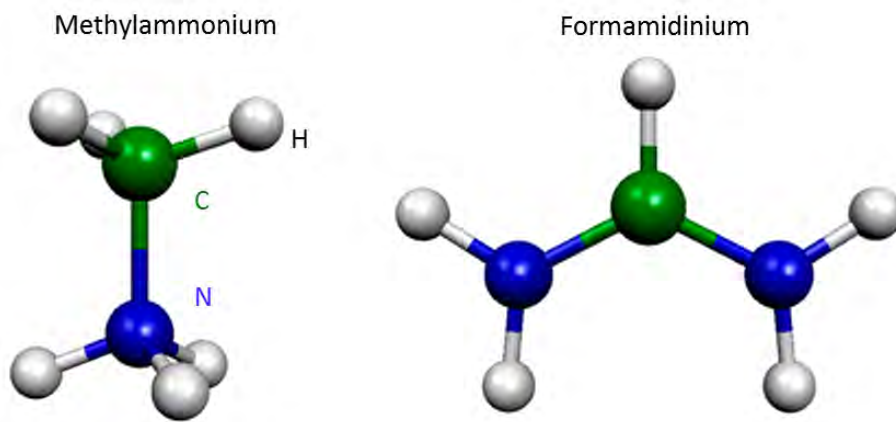


Figure 1.5: Structure of Methylammonium and Formamidinium cations. Reprinted from Reference [Amat 2014]

It has been also suggested that the high-frequency fluctuations in the orientation of the organic cations are followed by temporal changes in the local distortion of the crystal structure (referred to as the "dynamic disorder"), which has an influence on the electronic properties [Motta 2015, Etienne 2016]. In particular, the rotations of dipolar organic molecules induce a time - variable Rashba splitting of the bands. Theoretical calculations, the positions of the extrema of valence and conduction band oscillate independently in k -space on a timescale of subpicoseconds [Etienne 2016]. Therefore, this phenomenon was proposed as possible explanation for the long lifetimes observed in hybrid perovskites, originating from the reduced carrier recombination rate due to a periodic switching between the direct and indirect band gap, and a favoring of the exciton separation [Motta 2015, Etienne 2016].

1.3.3 Temperature dependence of the structural properties

The entire class of organic - inorganic perovskite materials reveals similar temperature dependence of the lattice structure, which can be either orthorhombic at low temperatures, or consecutively tetragonal/trigonal and cubic, when the temperature is raised. Therefore, a series of phase transitions, associated with the reorientation

of the BX_6 octahedra, can be observed in these compounds [Oku 2015, Frost 2016]. The temperature ranges corresponding to the particular phase transitions, on the example of the family of Methylammonium-based compounds - MAPbI_3 , MAPbBr_3 and MAPbCl_3 , are presented in Fig. 1.6.

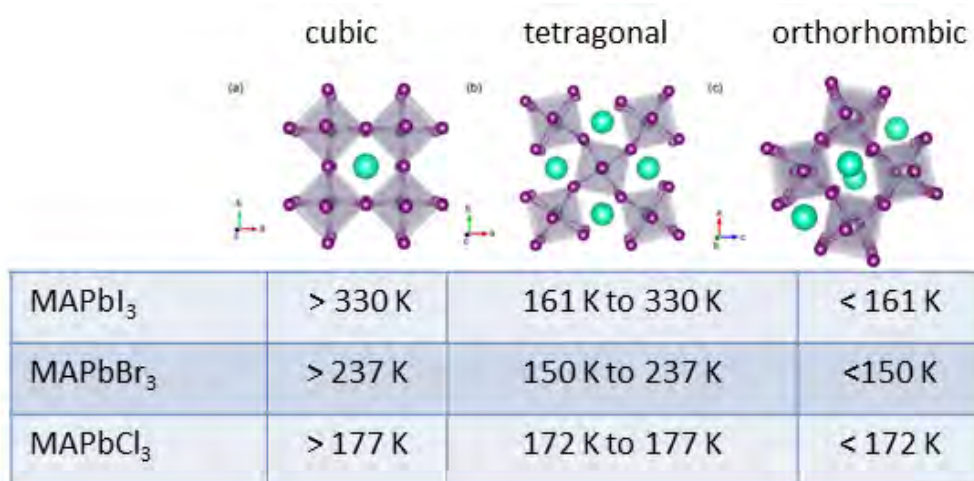


Figure 1.6: Temperature dependence of the crystal structure in MAPbI_3 , MAPbBr_3 and MAPbCl_3 . Data after the Reference [Oku 2015], figure reprinted from [da Silva 2015]

At the low temperature orthorhombic phase, the sublattice of the organic cations is ordered, with their motion being limited to vibrations without a reorientation of the C-N bonds [Ong 2015, Frost 2016]. The increasing temperature induces a relatively large expansion of the out-of-plane c lattice constant, eventually enabling the rotation of the entire organic molecule. At this point, the orientation of the organic cations can be distributed between eight disordered states, which is followed by a reorientation of the inorganic octahedra. This changes are associated with the transformation to the tetragonal phase [Weller 2015, Ong 2015]. This first order phase transition, reported to occur in the range between 140 K and 170 K for different compounds (see Fig. 1.6), has a significant influence on the optoelectronic properties of hybrid perovskites. One of the consequences of the transformation from the orthorhombic to tetragonal structure is a decrease in the band gap energy, which is in the range of 10 - 90 meV depending of the compound [Wang 2015a, Kong 2015]. The libration of the organic molecules, quenched at lower temperatures, becomes allowed in the tetragonal phase [Ong 2015]. As a result, the contribution of the organic sublattice to the electric field screening increases. The resulting increase in the low-frequency dielectric constant leads to a drop in the exciton binding energy [Even 2014b].

Remarkably, microscopic studies have revealed that in the polycrystalline films

the phase transition between the orthorhombic and tetragonal structure does not happen uniformly over the film. The remains of the tetragonal phase can be found even at temperatures as low as 4 K, which is also discussed in this work. The temperatures at which the entire film is converted to the tetragonal phase, usually attributed to the phase transition point, are similar between the different reports. Only in the perovskite materials composed of small (< 500 nm) crystalline grains, the temperature of this structural transformation was shown to be grain size dependent [Li 2016]. Depending on the compound, the phase transition was reported to develop over the temperature range of a few to tens of Kelvin [Wang 2015a, Kong 2015]. This process has been thoughtfully studied in the archetypal MAPbI_3 [Osherov 2016]. It has been shown that in this material, the ratio of the orthorhombic and tetragonal phase domains within the film at given temperature depends on the direction and rate of the temperature change. The existence of such hysteresis has been confirmed by the optical and crystallographic studies [Osherov 2016].

The parameters of the tetragonal lattice become more isotropic with further increase of the temperature above the phase transition point, resulting in the second order transition to the cubic phase. This structural change can be observed with the temperature-dependent studies of neutron [Weller 2015] or X-ray diffraction [Swainson 2003, Wang 2015b] and specific heat capacity [Onoda-Yamamuro 1990]. As shown in Fig. 1.6, the temperature of transition from the tetragonal to cubic phase is influenced by the size of the halide atoms. The elongation of the relatively large inorganic cage along the c axis suppresses the formation of the cubic phase in MAPbI_3 until 327 K, while the compounds containing smaller bromine and chlorine atoms undergo this process at around 240 K and 178 K, respectively.

1.3.4 Stability of organic-inorganic perovskites

The long term stability of organic-inorganic perovskite compounds is the biggest challenge for the perovskite-based photovoltaics. Below, we discuss the most important factors which influence the lifetime of the perovskite-based solar devices.

The photoactive and photo - inactive phases. Some of the hybrid perovskites can simultaneously form different polymorphic phases. This is, for example, the case of FAPbI_3 , which crystallizes either in the photoactive, "black" perovskite α -phase, or the photo inactive, "yellow" non-perovskite δ -phase [Stoumpos 2013, Eperon 2014b]. The black phase is stable above 60° C; below this temperature, it gradually converts into the photo-inactive polymorph. This process is catalyzed by the presence of humidity [Jeon 2015]. Although the transition to the δ -phase is reversible by annealing [Stoumpos 2013, Jeon 2015], without a permanent stabilization of the α -phase the optoelectronic properties of FAPbI_3 will constantly worsen with the increasing number of the non-perovskite inclusions.

Air and humidity. The hybrid perovskites easily react with water and other polar solvents [Kojima 2009]. The hydration of MAPbI_3 was found to be reversible under the dry air, however the long exposure to humidity enhances the irreversible sepa-

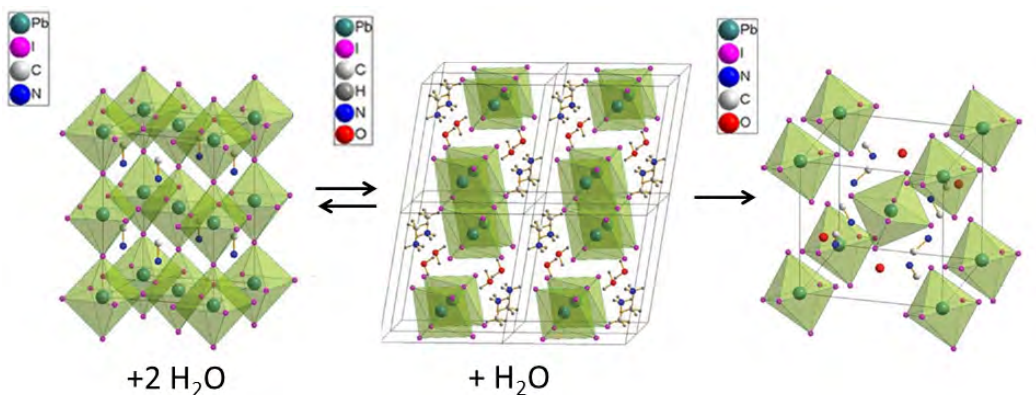


Figure 1.7: (a) The structure of MAPI in its cubic phase, (b) the monohydrate phase, $\text{CH}_3\text{NH}_3\text{PbI}_3 \cdot \text{H}_2\text{O}$ and (c) displays the structure of the dihydrate, $(\text{CH}_3\text{NH}_3)_4\text{PbI}_6 \cdot 2\text{H}_2\text{O}$. After Reference [Leguy 2015]

ration of the hydrogen iodide HI and lead di-iodide PbI_2 [Leguy 2015, Yang 2015]. When accompanied by the heat, this process can degrade the MAPbI_3 film within 24h [Habisreutinger 2014, Liu 2015]. Leguy et al. have revealed a two - stage character of the hydration process, which is presented in Fig. 1.7 [Leguy 2015]. When exposed to the moisture, primarily a monohydrate phase of the perovskite is formed. Depending on the exposure time and the level of the moisture, it can further develop to the dihydrate phase, associated with the irreversible decay of the organic molecule and segregation of PbI_2 crystals. In agreement with this picture, the degradation of MAPbI_3 based solar cells occurs several times slower in the conditions of normal humidity (< 50%) than when the humidity exceeds 80% [Leijtens 2015]. To protect the perovskite films from the atmospheric moisture, several methods of encapsulation with isolating or hydrophobic materials have been proposed, resulting in the improved stability of the perovskite solar cell. Among them are the methods of glass encapsulation, adapted from the organic photovoltaics [Habisreutinger 2014, Matteocci 2014], or the coating of the perovskite film with a hydrophobic, polymer hole absorber with incorporated single-wall carbon nanotubes [Habisreutinger 2014]. The encapsulation eliminates another ageing catalyst connected with the ambient air environment, which is photooxidation [Leijtens 2015]. With the exclusion of the tin-containing compounds [Noel 2014], the hybrid perovskites are resistant to oxidation in the dark [Kim 2012].

Heat and intense light. Although the influence of the atmosphere can be reduced with the protective or functional layers, the presence of an intense illumination and the resulting raised temperature is unavoidable under the operational conditions of solar cells. Even when isolated from the air, the thermal degradation of MAPbI_3 , observed by mass loss, occurs already at 85 °C [Conings 2015]. Moreover, the lead-halide perovskites are good conductors for the ions and ionic defects [Mizusaki 1983,

[Leijtens 2015]. The ion migration freezes out at lower temperatures [Xiao 2014, Yuan 2015], while at room temperature and under applied bias voltage, a development of a non-stoichiometric distribution of the ions was reported [Zhao 2015, Zhang 2015]. Also, the illumination - induced reversible segregation of the halide ions into bromine and iodine rich domains was observed in $\text{MAPbBr}_x\text{I}_{3-x}$, resulting in the local fluctuations of the band gap energy [Hoke 2015].

The numerous attempts to limit the problems stated above have been made, based mainly on the manipulation of the chemical composition of perovskite materials. The stability of these novel compounds is further discussed in Section 1.5, with Section 1.5.3 being devoted to the most robust, mixed-cation materials.

1.4 Electronic properties of hybrid organic-inorganic perovskites

A deep understanding of the fundamental phenomena responsible for the high photon conversion efficiencies in hybrid perovskite solar cells is required for the further, controlled development of these materials. In this section, we summarize the literature concerning the perovskite band structure and the carrier diffusion lengths, explaining the origins of the strong broadband absorption and the efficient extraction of photocreated carriers.

1.4.1 Band structure

The band structure of the hybrid perovskites is commonly derived from the density functional theory (DFT) simulations [Even 2012, Even 2014b, Umari 2014, Zhou 2014]. The selected calculations for the cubic MAPbI_3 , performed by Even et al. [Even 2014b], are summarized below. These results can be extended to the room temperature tetragonal phase due to the relevance in the symmetry analysis for the structures with a group-subgroup relationship [Even 2014a].

A schematic view of the reciprocal space of the cubic lattice with the first Brillouin zone is drawn in Fig. 1.8 (a). Point Γ corresponds to the center of the Brillouin zone, while points M and R are the centers of cube edges and vertices of the cube, respectively. Fig 1.8 (b) presents a plot of the Fermi surface in the Brillouin zone. This isoenergy surface (at $E = -0.5$ eV) connects the valleys of the Brillouin zone, centered at the R points, with the saddle - like M points. Therefore, the holes photo-created at the edges of Brillouin zone can migrate towards R.

The band structure calculated for the cubic phase MAPbI_3 at the different points of the Brillouin zone is shown in Fig. 1.8 (c). The conduction and valence bands are relatively symmetric, leading to similar values of the effective masses for electrons and holes. Two direct band gaps are found at the R (primary band gap) and M (secondary band gap) points of the Brillouin zone. The character of the conduction band is dominated by lead p orbitals, while the valence band consists of iodine p - with some component of lead s orbitals [Umebayashi 2003, Even 2012, Umari 2014].

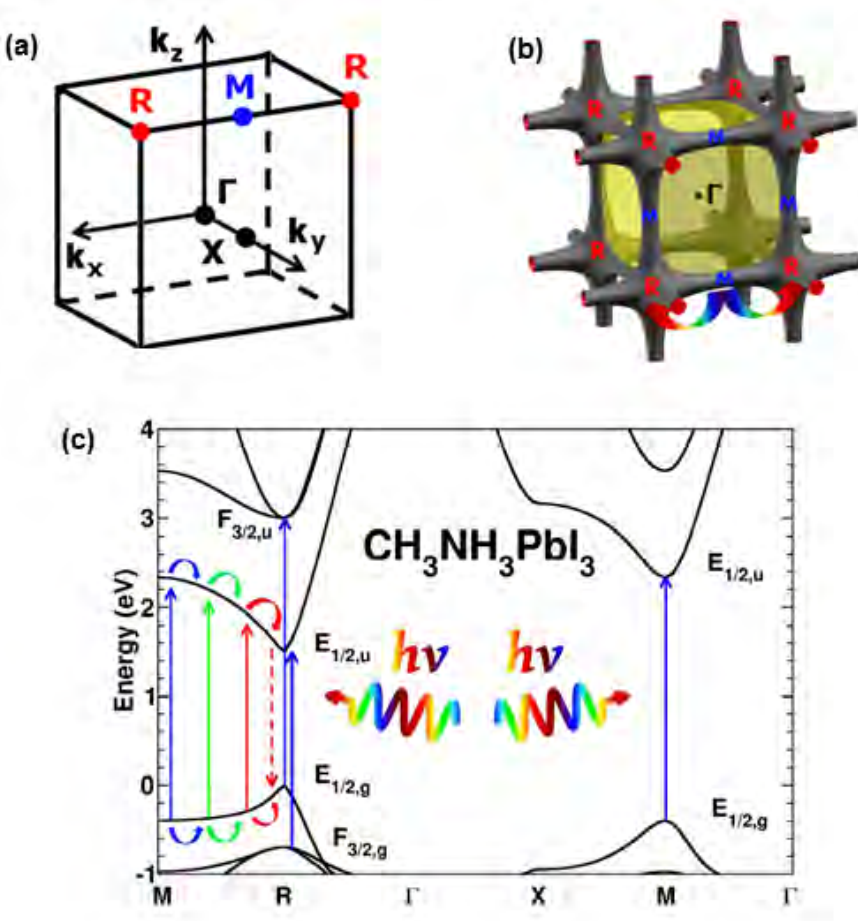


Figure 1.8: (a) Reciprocal space 3D view showing the first Brillouin zone. (b) Fermi surface ($E = -0.5$ eV) in the first Brillouin zone Z. R and M are connected along the zone edges, highlighting the saddle nature of the point M. (c) Electronic band diagram of the high temperature cubic phase of MAPBI_3 taking the spin-orbit coupling into account. An upward energy shift of 1.4 eV has been applied to match the experimental bandgap value at R. The relaxation of the carriers excited along the $M \rightarrow R$ path is sketched. After Reference [Even 2014b].

The contribution of heavy lead atom in both valence and conduction bands enhances the spin-orbit interaction. The resulting band splitting is more pronounced in the conduction band, being at ≈ 1.3 eV at the R point. The corresponding value for the valence band is ≈ 0.6 eV. Therefore, the spin-orbit interaction has a significant contribution to reducing the band gap energy, thus the energy of the primary $E_{1/2,g} \rightarrow E_{1/2,u}$ optical transition.¹ It is also the reason behind the positive tem-

¹Although the DFT calculations reproduce well the shape of the bands, the band gap values obtained with this method are often significantly underestimated [Onida 2002]. Therefore, the

perature coefficient of the band gap, which is in contrast with the majority of semiconductor materials. Due to a large volume coefficient for the thermal expansion ($\simeq 1.35 \times 10^{-4} \text{ K}^{-1}$ 50 times more than in the crystalline silicon), the interactions within the inorganic lattice are significantly weakened with increasing temperature. The resulting increase of separation between the band extrema leads to a blue-shift of the band gap [Huang 2013, Singh 2016].

As a result of the saddle-point nature of the M point, the carriers created by photons of different energies at M point and along $M \rightarrow R$ path can relax towards the R point. This is schematically presented in Fig 1.8 (c). As proposed by Even et al. [Even 2014b], this process can be assisted by the acoustic phonons or coupling to collective molecular rotations. As the secondary $F_{3/2,g} \rightarrow E_{1/2,u}$, $E_{1/2,g} \rightarrow F_{3/2,u}$ transitions are also optically allowed, is assumed that part of the carriers generated by light at the R point can remain trapped in spin-orbit split $F_{3/2,g}$ and $F_{3/2,u}$ states. For these states, Even et al. propose optical phonon assisted intraband relaxation processes $F_{3/2,g} \rightarrow E_{1/2,g}$ and $F_{3/2,u} \rightarrow E_{1/2,u}$. Such hot-carrier-cooling has been already observed in time resolved studies of MAPbI₃ [Stranks 2013].

Similar, symmetric band structures with direct band gaps were obtained from the calculations performed for other cubic phase Methylammonium lead trihalides [Even 2014b, Even 2014a] and for fully inorganic CsPbI₃ [Even 2013]. A close analogy to the MAPbI₃ band structure has been demonstrated for MAPbCl₃, reproducing band gaps at the R and M points of the Brillouin zone [Even 2014b].

Such multivalley and multiple band gap band structure in organic-inorganic perovskites explains the efficient broadband absorption reported for these compounds. The theoretical calculations described above are confirmed with numerous measurements of the absorption coefficient, which reveal the existence of both low- and high-energy band gaps [Green 2015b, Brenner 2016]. The experimentally determined room-temperature absorption coefficient of MAPbI₃ is presented in Fig. 1.9, compared with the results obtained for c-Si and GaAs, the reference photovoltaic materials. Due to relatively high band gap, the infrared absorption of the MAPbI₃ is low. However, in the visible spectral range, where the energy density of the solar radiation is highest, the absorption coefficient of MAPbI₃ is comparable to that from GaAs, and is more than order of magnitude larger than in Si. Therefore, the light absorbing perovskite layers in solar cells can have relatively low thickness, which allows to design semi-transparent photovoltaic devices.

1.4.2 Carrier diffusion lengths and mobilities

The parameter determining the ability of photocreated free carriers to move within the crystal is the diffusion length, given by:

$$L = \sqrt{\frac{e\tau\gamma}{k_B T}} \quad (1.9)$$

bands in Fig. 1.8 (b) have been shifted upwards by 1.4 eV in order to correspond to the experimental value for the low-energy bandgap at the R-point [Even 2014b].

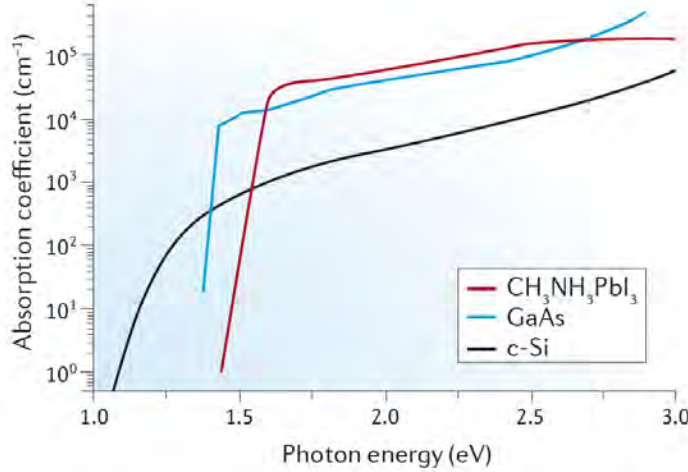


Figure 1.9: Absorption coefficient α of MAPbI_3 and $\text{MAPbCl}_x\text{I}_{3-x}$ compared to other solar cell materials. After Reference [Brenner 2016].

where τ , m^* , T are the carrier recombination lifetime, the effective mass of the carrier and the absolute temperature, respectively, and $\gamma = \frac{e\bar{\tau}}{m^*}$ is the mobility of the carriers, where $\bar{\tau}$ is the average scattering time.

The diffusion lengths and carrier lifetimes of the order of 100 nm and 10 ns in MAPbI_3 were reported by Xing et al. [Xing 2013] and Stranks et al. [Stranks 2013]. Remarkably, for a mixed halide with meager chlorine doping, namely $\text{MAPbCl}_x\text{I}_{3-x}$, Stranks et al. demonstrated a significant rise in the decay time to $\tau \simeq 270$ ns and diffusion lengths increased to around 1 μm for electrons and 1.2 μm for holes [Stranks 2013]. This result explains enhanced photon conversion efficiencies obtained in the $\text{MAPbCl}_x\text{I}_{3-x}$ solar cells, which can be attributed to the enlargement in the size of crystalline grains. The carrier diffusion properties further benefit from improving the material quality with increasing grain size from the microscopic to the millimeter range. For such macroscopic crystals, the diffusion lengths as long as 10 μm were reported [Dong 2015, Shi 2015].

In their studies, both Stranks et al. [Stranks 2013] and Xing et al. [Xing 2013] investigated the photoluminescence decay time after the excitation pulse. They compared the carrier lifetime in the perovskite films covered with PMMA and the materials absorbing electrons (PCBM) or holes (Spiro-OMeTAD), commonly used for the photovoltaic devices. The selected results of Stranks et al. [Stranks 2013] are shown in Fig. 1.10. The presence of the carrier absorbers reduces the radiative lifetime by up to two orders of magnitude. This is evidence that even in the films as thick as 200 nm or more [Stranks 2013], the majority of the carriers are successfully transferred from the photoactive material to the absorbers within several nanoseconds².

²The relative effectiveness of the intrinsic extraction of carriers from the perovskite layer has

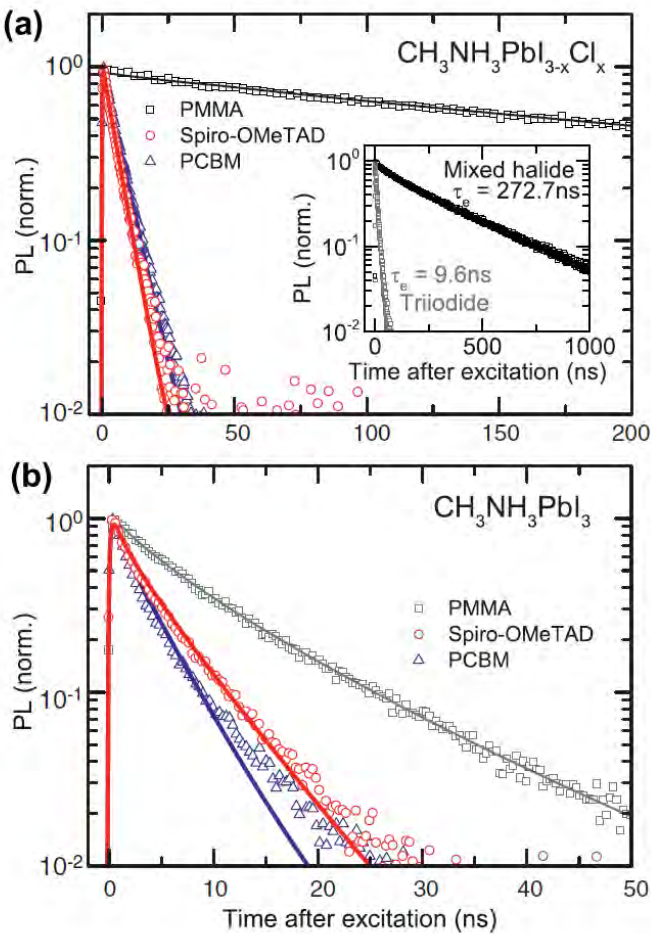


Figure 1.10: Time-resolved PL measurements taken at the peak emission wavelength of the MAPbI_3 (a) and $\text{MAPbCl}_x\text{I}_{3-x}$ (b) an electron (PCBM; blue triangles) or hole (Spiro-OMeTAD; red circles) quencher layer, along with stretched exponential fits to the PMMA data (black squares) and fits to the quenching samples by using the one- dimensional diffusion model. Inset: comparison of the PL decay of the two perovskites (with PMMA) on a longer time scale. After Reference [Stranks 2013].

On the other hand, the experimental estimations for the electron mobility in the hybrid perovskites are only $\leq 100 \text{ cm}^2\text{V}^{-1}\text{s}^{-1}$ either in the thin films [Stoumpos 2013] or high-quality macroscopic monocrystals [Dong 2015, Shi 2015]. Therefore, in the terms of mobility, even the high quality organic - inorganic perovskites are positioned closer to the other solution-processed materials than the epitaxially grown semiconductors, despite low effective masses [Brenner 2015].

This leads to the conclusion that the large diffusion lengths (Equation 1.9) in the

been demonstrated with the simplified, hole-absorber-free design of MAPbI_3 solar cell, revealing the efficiency of 5.5% [Etgar 2012]

hybrid perovskites originate from the long carrier lifetimes due to the low recombination rates (see Section 1.3.2 for proposed cation-dynamics related mechanism for the enhanced carrier lifetime). Reaching up to $10\ \mu\text{m}$, the diffusion lengths observed in the high quality perovskites crystals are comparable to those reported for the doped GaAs [Aukerman 1967, Edelman 1992], one of the leading photovoltaic materials, achieving record PCEs close to 29% [Green 2015a]. Therefore, considering the carrier extraction efficiency, the hybrid perovskites are better than other inexpensive low-temperature solution-processed materials, where the poor crystalline quality is the limiting factor [Facchetti 2011, Selinsky 2013]. The diffusion lengths in the organic conjugated compounds are of the order of only 10 nm [Haugeneder 1999, Shaw 2008, Kroese 2003]. Thus, the PCEs in such dye sensitized materials, suffering from carrier scattering and recombination losses, are limited to 12% despite the efficient light absorption [Wang 2015c, Han 2012, Chiba 2006]. The record PCE recently reported for a mixed-cation perovskite device is approximately two times higher [Saliba 2016b].

1.5 The evolution of hybrid perovskite materials

The undergoing development of hybrid perovskite materials is driven by the requirements of the photovoltaic applications. Two most important aims can be distinguished:

- 1) Further improvement of the photon conversion efficiency (PCE) by the adjustment of the band gap energy either for the single or multiple junction architecture and optimizing the material's optoelectronic properties and improving its morphology.
- 2) Achievement of the long-term structural stability under operational conditions.

1.5.1 Towards the perovskite solar cells: the requirements for the photoactive material

The optimal band gap energy. The band gap of silicon (1.1 eV) is considered to be the optimal band gap for a single junction solar cell [Shockley 1961]. Therefore, for a further increase of the PCEs in the single-junction architectures, the relatively high band gaps of the hybrid perovskites (e.g. 1.6 eV in MAPbI_3) should be tuned towards lower values by varying the ionic composition. On the other hand, a concept of a tandem silicon-perovskite solar cell was recently proposed in order to fully exploit the perovskites' excellent absorption properties in the visible spectral range [Sivaram 2015, Bailie 2015]. In such architecture, the top, thin perovskite film cell harvests the high-energy part of the solar spectrum, while the silicon cell below absorbs the low energy range. The combined PCEs for these tandem devices are expected to reach 30% [Sivaram 2015, McMeekin 2016]. The current-match of both junctions requires a perovskite band gap of 1.75 eV [Shah 1999], which, as shown before, can be tuned to this value simply by manipulation of the halide content (see Section 1.3.1).

The role of the morphology: homogeneity and structural defects. The importance of the material morphology in the microscopic scale has been demonstrated with the recent studies of the high quality, millimeter-sized Methylammonium trihalide crystals [Valverde-Chavez 2015, Dong 2015, Shi 2015]. Grown from solution in the epitaxial regime, these structures show significantly improved electronic properties when compared to thin films (see also Section 1.4.2) [Dong 2015, Shi 2015]. Films, due to their spin-coated nature, reveal a higher level of inhomogeneity and larger density of defects at the surface or grain boundaries [Shkrob 2014]. Apart from disturbing the charge diffusion properties, the non-optimized crystal morphology results in the limited reproducibility of the perovskite solar cells. The PCEs of the perovskite-based devices usually vary around several per cents from the average value, even for the units fabricated in the same series [Jeon 2014].

Therefore, it is crucial to optimize both material properties and preparation techniques, in order to obtain possibly uniform, defect-free perovskite thin layers.

Long-term stability of the perovskite structure. The most important mechanisms causing the degradation of the hybrid perovskite materials are presented in Section 1.3.4. Sensitive to the humidity, light and raised temperatures, the majority of the hybrid perovskites degrade within days to weeks even if incorporated into a full solar cell architecture [Leijtens 2015]. As the commercial demand is a solar cell stable at temperatures as high as 85° C over a period of 25 years [Leijtens 2015], it is essential to develop significantly more stable perovskite materials. Moreover, this robustness has to be combined with excellent electronic properties, resulting in the PCEs not worse than in the silicon-based competitors.

1.5.2 The perovskite light absorbers beyond MAPbI_3

With the band gap of 1.6 eV and a poor resistance towards raised temperature and atmospheric factors, the archetypal MAPbI_3 compound does not reveal the desired properties of the photovoltaic absorber listed above. Therefore, the possibilities of applying alternative hybrid perovskite compounds have been explored. Here, we present several of these materials, which have been investigated in this thesis. We briefly discuss their properties, pointing out the advantages and disadvantages with respect to the photovoltaic applications.

The materials derived from MAPbI_3 . The mixed halide $\text{MAPbCl}_x\text{I}_{3-x}$ is obtained through the synthesis of the MAPbI_3 in the presence of chlorine-containing precursors [Dar 2014, Deschler 2014]. As the introduced chlorine atoms are relatively small and the level of doping is intentionally low, the band gap of the mixed halide should intuitively be slightly higher than in the MAPbI_3 . Instead, a red-shift of around 50 meV is observed. Additionally, the carrier diffusion lengths are larger by an order of magnitude with respect to the MAPbI_3 , along with the increased size of the crystalline grains (see also Section 1.4.2). The exact mechanism responsible for such a significant change in the electronic properties and the amount of effectively incorporated chlorine atoms are still under debate [Dar 2014, wook Park 2015, Binek 2016]. One of the proposed explanations suggests the initial crystallization

of the MAPbCl₃ on the substrate. This induces the growth of the MAPbI₃ with modified lattice properties, resulting in a band gap value lowered towards the single-junction optimum and improved morphology [Binek 2016]. Therefore, the efficiencies of such mixed-halide based solar devices exceed the results obtained for the conventional MAPbI₃ units by 2 % on average.

Encouraging results were also obtained by introducing small metal Al³⁺ cations into the MAPbI₃ lattice [Wang 2016]. At the doping level of 0.1%, the band gap remains unchanged, while the increased PCE of MAPbI₃:Al solar cells (the record value of 19.1 %) results from the improved uniformity and surface smoothness in the film [Wang 2016].

Therefore, with the proper control of the morphology and electronic properties, there are perspectives for exceeding 20 % PCE with the devices based on iodine- and Methylammonium-rich materials. However, it is important to note that their thermal stability is similarly insufficient as in the MAPbI₃ archetype.

FAPbI₃. The perspectives for the further improvement of the electronic properties arise with the substitution of Methylammonium with Formamidinium cations (see also Section 1.3.2). Compared to MAPbI₃, the Formamidinium analogue FAPbI₃ has a band gap significantly lowered towards the single-junction optimum (\approx 1.5 eV) and diffusion lengths increased by at least the factor of two ($>200\text{ }\mu\text{m}$) [Eperon 2014b]. Moreover, this compound is capable of resisting temperatures of 160° C [Koh 2014]. However, the formation of the photoinactive δ -phase inclusions in FAPbI₃ cannot be completely avoided during the synthesis, and its amount increases with time [Pellet 2014, Jeon 2015]. As a result, both absorption and carrier diffusion properties suffer from the presence of the non-perovskite fraction, limiting the photon conversion efficiency to around 16 % [Eperon 2014b, Koh 2014].

Tri-bromides: MAPbBr₃ and FAPbBr₃. In contrast, the organo lead tri-bromides MAPbBr₃ and FAPbBr₃, forming the cubic phase of the low distortion level, reveal both structural stability and low degradation rate under the operational conditions [Noh 2013, Zheng 2016]. Though, with the band gap energies of around 2.2-2.3 eV, the PCEs of solar cells based on the these materials will be significantly worse than in the silicon devices.

Therefore, neither the archetypal MAPbI₃ and its derivatives, nor the homogenous-cation perovskite compounds can offer both durability and perspectives for the high efficiency. A considerable progress was achieved with the stabilization of the photoactive structure in the most promising candidate for the photovoltaic applications, FAPbI₃, by alloying it with the robust representatives of the hybrid perovskite family. As further shown, the approach of combining both different cations and anions allows to join the advantages of the pure-ion materials, while the propagation of the factors which limit the PCEs is reduced.

1.5.3 A key to the stability: mixed-cation mixed-halide hybrid perovskites

In order to stabilize the perovskite phase of the FAPbI_3 , the level of the structural distortion must be reduced, resulting in more a cubic-like character of the lattice. This can be achieved by the partial substitution of Formamidinium with smaller cations, like the Methylammonium molecules or caesium atoms. Following this idea, the $(\text{FAPbI}_3)_{1-x}(\text{MAPbBr}_3)_x$ alloys were intensively studied during the last two years. Jeon et al. have reported the stabilization of the photoactive perovskite phase already at $x = 0.15$ [Jeon 2015]. Soon after, the $(\text{FAPbI}_3)_{0.83}(\text{MAPbBr}_3)_{0.17}$ was reported as the composition of the optimal stoichiometric proportions of the host and substituting ions [Correa Baena 2015], which has been reproduced in the later studies [Bi 2016, Saliba 2016c, Saliba 2016b]. All this work acknowledges the numerous advantages of such alloys over the pure FAPbI_3 , resulting in the superior PCEs (the record yields 21 % [Green 2015a]) despite the bromine-induced blueshift of the band gap to around 1.65 eV. Among these benefits are the increased photocurrents and small hysteresis in the $J - V$ curves.. Moreover, the $\text{FAPbI}_3\text{-MAPbBr}_3$ compounds reveal improved crystal morphology when compared to FAPbI_3 , revealed in smoother surface with reduced voids between the grain boundaries [Jeon 2015].

Consequently, the triple-cation mixed compounds containing relatively small caesium atoms were proposed as the next step towards the ideal, undistorted cubic structure. Saliba et al. have investigated the $\text{Cs}_x(\text{MA}_{0.17}\text{FA}_{0.83})_{100-x}\text{Br}_{0.17}\text{I}_{0.83}$ materials, determining the optimal caesium content at $x = 0.05$ [Saliba 2016b]. Such composition leads to further reduction of the photoinactive inclusions, resulting in superior reproducibility of the solar cells and low degradation rate [Eperon 2014a, Saliba 2016b].

In parallel, the caesium - organic cation mixed compounds, the Cs/FA and Cs/MA, are developed for tandem silicon - perovskite solar cell applications [Lee 2015, Beal 2016, McMeekin 2016]. According to the studies of the $\text{Cs}_{0.17}\text{FA}_{0.83}(\text{Br}_x\text{I}_{1-x})_3$ family by McMeekin et al., the optimal 1.74 eV band gap is reached at $x = 0.4$ [McMeekin 2016]. The band gap energy is widened partially by the presence of small Cs atoms with reduced bromine content. This allows to avoid the problem of structural stability and crystalline quality at around $x = 0.6$, where the lattice transforms to bromide-like cubic phase [Rehman 2015]. Simultaneously, the significance of the halide segregation (see also Section 1.3.1) is reduced.

One of the most recent works reports on the incorporation of an additional element, rubidium, into the lattices of previously studied hybrid perovskites [Saliba 2016a]. The compound of four mixed A-cations (Cs-Rb-MA-FA) was found capable of passing the standardized durability tests required for the photovoltaic devices. Moreover, it was suggested that the observed degradation originates from a non-optimized architecture rather than insufficient stability of the perovskite absorber. This strongly suggests, that the development of complex, multi-cation materials is currently the leading trend towards the commercialization of perovskite-based photovoltaics. Nevertheless, to predict the properties of newly designed compounds, a full understand-

ing of the fundamental properties and morphology in the pioneering, prototype compounds is required, which is the aim of this thesis.

CHAPTER 2

Experimental techniques

Contents

2.1	Spectroscopy in high magnetic field	25
2.1.1	Pulsed magnetic field generation	25
2.1.2	Transmission measurements	28
2.1.3	Temporal synchronization	31
2.2	Micro-Photoluminescence measurements	32

This chapter describes the experimental techniques used to obtain the results presented in this thesis. In the first part, the generation of the pulsed magnetic fields and the magneto transmission measurements are presented. In the second part, the micro-photoluminescence measurements performed in the absence of magnetic field are discussed.

2.1 Spectroscopy in high magnetic field

All measurements in pulsed magnetic fields have been performed in the Laboratoire National des Champs Magnétiques Intenses (LNCMI), Centre National de la Recherche Scientifique (CNRS), Toulouse, France. The LNCMI in Toulouse is one of the worlds leading facilities in pulsed magnetic field generation. Pulsed techniques allow to obtain magnetic field intensities beyond the limits of the superconducting (22 T) and resistive DC field magnets (38 T). Currently, LNCMI produces magnetic fields exceeding 90 T with non-destructive long pulses, and up to 150 T using the semi - destructive, ultrashort pulses. The laboratory serves as a user facility, providing access to high magnetic fields for users from laboratories around the world. The main research topic is solid state physics, including superconductivity and the electronic properties of semiconductors, investigated with transport and spectroscopic methods in the temperature range from 100 mK to 300 K. Additionally, the high accuracy measurements of magnetic birefringence of vacuum and the investigation the atomic levels in rubidium gas for the future applications in magnetometry are being developed.

2.1.1 Pulsed magnetic field generation

The elements of pulsed magnetic field installation in Toulouse are presented in Fig 2.1. The pulsed magnetic field is obtained by an electric discharge into a resistive

coil. The electrical energy, prior to discharge into a coil, is stored in a capacitor bank (Fig.2.1 (a)). The resistive coil magnets, made of copper alloy wires, are placed in cryostats, filled with liquid nitrogen, as shown in (Fig.2.1 (b)). Inside the magnet bore, an inner helium bath cryostat is installed, with a variable temperature insert (VTI) allowing the measurements between 1.5 and 300 K [LNCMP-team 2004]. The investigated sample is inserted into the cryostat with a light transmitting probe, which also allows the monitoring of the experimental conditions (temperature, magnetic field). A complete experimental setup is presented in the Fig. 2.1 (c).

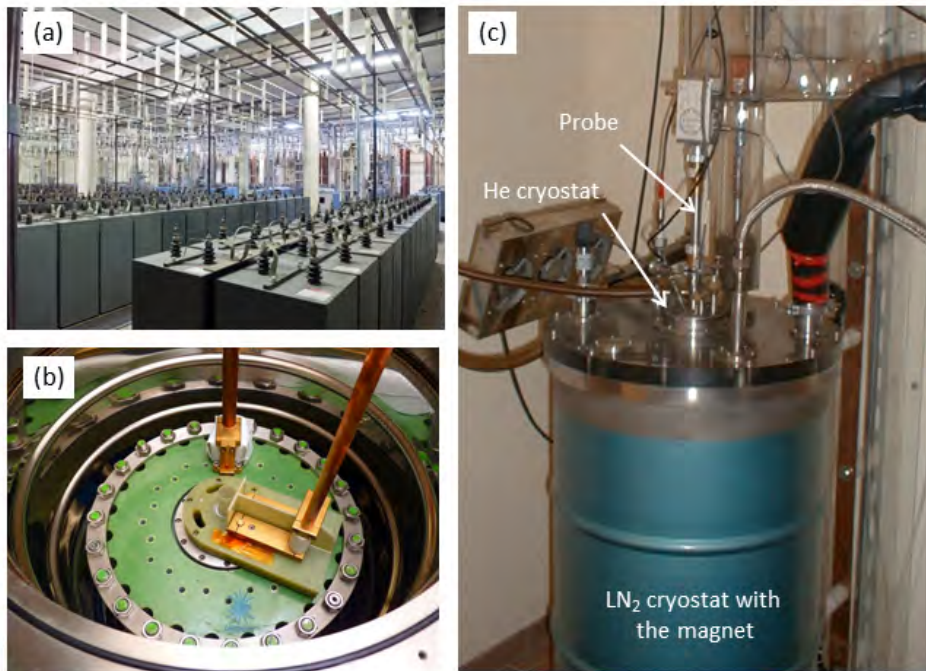


Figure 2.1: (a) the 14 MJ capacitor bank (b) a resistive coil mounted in a cryostat (c) a complete experimental setup with a probe placed in helium bath cryostat.

The 14 MJ generator (Fig.2.1 (a)) serves as the main power supply at LNCMI Toulouse. It consists of 14 capacitor bank units, each storing up to 1 MJ energy. The capacitors are synchronized to discharge simultaneously when the pulse of magnetic field is triggered.

The resistive coils are designed and manufactured in-house within the LNCMI technical workshop. The most important requirement for the coil is the ability to survive the high magnetic pressure, which originates from the Lorentz force acting on the charge carriers moving in the coil wire. The coil is exposed to a mechanical strain, both tangential expansion and axial compression, proportional to B^2 , which limit the value of the magnetic field that can be generated, due to the mechanical durability of the system - for a review see Ref. [Debray 2013]. The materials and design used at present routinely allow the generation of magnetic fields up to 70 T with a single

coil. An energy discharge exceeding the construction limit for the particular coil causes an abrupt burst of the magnet, resulting in a destructive explosion. To go beyond the 70 T limit in the non-destructive long pulse experiment, magnetic fields generated by multiple, coaxial coils are combined. At present, the magnetic field intensities in the region of 90 T are available with a dual coil installation.

Typical temporal profiles of the magnetic field, generated with several long pulse coils available at LNCMI Toulouse are presented in Fig. 2.2. The duration of the single coil pulse varies from a few tens to several hundred of milliseconds, depending on the coil size and design. The temporal profile of a dual coil magnet has a short and a long component, associated with the discharges in the inner and outer coil, respectively [Jones 2004], as shown with the red curve on Fig. 2.2. The dual coil system requires two synchronized generators: 12 MJ energy from the main generator supplies the outer coil (maximally 34 T at 700 ms pulse duration), while the inner coil (maximally 62 T, pulse duration of 25 ms) is powered with 1.15 MJ from the additional, 6 MJ capacitor bank [Béard 2012]. The maxima of the pulses are synchronized, inducing 91 T in an effective 9.5 ms combined pulse. All the results presented in this work were obtained with the 70 T magnet (the typical temporal profiles are shown with orange and blue curves).

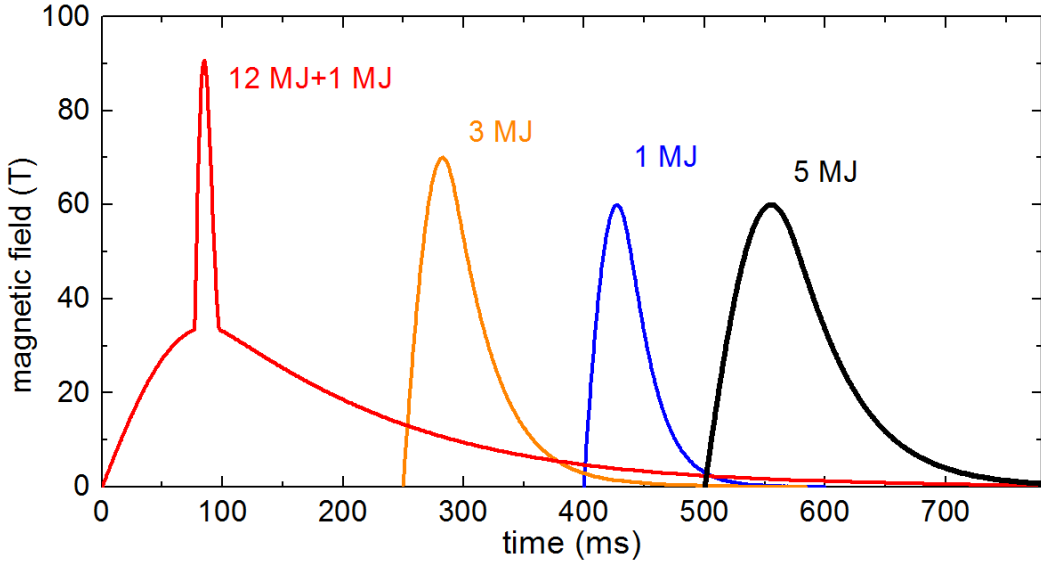


Figure 2.2: Temporal profiles of typical magnetic field pulses. Magnetic field as a function of time obtained for different coil systems at the maximal energies available for each system. The curves are offset horizontally for clarity.

The solutions used in the design of the pulsed magnetic field coils are presented in Fig. 2.3. Panel (a) shows a copper alloy fiber of rectangular cross-section used to wind the coil with approximately 1000 turns. The wires are additionally rein-

forced with an outer shell of Zylon fibres. Such wires combine mechanical durability [Spencer 2004] with low electrical resistivity, typically of the order of $\rho = 10^{-9}\Omega \cdot \text{m}$ at liquid nitrogen temperature. For a further reinforcement of the magnet construction, and to minimize the impact of a possible explosion due to the magnetic pressure, the coil is placed in a cage of metallic rods (Fig.2.3 (b)), supported by bottom and top flanges.

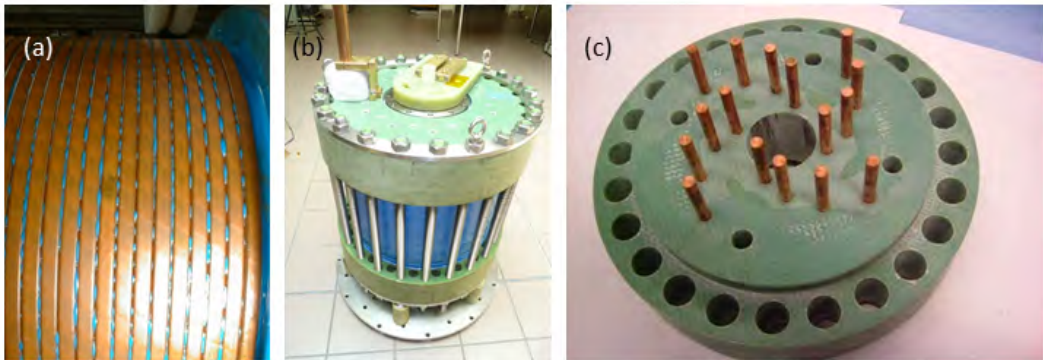


Figure 2.3: The coil construction details: (a) a rectangular cross-section copper composite wire, (b) a dual- coil magnet system in flanges and reinforcing cage, (c) top flange with copper cooling fingers.

In order to reduce the time between the high-energy magnetic field pulses, a fast-cooling design of the magnet has been developed [Frings 2008]. Due to the energy dissipation caused by resistive losses in the coil wire, the temperature of the magnet rises considerably after each pulse. For example, during the electric discharge at a voltage of 20 kV, the temperature of the 70 T coil (resistance 50 m Ω at $T = 77\text{ K}$) rises by more than 100 K. As a result, the coil resistance increases approximately by a factor of 2. The cooling time ranges from several minutes to 3 hours, depending on the energy of the pulse, coil type and size. The fast-cooling design uses the cooling fingers for improved thermal contact (Fig.2.3 (c)) and vertical channels for enhanced nitrogen circulation. As a result, the time between the 70 T pulses is shortened by half, to around 60 minutes, which is a significant advantage for measurements. The cooling time can be further reduced by decreasing the temperature of the liquid nitrogen, for example by pumping.

2.1.2 Transmission measurements

In the magneto - transmission measurements, white light is passed through a sample placed in the magnetic field. A schematic representation of the transmission setup is presented in Fig. 2.4. The sample is mounted on a probe, which is placed in a helium bath cryostat, inserted into the magnet bore. The available temperature range is from 1.5 K (pumped helium conditions) to 300 K. The incoming and outgoing beams are transmitted using optical fibres. The signal is dispersed in a monochromator

equipped with a diffraction grating and acquired using a CCD camera, which is synchronized with the magnetic field pulse.

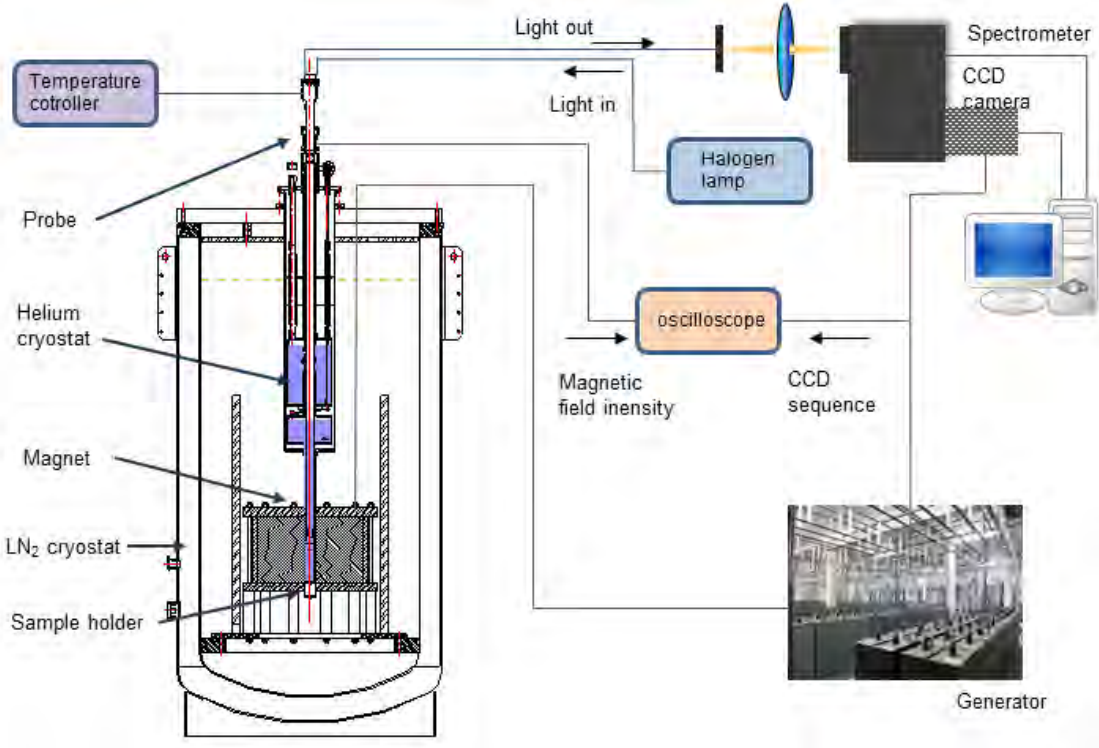


Figure 2.4: Schematic representation of the setup used for transmission measurements in pulsed magnetic fields.

An image of the magneto - transmission probe used for the experiments is presented in Fig. 2.5 (a). In order to avoid the formation of eddy currents in high magnetic field, all the materials used for the fabrication of the high-field exposed parts are electrical insulators. The lower part of the probe, which is inserted into the magnet, consists of a 7 mm diameter rod and a ceramic sample holder. The rod is made of low thermal conductivity (below $1 \frac{W}{m \cdot K}$) and low thermal expansion coefficient (less than 1% between 4 K and 300 K) epoxy fiberglass. A vertical translation of the rod is possible thanks to a moveable o-ring, sealing the connection between the probe and the inner cryostat. The sliding seal allows the position of the sample to be adjusted to be exactly in the center of the magnetic field.

A close-up of the sample holder is shown in the Fig. 2.5 (b). Apart from the optical components, a Cernox thermometer and a pick-up coil are mounted close to the sample. The thermometer is calibrated with an accuracy of ± 0.1 K using a reference Cernox and a platinum resistor. The temperature of the experiment is monitored by a LakeShore temperature controller. The ambient temperature of the cryostat is 77 K, determined by the presence of liquid nitrogen in the outer cryostat.

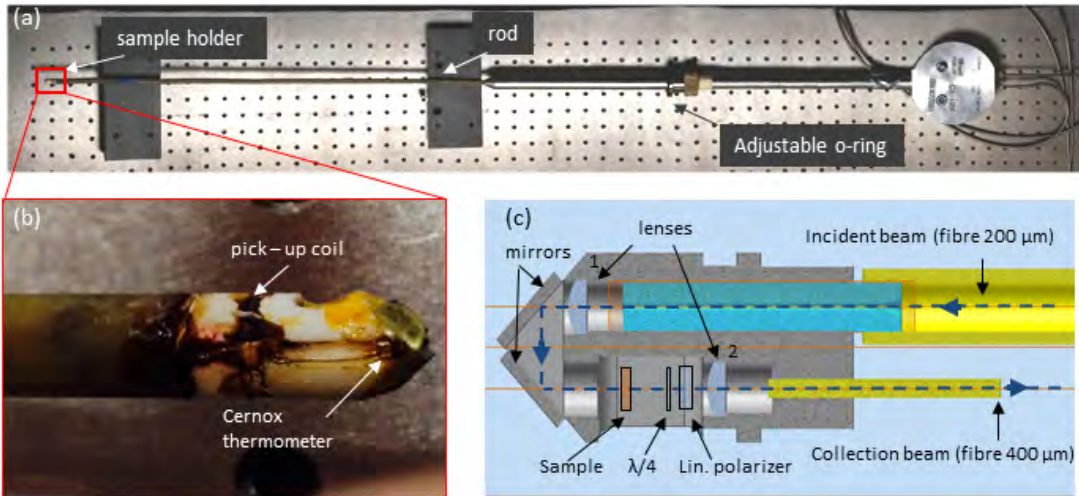


Figure 2.5: (a) The photo of the magneto-transmission probe. (b) The magnified phot of sample holder (c) as scheme of the optical path in the holder.

In the case of low temperature measurements, the VTI is filled with helium, which becomes superfluid when cooled down to below 2 K by pumping. Temperatures above 77 K are stabilized with a heater, mounted inside the VTI insert of the helium cryostat.

A pick-up coil is used to monitor the value of magnetic field in the position of the sample as a function of time. It is formed by 100 turns of an insulated 50 μm diameter copper wire. The voltage induced in the pick-up coil during the magnetic pulse is the derivative of the magnetic flux. The temporal profile of magnetic field is obtained from the integrated pick-up voltage divided by the area of the coil. The effective area of the pick-up coil (0.00318 m^2) is defined with 2% accuracy. To measure this parameter, the pick-up coil is placed in the center of a long ($\approx 1 \text{ m}$) calibration coil, with a known $B(I)$ dependence. A sinusoidal magnetic field is induced in the calibration coil using the oscillator output of a lock-in amplifier, which also records the pick-up coil response. The area of the pick-up coil is calculated as the linear coefficient in the $V(\frac{dB}{dt})$ dependence.

The pick - up coil is also used to exactly position the sample in the center of magnetic field. An alternating current generated by the oscillator output of a lock-in amplifier is applied to the pulsed field coil. The probe is moved up and down along the magnet bore to find at the position at which the maximum of induced pick-up signal occurs.

The optical path in the sample holder is schematically shown in the Fig. 2.5 (c) with the dark blue dashed line. The white light is coupled to a 200 μm multimode optical fibre and collimated by a lens (1). A set of two gold mirrors reflects the beam to the sample space. The light transmitted through the sample is focused

by a second lens (2) onto the 400 μm multimode fibre, which guides the signal to the spectrometer. To obtain polarization resolved data, a circular polarization analyzer is placed in the optical beam between the sample and lens (2). The analyzer consists of a lambda quarter waveplate, the axis of which is rotated by $(45 \pm 2)^\circ$ with respect to the axis of a linear polarizer. For each spectral region, a suitable analyzer, with circular polarization degree of at least 90 %, is mounted. To measure both σ^\pm circular polarizations, the direction of the magnetic field is reversed. The low thickness (below 0.3 mm) of the polarization optics limits the impact of the Faraday effect. Additionally, the transmission probe was also used for temperature dependence transmission measurements in the absence of magnetic field.

2.1.3 Temporal synchronization

As the 70 T pulse lasts only 150 ms, the time to acquire spectra at a particular value of magnetic field is limited to several milliseconds. Therefore, the temporal synchronization of magnetic pulse with the data collection is crucial. An example of a spectral acquisition series recorded during a 68 T magnetic pulse is presented in Fig. 2.6. The sequence of 30 CCD acquisitions, each lasting 3 ms (CCD trigger is indicated by the blue line) and the pick-up coil signal (orange curve) are plotted as a function of time. The pulse is triggered at $t = 0$. After the integration of the pick-up coil signal, the temporal profile of magnetic field is obtained (black curve). Each acquisition in the sequence can be then associated with the corresponding magnetic field intensity, which is calculated as an average of the values recorded at the beginning and the end of the acquisition frame. The duration of a single acquisition cannot be below 3 ms, as the CCD triggering becomes unstable for shorter times. The fast read-out time of the CCD detector (13 ms repetition rate with 3 ms acquisition) enables the collection of up to a dozen spectra at different magnetic field values during a single 150 ms pulse.

Synchronization of the magnetic field with the data collection is achieved by setting the delay of the magnetic field pulse with respect to the start of the CCD acquisitions. The exact value of the delay time is fixed with the precision of 0.1 ms during a series of test pulses, where the delay is adjusted so that the maximum of the magnetic field occurs in the middle of one of the acquisition frames (see inset in Fig. 2.6). This ensures that a spectrum is acquired at the maximum of the magnetic field. We use a synchronization sequence as shown in the 2.7. The CCD camera is used as a master trigger. The measurement starts when the generator sends a pre-trigger pulse to the CCD. Afterwards, the CCD camera produces a series of acquisition pulses, which is passed to the waveform generator to be formed into a TTL compatible rise signal. Simultaneously, the CCD shutter series is recorded on the oscilloscope together with the pick-up coil signal. The delay unit retards the TTL signal in order to record the first three acquisition frames without the presence of magnetic field. Finally, the magnetic pulse is released by a thyristor switch.

The temporal derivative of the magnetic field varies with the evolution of the pulse, as presented in Fig 2.6. The absolute value of this parameter is lowest at the

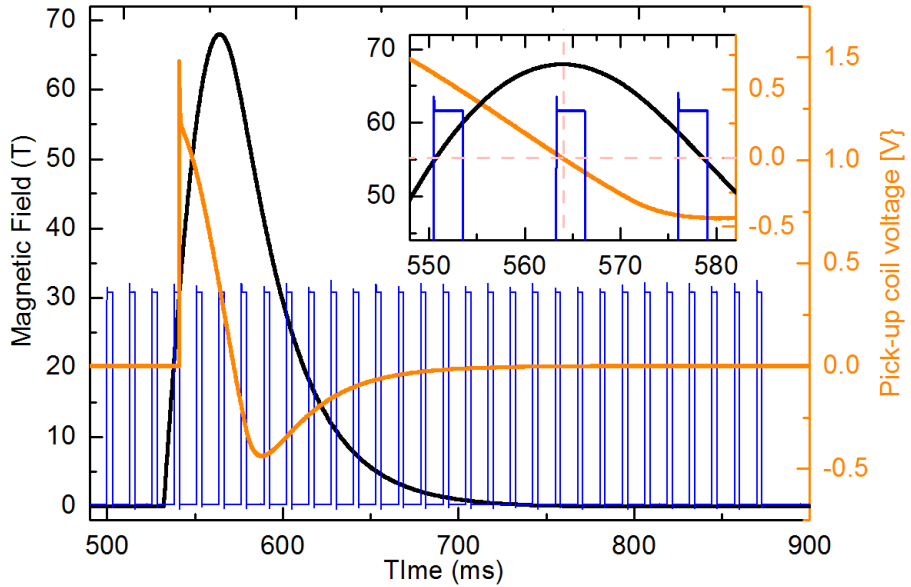


Figure 2.6: Sequence of 30 CCD acquisitions (in blue) and the pick-up coil signal (orange) during 67 T pulse, registered on the oscilloscope as a function of time. The calculated temporal profile of magnetic field is represented by the black curve. The inset shows the synchronization of the maximum of magnetic field with one of acquisition frames.

maximum of the field, and at the end of the pulse, for the magnetic fields below 30 T. In these regions, the spread between the extreme values of magnetic field occurring during a single acquisition frame does not exceed 0.5 T. In contrast, the data collected on the rising slope of the pulse, where the spread is in the range of 10 T, are not analyzed. Similar difficulty occurs for the intermediate values of magnetic field for the descending slope of the pulse. Due to the rapid drop of magnetic field from 55 T to 30 T, only one spectrum is acquired in this range. Therefore, a 70 T measurement is typically completed with another magnetic field pulse, with a maximum field of 50 to 52 T. Using data from both pulses, we obtain 15 spectra, separated by no more than 6T.

2.2 Micro-Photoluminescence measurements

In this section, spatially resolved μ -PL measurements are described. These measurements were performed in the absence of magnetic field in the laboratories of LNCMI CNRS, Toulouse, France, and LUMNP, Faculty of Physics, University of Warsaw, Poland. A schematic illustration of the μ PL experimental setup at LNCMI is presented in Fig. 2.8. The samples are placed in a helium gas flow optical cryostat, working in the temperature range from 4 to 500 K. The cryostat is bolted to the computer controlled, motorized x-y translation stages, allowing two-dimensional

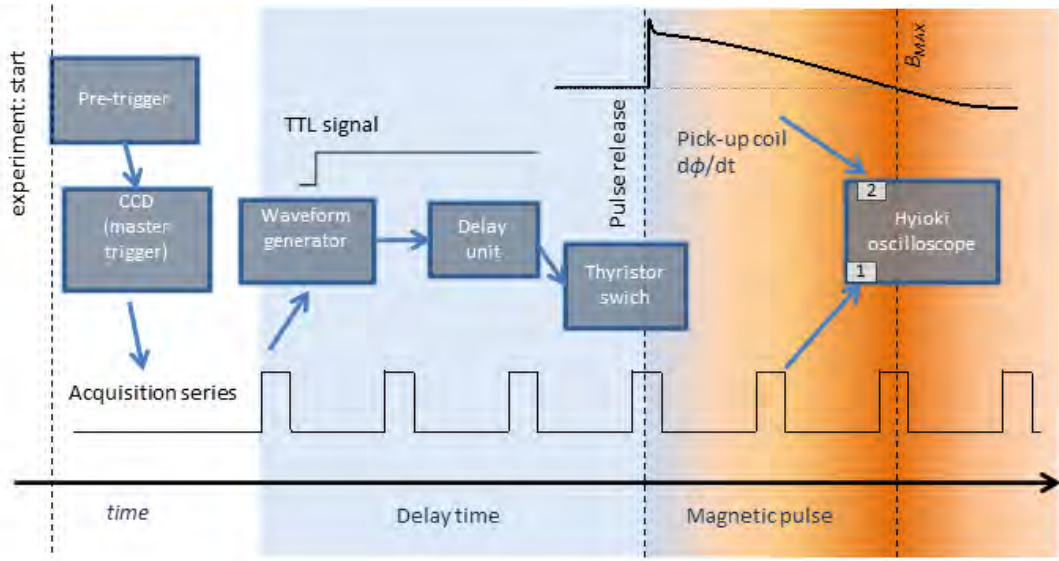


Figure 2.7: The schematic diagram of synchronization sequence for optical measurements in pulsed fields.

in-plane motion. The position of the stages is controlled with micrometer screws, either manually or by automatized stepper motors. It allows a macro-scale mapping of the sample surface with micrometer resolution. The effects of a motor backlash ($\approx 10\mu\text{m}$) is minimized by acquiring the spectra while always scanning in the same direction - in a similar manner as the scanning of a cathode ray tube television. The resolution of the system is not limited by the minimal step of the motor, which is 100 nm, but rather by the $1 \mu\text{m}$ spot size of the excitation.

Free beam optics in a backscattering configuration is used. The laser beam used for the excitation is split by a non-polarizing 50/50 cube or a dichroic filter. For excitation and collection of the signal, a microscope objective with long working distance (7 mm) is used. The objective has a numerical aperture of $\text{NA} = 0.55$ and the magnification is $50\times$. The size of the laser spot on the sample surface is of the order of $1 \mu\text{m}$. The photoluminescence signal is focused on a monochromator slit, then dispersed by a diffraction grating and acquired by nitrogen cooled CCD camera. The PL is excited with a semiconductor continuous wave 532 nm laser. For the materials with a higher band gap, Optical Parameter Oscillator (OPO) pumped by a tunable Ti:sapph laser is used for the excitation.

The μPL experimental setup in Warsaw is similar: The cryostat translation stages have a 45 mm of travel and are controlled manually with micrometer screws. For automatized surface mapping, the microscope objective is moved by piezo-controlled stages with a $160 \mu\text{m}$ range. The objective of $\text{NA} = 0.9$ numerical aperture has a 13 mm working distance and $100\times$ magnification. The CDD camera is cooled with the Peltier cell.

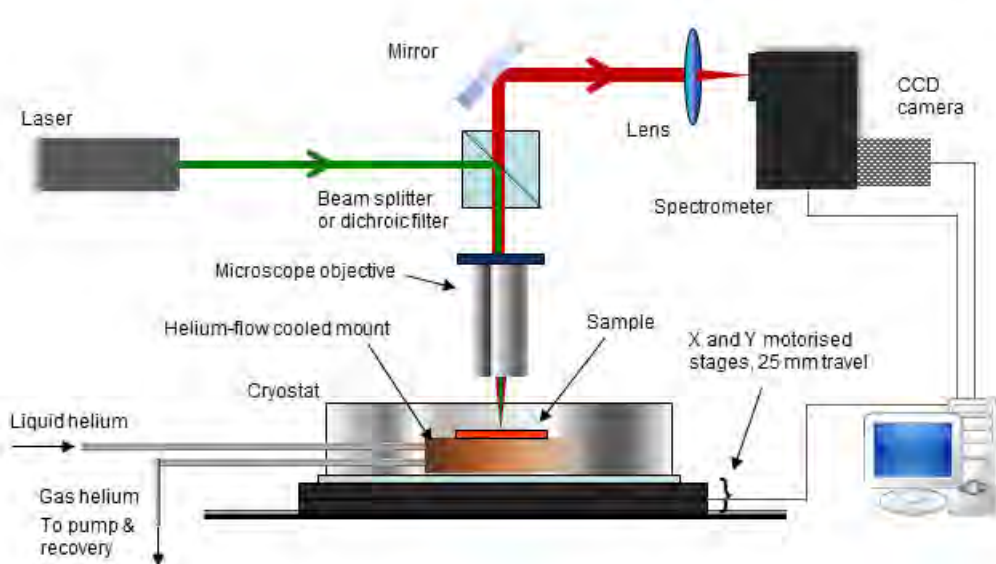


Figure 2.8: Schematic drawing of the μ PL experimental setup at LNCMI-T

CHAPTER 3

Preparation and characterization of the samples

Contents

3.1	Description of samples	35
3.2	Fabrication of the samples	36
3.3	Maintaining the perovskite phase	38
3.4	Sample characterization	40

In this chapter, we describe the fabrication of perovskite thin-film samples and how we characterize them prior to the measurements in magnetic field. First, we introduce the investigated compounds and the details of solution-process deposition methods used to synthesize the samples. Then, we discuss the procedures for conserving the thin films in the perovskite phase and discrimination between the pristine and degraded material. Finally, we present the results of the sample characterization, where we investigate the dependence of the band gap energy on the temperature.

3.1 Description of samples

The studies presented in this work were performed on several representatives of hybrid perovskite family. These were mostly recently synthesized materials, developed to improve the performance of the perovskite solar cells. We investigate the compounds based on Methylammonium ($MA = CH_2NH_3^+$) or Formamidinium ($FA = CH(NH_2)_2^+$) organic cations. We also distinguish two main groups with respect to the halide content: the iodine - based compounds and high band gap tribromides. Among the first group are the archetypal $MAPbI_3$, its Formamidinium analogue $FAPbI_3$ and the mixed halide $MAPbCl_xI_{3-x}$. Bromine - based materials are $FAPbBr_3$ and $MAPbBr_3$. All the samples were fabricated in the group of Professor Henry Snaith of the Clarendon Laboratory at the University of Oxford. The synthesis was performed by Giles E. Eperon, Thomas Stergiopoulos and Jacob Tse-Wei Wang.

The samples investigated in this thesis are thin films of the perovskite material deposited on glass substrates. The films are around 350 nm thick, which is comparable to the penetration depth of the visible light [Stranks 2013]. The thickness is uniform across the sample, and the material is free of pinhole-like defects. The



Figure 3.1: Photograph showing the typical Formamidinium - based samples with different halide content.

thickness of the substrate is 1 mm. In Fig 3.1 we present a photograph of three typical Formamidinium based samples used for our research. The differences in the halide content - changing from pure iodine to pure bromine - are responsible for the observed change in colour.

3.2 Fabrication of the samples

In this section, we present the techniques commonly used for the synthesis of the perovskite thin films. We focus on the description of the most popular, spin-coating methods, which were used to fabricate all the samples provided by the Clarendon Laboratory. A two-step approach was applied in the case of MAPbI₃ thin films, while the rest of the investigated compounds were obtained with a one-step deposition.

Solution deposition technique: one-step approach. In this process, the perovskite thin film is synthesized from a solution, containing the the salt precursors, which are the halide of organic cation AX and the lead di-halide PbX₂. The sequence of procedures in the simplest, one-step approach is presented in Fig. 3.2. The organic solvent with precursor salts is dripped onto the cleaned glass substrate. The mixture is then uniformly spread on the substrate through spin-coating. The subsequent anneal, in temperatures of the order of 100 °C, leads to the evaporation of the solvent and formation of the perovskite film.

The simplicity of spin-coating procedure comes along with the drawbacks of incomplete substrate coverage, leading mainly to pinhole-like defects and variable film thickness. These problems can be reduced by the proper control of the processing conditions, such as performing the film formation in nitrogen atmosphere, and lowering the annealing temperature to below 90 °C [Stranks 2013, Eperon 2014a]. Moreover, the size of the grains which form the perovskite film, can be increased by an order of magnitude, up to a few micrometers, by a rapid post-annealing procedure

at higher temperatures [Saliba 2014].

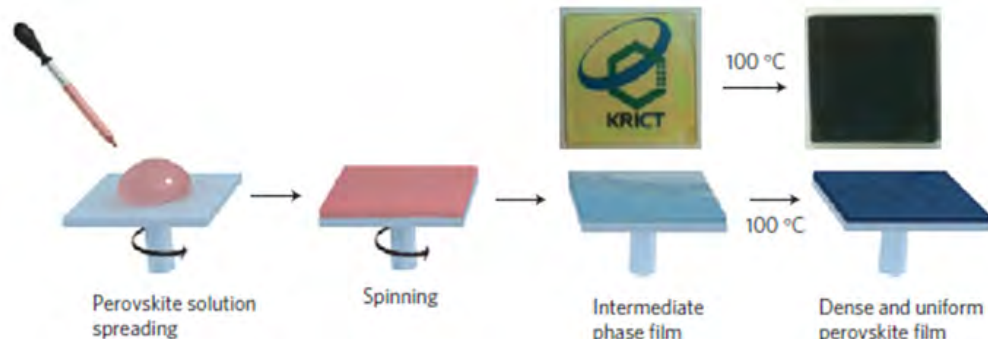


Figure 3.2: The sequence of procedures in the one-step perovskite deposition method. After the reference [Jeon 2014]

Solution deposition technique: two-step approach. A further improvement of the film morphology and increased coverage is provided by the two-step sequential deposition approach. In this process, the solvents with precursor salts are spin-coated one after another, which is schematically presented for the MAPbI_3 film formation in Fig 3.3. First, the layer of PbI_2 is spread on the substrate and dried. Then, the solution with MAI is spin-coated upon it, and the MAPbI_3 film then forms in several seconds.



Figure 3.3: A schematic representation of the two-step deposition method. Reprinted the reference [Stranks 2015]

Other synthesis methods At present, several derivative or related synthesis processes have been reported. An evolution of the two-step approach, namely the interdiffusion method based on sequential deposition of stacked bi-layers of precursor salts, was demonstrated to improve the surface smoothness [Xiao 2014, Chen 2014a]. The variation in the thickness can be minimized with evaporation techniques, which also enables the design of multijunction architectures [Liu 2013, Green 2014]. An overview on these and other current state-of-art perovskite synthesis methods is provided in the review article of S. D. Stranks et al. [Stranks 2015].

3.3 Maintaining the perovskite phase



Figure 3.4: A photograph showing decomposed MAPbI₃ sample with yellow PbI₂ precipitations.

The long-term stability of organic-inorganic perovskites has been discussed in detail in Chapter 1, together with the factors catalyzing the degradation of these materials. The majority of our perovskite samples can be exposed to normal atmospheric conditions for several months before decomposing to the reaction precursors. However, in order to ensure that the investigated perovskite film is preserved in the perovskite phase, we minimize the influence of the moisture and temperature during the storage period. The samples, which are vacuum-sealed for the transport, are placed in a vacuum box immediately after arrival. The samples are stored under a pressure of $\approx 10^{-5}$ bar and at an ambient temperature of 18° C. The perovskite films are exposed to the atmosphere only during preparation for the experiment, which lasts no longer than 30 minutes. The samples which have encountered any water condensation or increased moisture are not used for the further measurements.

We also analyze the samples for the first symptoms of the decay prior to the measurement. A visible evidence of sample degradation is the presence of the lead di-halides in the observed colours: yellow for PbI₂ and white for PbBr₂. A picture of a decomposed MAPbI₃ film, with yellow precipitations PbI₂, is shown in Fig. 3.4. After the first sign of a discrete, yellow halo was spotted in this sample, it has been exposed to the atmosphere for 10 months, which has caused a rapid progress in the degradation. However, if the inclusions of the di-halides can already be observed by eye, the presence of the non-perovskite phase is already significant. To test the condition of our samples for the early stage of decomposition we use the low-temperature micro-PL, a technique described in Section 2.2. The micro-PL scans along two pieces of MAPbI₃ sample are shown in Fig. 3.5. Although both pieces revealed no visible sign of PbI₂ precipitations, only the spectra presented in

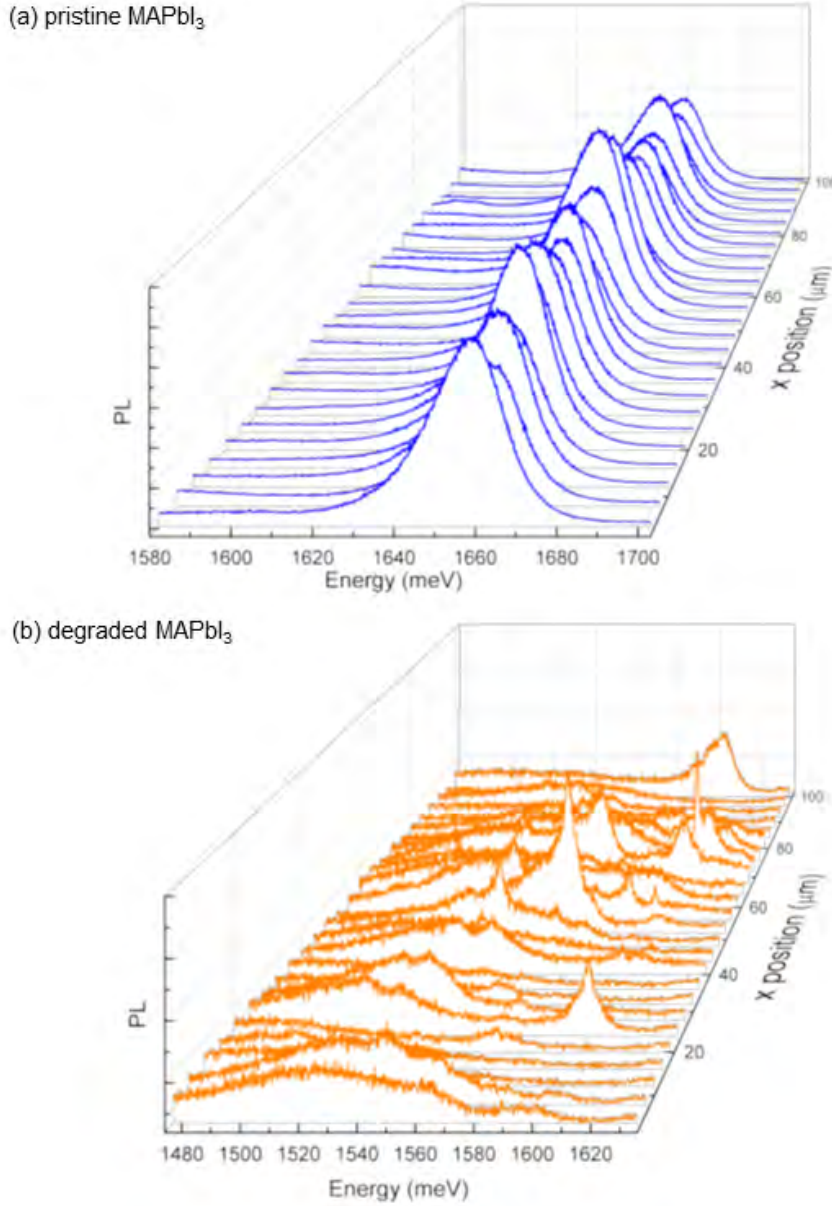


Figure 3.5: A comparison of micro-PL spectra for pristine (blue) and degraded MAPbI_3 .

Fig. 3.5 (a) correspond to the pure perovskite phase, while the results presented in panel (b) indicate the partial degradation to PbI_2 . This leads to the presence of multiple, narrow-line local emitters in the micro-PL spectrum, instead of the single Gaussian-like peak. The emission from the degraded material is several tens of

meV lower in energy than the emission from the pristine material. These lines are attributed to the local inclusions of non-perovskite phase, which preferably collect the photocreated carriers. Remarkably, such phenomenon can be observed only at low temperatures, at around 120 K and below, as this trapping becomes more efficient, when the diffusion length for the carriers decreases (see Section 5.6 for the reference). At higher temperatures, the emission occurs through the perovskite phase.

3.4 Sample characterization

For the initial characterization of the samples, we measure the energy of the near-band-gap absorption as a function of the temperature. In these studies we use the broad-band macro-transmission, performed in the absence of magnetic field with the setup described in detail in Section 2.1.2. The experimental temperature range, between 4 K and 300 K, covers the phase transition from the low temperature, orthorhombic, to the higher temperature, tetragonal phase, which was already discussed in Chapter 1. This allows an exact determination of the low-temperature phase transition point. Such a characterization is crucial prior to the high magnetic field measurements, which are performed in both orthorhombic and tetragonal phase.

MAPbI₃. First, we will refer to the measurements of the archetypal MAPbI₃ compound. The typical transmission spectra acquired at different temperatures are shown in Fig. 3.6 (a). The temperature is increased in steps of 5 K, reduced to 2 K in the phase transition region. The spectra, divided by the spectrum of the lamp, are dominated by a single strong absorption minimum. Our further magneto - transmission studies (see Chapter 4) show that this absorption corresponds to the 1s excitonic transition. We extract the absorption energies from the transmission spectra by looking for the center of the absorption shape. These energies are plotted as the function of temperature in Fig. 3.6 (b). With the increasing temperature, we observe the blue-shift and broadening of the absorption resonance. The positive temperature coefficient of the band gap is characteristic for all hybrid perovskites (which was discussed in Section 1.4.1).

Above 145 K, we find the first evidence of the phase transition developing within the MAPbI₃ film. A second minimum, which we attribute to the absorption of tetragonal phase (TP) inclusions is observed at the energy around 90 meV lower than the minimum of the orthorhombic phase (OP). As the conversion from the orthorhombic to tetragonal phase proceeds with increasing temperature, the low-energy minimum becomes more pronounced, while the absorption corresponding to the orthorhombic phase weakens. As can be seen in Fig. 3.6 (b), no significant changes in the absorption energies are observed for temperatures up to 20 K above the onset of the phase transition. At 169 K the conversion is complete, as we detect only the absorption corresponding to the tetragonal phase. Raising the temperature above 169 K, we again observe a constant increase of absorption energy and

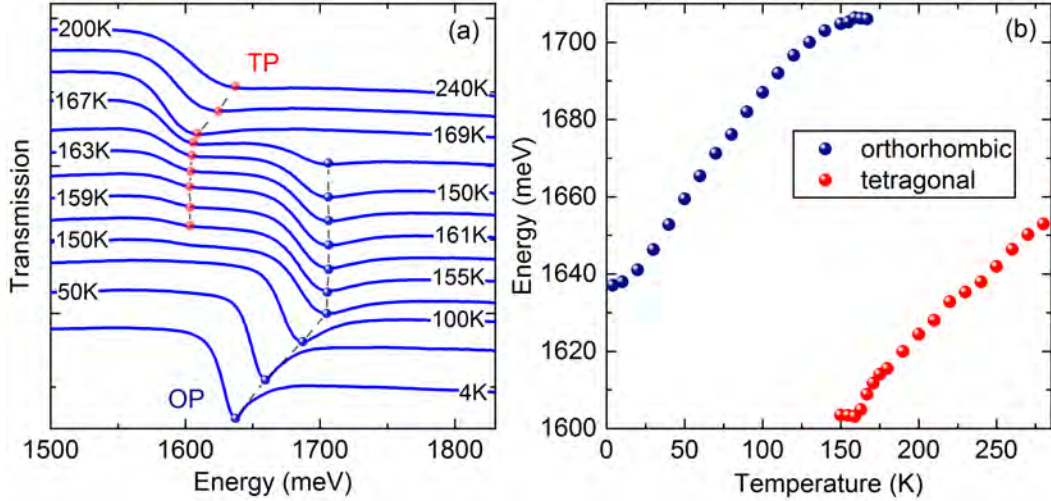


Figure 3.6: (a) Typical transmission spectra for MAPbI₃ measured at different temperatures and (b) the energies corresponding to the observed transitions plotted as the function of temperature. Points and dashed lines are added to ease the following of the transitions.

broadening of its shape.

Other organic-inorganic compounds. Similar characterization measurements were performed for all the investigated compounds. The spectra for other representatives of Methylammonium and Formamidinium families are presented Fig 3.7. As for MAPbI₃, the absorption minima blue-shift and broaden with increasing temperature. However, as the phase transition progresses, the separate absorption minimum corresponding to the tetragonal phase is not detected. Instead, we observe a continuous change of the energy of a single absorption minimum. Initially, as the material gradually converts into the tetragonal phase, this minimum moves towards lower energies. After the turning point, when the conversion is complete and the absorption energy corresponds to the tetragonal phase, a further increase of temperature again results in the increase of the transition energy.

We can compare in detail the development of the phase transition in all the investigated materials by analyzing their absorption energies plotted as a function of temperature. These are summarized in Fig. 3.8. An abrupt change in the absorption energy (evidence of the low-temperature phase transition) is observed only for MAPbI₃. The difference in the absorption energies between the orthorhombic and tetragonal phases in the MAPbCl_xI_{3-x} mixed halide, of around 70 meV, is slightly lower than the 90 meV difference observed in the pure tri-iodide. However, in the mixed halide the phase transition develops over a temperature range of \approx 50 K, and is completed at a considerably higher temperature, only above 200 K. In the Formamidinium analogue, the FAPbI₃, the conversion into the tetragonal phase also progresses slowly, over a range of \approx 30 K, and completes at the temperature of

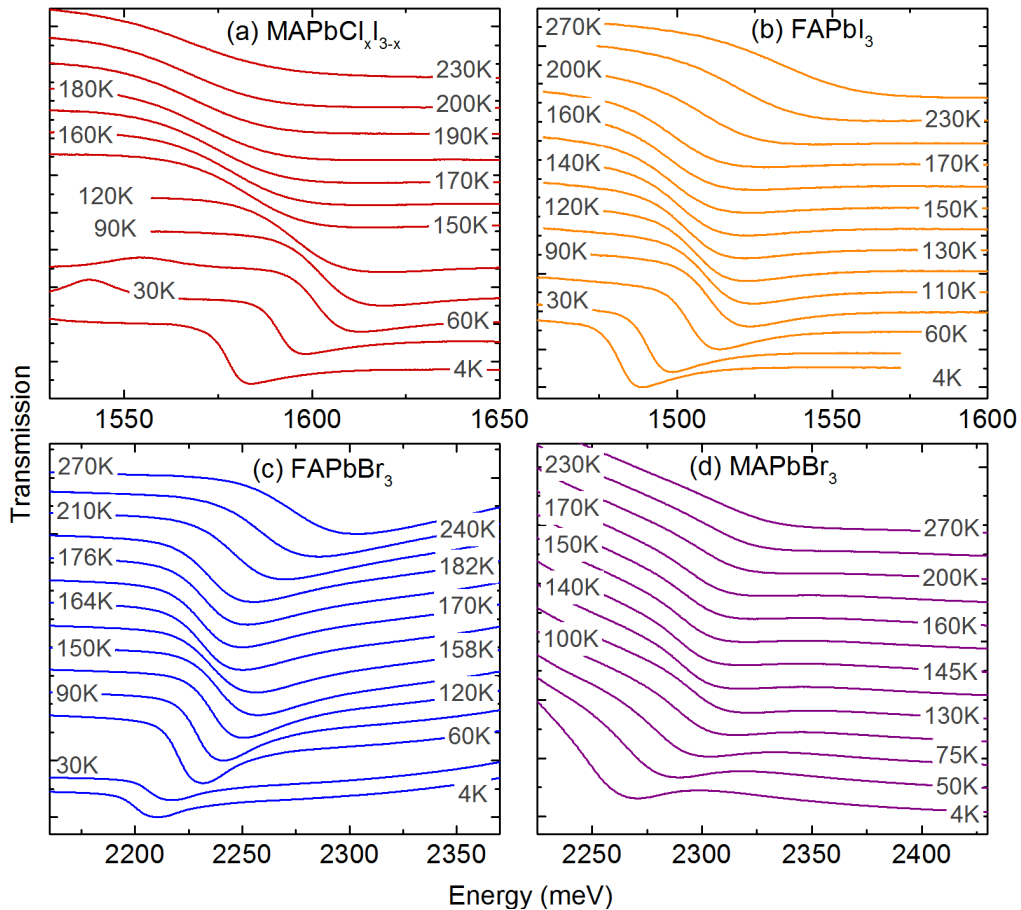


Figure 3.7: Typical transmission spectra measured at different temperatures for (a) $\text{MAPbCl}_x\text{I}_{3-x}$, (b) FAPbI_3 , (c) FAPbBr_3 and (d) MAPbBr_3 . The data for $\text{MAPbCl}_x\text{I}_{3-x}$ have been measured by Anatolie Mitioglou.

around 150 K. In comparison to other iodide based materials, the energy redshift at the phase transition point in FAPbI_3 is few times smaller, not exceeding 10 meV. A similar value for the transition-induced redshift is observed in the tri-bromides. In these high band gap materials, the phase transition develops for only around 15 K. The turning points are at 165 K for FAPbBr_3 and at 145 K for MAPbBr_3 . The phase transition from tetragonal to cubic phase, which is expected in bromides at around 240 K, does not induce any recognizable change in the transmission spectra.

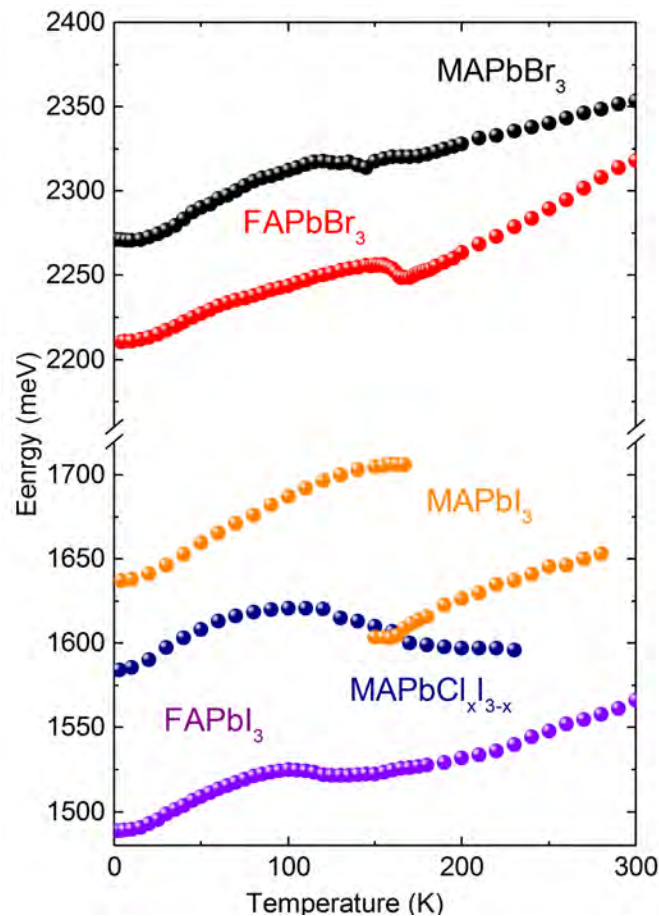


Figure 3.8: The energies of near band edge absorption as a function of temperature for all studied materials.

CHAPTER 4

Magneto transmission

Contents

4.1	Introduction	.	.	.	45
4.1.1	Electronic transitions in magnetic field	.	.	.	46
4.2	Low - temperature magneto-spectroscopy	.	.	.	51
4.2.1	Iodine-based compounds: $\text{MAPbCl}_x\text{I}_{3-x}$ and FAPbI_3	.	.	.	51
4.2.2	Tri-bromides: FAPbBr_3 and MAPbBr_3	.	.	.	53
4.2.3	Analysis	.	.	.	54
4.3	High temperature magneto-spectroscopy	.	.	.	60
4.4	Discussion	.	.	.	63
4.5	Conclusions	.	.	.	66

In this chapter, we present the results of magneto-transmission studies performed on the family of organic-inorganic perovskites, based on Methylammonium or Formamidinium organic cations. By fitting the observed excitonic and free - electron transitions with a hydrogen-like model and Landau levels, respectively, we determine the values of the exciton binding energy (R^) and reduced mass (μ). From our low-temperature studies we conclude that in all investigated materials R^* is smaller or comparable with the mean thermal energy at room temperature. Moreover, the exciton binding energy is found to decrease at high temperatures. Therefore, the photo-created carriers in the perovskite-based devices can be considered to be thermally ionized at room temperature. Finally, we show that both R^* and μ scale linearly with the band gap of the material. The results presented in this chapter have been published in *Environmental & Energy Science* **6**, 245442 (2016).*

4.1 Introduction

The basic electronic parameters in organic-inorganic perovskites, such as exciton binding energy R^* and reduced mass μ , have been the object of intense debate in the literature. The value of R^* determines the nature of photo created carriers and is therefore a matter of special interest for photovoltaics. However, either the pictures of bound or fully ionized carriers in the iodine-based perovskite compounds have been proposed basing on various indirect experimental methods. While the mean thermal energy at the room temperature is $k_B T \simeq 26$ meV, values of R^* as low as

2 meV were reported in the studies of the optical constants (n, k) [Lin 015]. In contrast, the temperature dependence of the absorption band edge has lead D’Innocenzo *et al.* to estimate a much larger value of $R^* \simeq 50$ meV [D’Innocenzo 2014]. In 2015, Miyata *et al.* using magneto-transmission measurements have demonstrated that the exciton binding energy in the archetypal perovskite photovoltaic compound MAPbI_3 is at the lower end of that range [Miyata 2015]. In magnetic field, they observed up to seven electronic transitions, originating from excitonic and free electron states, which allowed to directly determine the low-temperature, upper bound for R^* to be equal to 16 meV. This value was found to further decrease to around 10 meV in the higher temperature, tetragonal phase [Miyata 2015]. In agreement with recent theoretical calculations [Even 2014b], this result proves that at room temperature no additional energy is required to separate the photoexcited carriers. The earlier magneto-spectroscopy on MAPbI_3 , first demonstrated in 1994, revealed the evolution of only the 1s excitonic state in magnetic field [Hirasawa 1994, Tanaka 2003]. However, as it will be further shown in this chapter, only the observation of multiple excitonic transitions (in particular, both 1s and 2s) and the transitions between the Landau levels enables the direct and precise measurement of R^* and μ , which makes magneto - spectroscopy superior to other, indirect methods.

In this work, we extend the magneto - transmission studies on organic-inorganic perovskites to other, newly synthesized materials of this family. We investigate the dependence of the exciton binding energy and reduced mass on the material composition and band gap. We perform the first magneto - optical studies on the materials containing the Formamidinium organic cation and the high band gap tribromides. The band gaps for the studied materials range from 1.5 eV to 2.3 eV. For each of them, we determine the exciton binding energy and reduced mass for both the low temperature, orthorhombic phase, and the high temperature tetragonal phase. In all investigated compounds, the exciton binding energies are less or comparable to the mean thermal energy at room temperature. We also find that both the exciton binding energy and the reduced mass increase proportionally to the energy of the band gap. Moreover, the values of the reduced mass are consistent with a simple two band $\mathbf{k} \cdot \mathbf{p}$ perturbation approach for the band structure. Importantly, these conclusions can be generalized to predict the values of the reduced mass and binding energy for the other members of the family of hybrid perovskites.

4.1.1 Electronic transitions in magnetic field

This section gives a brief introduction to the influence of magnetic field on the interband optical transitions observed in bulk semiconductors. The magnetic field interacts with the orbital motion and the spin of the electron, resulting in a shift of the energy levels and a splitting of the spin states. Below, we summarize the theory of magnetic field evolution of the energy of free carrier and free exciton levels in the presence of a magnetic field. We limit our considerations to the effective mass approximation near the extrema of the parabolic, spherically symmetric bands.

Free charged particles in a magnetic field

Following the original approach of Landau [Landau 1977], the Hamiltonian of elementary electronic charge e in a magnetic field can be expressed as:

$$\hat{H} = E_g + \frac{1}{2m^*}(\hat{p} - \frac{e\hat{A}}{c})^2$$

where E_g is the band gap of the material, and \hat{A} is an electromagnetic vector potential related to the magnetic field through $\vec{B} = \nabla \times \hat{A}$. Here, \hat{p} is the momentum operator, while m^* is the effective mass of the carrier. The first term in the brackets refers to the translational kinetic energy of the particle, while the second term describes the interaction with the magnetic field. Assuming the magnetic field is applied along the z -axis, $\vec{B} = B\hat{e}_z$, we choose the Landau gauge:

$$\hat{A} = \begin{bmatrix} 0 \\ Bx \\ 0 \end{bmatrix}$$

where the non zero element is a product of the magnetic field intensity and the x component of the position operator. The resulting Hamiltonian can be written as follows:

$$\hat{H} = E_g + \frac{\hat{p}_x^2}{2m^*} + \frac{1}{2m^*}(\hat{p}_y - \frac{eB\hat{x}}{c})^2 + \frac{\hat{p}_z^2}{2m^*}$$

As this Hamiltonian does not contain the y and z coordinate components of the position operator explicitly, it commutes with \hat{p}_y and \hat{p}_z operators, which can therefore be replaced by their eigenvalues, $\hbar k_{y,z}$:

$$\hat{H} = E_g + \frac{\hat{p}_x^2}{2m^*} + \frac{1}{2m^*}(\hbar k_y - \frac{eB\hat{x}}{c})^2 + \frac{\hbar^2 k_z^2}{2m^*}$$

Introducing the cyclotron frequency, $\omega_c = \frac{eB}{m^*c}$, the Hamiltonian can be further simplified:

$$\hat{H} = E_g + \frac{1}{2m^*}\hat{p}_x^2 + \frac{1}{2}m^*\omega_c(\hat{x} - \frac{\hbar k_y}{m^*\omega_c})^2 + \frac{\hbar^2 k_z^2}{2m^*} \quad (4.1)$$

In this form, the Hamiltonian describes a harmonic oscillator in x direction and free motion along the z -axis. The shift of the harmonic potential minimum position by $x_0 = -(\frac{\hbar k_y}{m^*\omega_c})$ does not influence the energies of quantum harmonic oscillator. Thus, the energies of the free particle in the magnetic are given by:

$$E(n, k_z) = E_g + \hbar\omega_c(n + \frac{1}{2}) + \frac{\hbar^2 k_z^2}{2m^*} \quad n = 0, 1, 2, 3... \quad (4.2)$$

The kinetic energy dispersion along the z -axis leads to a density of states with Van Hove singularities rather than discrete Landau levels. We will limit our consideration to $k_z = 0$, reducing 4.2 to:

$$E_n = E_g + \hbar\omega_c(n + \frac{1}{2}) \quad n = 0, 1, 2, 3... \quad (4.3)$$

The harmonic oscillator energy term in 4.3, $\hbar\omega_c(n + \frac{1}{2})$, corresponds to the cyclotron motion in a circle in the xy -plane, about the center in $(x_0, y_0) = (-\frac{\hat{p}_y}{m^*\omega_c}, -\frac{\hat{p}_x}{m^*\omega_c})$. As Equation 4.1 does not contain the y component of momentum operator, \hat{p}_y can assume a continuous sequence of the values. Therefore, the states E_n , called Landau levels, are degenerate. This degeneracy is finite, when motion in the xy plane is limited to a finite area $A = L_x L_y$. The maximal number of electrons on each spin Landau level is then limited to the ratio of magnetic flux to the fundamental quantum of flux:

$$N = \frac{\Phi}{\Phi_0} = \frac{BA}{h/2e}$$

Each of the Landau levels is doubly degenerate with respect to spin, which will be discussed further.

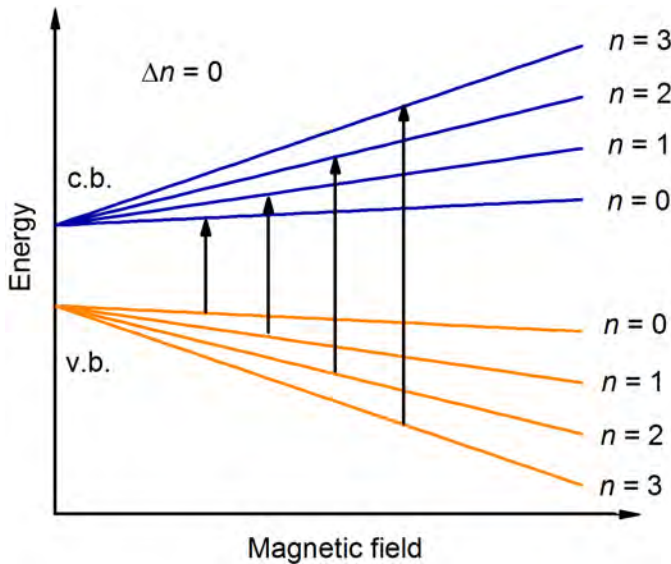


Figure 4.1: A schematic view of the Landau levels in the valence and conduction band. The interband absorptions are marked with arrows.

A schematic representation of Landau levels for $n \leq 3$ in the valence and conduction bands is shown in Fig. 4.1. The black arrows indicate the absorption interband transitions between the corresponding Landau levels, allowed by the $\Delta n = 0$ selection rule for dipole allowed transitions in hybrid perovskites. The energy of the measured free-electron absorption is the difference of the energies of the Landau levels in the valence and conduction band, characterized by the same value of n . The cyclotron frequencies for the valence and conduction band, given by $\omega_c^v = \frac{eB}{m_h^*c}$ and $\omega_c^c = \frac{eB}{m_e^*c}$, respectively, correspond to different effective masses of hole m_h^* and electron m_e^* . Using Equation 4.3, the energy of the intraband transition will be then equal to:

$$E_n = E_g + \hbar(\omega_c^c + \omega_c^v)(n + \frac{1}{2}) = E_g + \hbar\omega_c^r(n + \frac{1}{2}) \quad n = 0, 1, 2, 3, \dots \quad (4.4)$$

with $\omega_c^r = \frac{eB}{\mu c}$.

Free excitons in a magnetic field

We now turn to the influence of magnetic field on a photocreated electron-hole pair interacting via the Coulomb force, namely the exciton (see Section 1.1 for the reference). In analogy to the hydrogen atom, the energy of the n th 3D excitonic level in the absence of magnetic field scales as:

$$E_n = E_g - \frac{R^*}{n^2}. \quad (4.5)$$

where R^* is the effective Rydberg constant. Compared to the case of the free particle, the Hamiltonian for an exciton in a magnetic field contains an additional term, corresponding to the Coulomb interaction between the electron and hole:

$$\hat{H} = E_g + \frac{1}{2\mu^*}(\hat{p} - \frac{eA}{c})^2 - \frac{e^2}{\varepsilon_{eff}\|\vec{r}\|} \quad (4.6)$$

where $\vec{r} = \vec{r}_e - \vec{r}_h$ is the relative position of electron and hole. This Hamiltonian can be expressed in cylindrical coordinates (ρ, ϕ, z) , $r = \sqrt{\rho^2 + z^2}$. The $\vec{B} = B\hat{e}_z$ condition is now fulfilled by a choice of a cylindrical gauge $\hat{A} = \frac{1}{2}(\vec{B} \times \vec{r})$. Finally, we obtain:

$$\hat{H} = E_g + -\nabla^2 - \frac{2}{r} - i\gamma\frac{\partial}{\partial\phi} + \frac{1}{4}\gamma^2\rho^2 \quad (4.7)$$

where $\gamma = \frac{1}{2}\hbar\omega_c/R^*$ is a dimensionless parameter, which is the ratio of cyclotron energy and the effective Rydberg constant.

There are no exact analytical solutions for the hydrogen atom in a magnetic field, therefore its energy levels have to be derived using numerical methods. The energies of hydrogen-like states in the magnetic field, based on the variational method, were calculated by Makado and McGill in 1986 [Makado 1986]. They solved Equation 4.7 using trial wavefunctions of defined z -parity and symmetry. Their solutions are the energies of excitonic states $E_n(\gamma)$, calculated for n up to 4 and a γ range from 0 to 10. $E_n(\gamma)$ are given as the energy shifts with respect to the band gap energy E_g , in the effective Rydberg units.

For given values of μ and R^* , $\gamma(\mu, R^*, B)$ is a function of magnetic field only, $\gamma(B)$, and therefore $E_n(\gamma) \rightarrow E_n(B)$. This is presented in Fig. 4.2, where we use Makado and McGill's solutions to calculate several representative $E_n(B)$ energies relative to $E_g = 0$. The 1s, 2s and 2p excitonic state energies are calculated using $R^* = 15$ meV and $\mu = 0.1 m_e$. Each of these states is doubly degenerate with respect to the spin, and the lift of this degeneracy at high magnetic fields is indicated with the solid and dashed lines. The inset presents the model for lower values of magnetic field, where the hydrogen-like states reveal a diamagnetic behaviour. At higher fields, the excitonic states have a linear, free-carrier-like dependence.

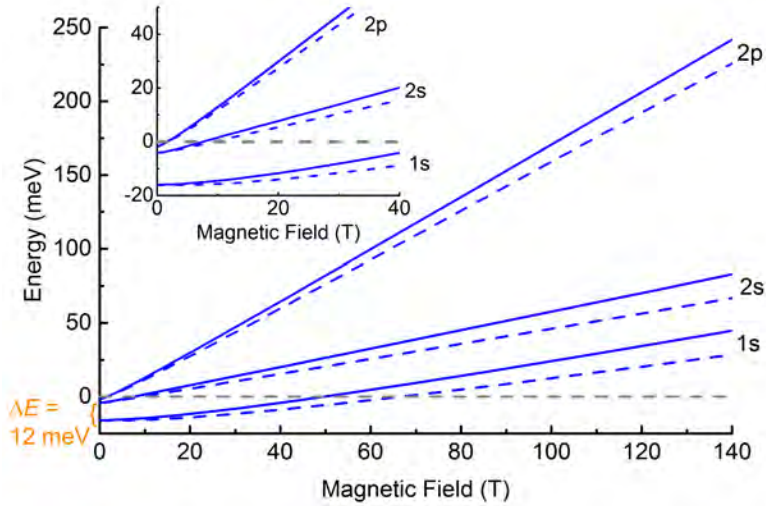


Figure 4.2: The energies of 1s, 2s and 2p hydrogen - like states calculated for $R^* = 15$ meV and $\mu = 0.1 m_e$. The solid/dashed lines correspond to spin up/spin down states, respectively. The energy level of the band gap is marked with gray dashed line. After [Makado 1986].

The Zeeman effect

Finally, we will discuss the degeneracy of the excitonic and free-electron states with respect to spin. This has not been included in the previous considerations, as due to the separation of variables, the spin Hamiltonian can be studied separately from the main/orbital Hamiltonians in Equations 4.1 and 4.6. The electronic states in both valence and conduction band are characterized by the spin quantum number $j = \frac{1}{2}$, which results in two possible values $m_j = \pm \frac{1}{2}$ of its projection on the quantization axis. Without the presence of the magnetic field, the energies of both $|\frac{1}{2}, -\frac{1}{2}\rangle$ and $|\frac{1}{2}, \frac{1}{2}\rangle$ states are degenerate, as schematically presented in Fig. 4.3. As further shown, applied magnetic field, interacting with the spin of the carriers, lifts this degeneracy. The energies of $|\frac{1}{2}, \pm \frac{1}{2}\rangle$ states shift by the value of the Zeeman energy:

$$E_Z = \pm \frac{1}{2} g_{eff} \mu_B B$$

where g_{eff} is the effective gyromagnetic factor and μ_B is the Bohr magneton. Fig. 4.3 shows the selection rules for optical interband transitions, fulfilling the requirement of momentum conservation upon photon absorption $\Delta m_j = \pm 1$. The red and blue arrows correspond to σ^+ and σ^- circularly polarized light, respectively. These states, detected at the same energy at $B = 0$ T, split in the magnetic field by $\Delta E = g_{eff} \mu_B B$.

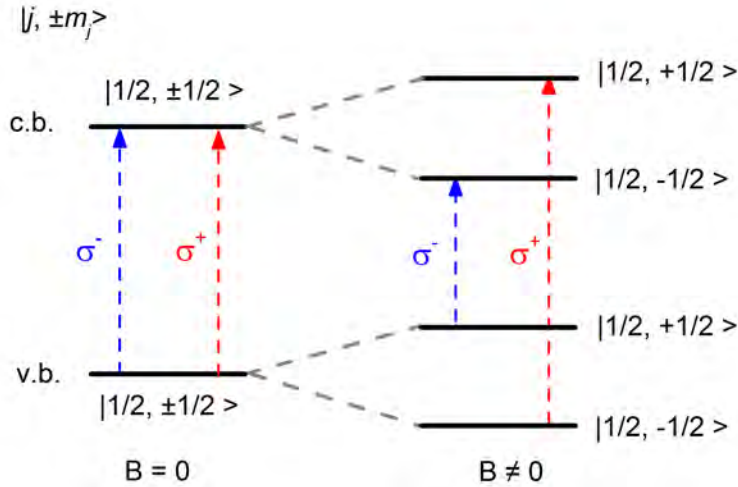


Figure 4.3: The Zeeman band splitting and the selection rules for both σ^+ and σ^- polarizations in the magnetic field .

4.2 Low - temperature magneto-spectroscopy

The low-temperature magneto - spectroscopy studies were performed at the LNCMI CNRS laboratory in Toulouse using a long magnetic pulse technique. The details of the experimental setup are given in Section 2.1. The investigated materials were iodine based $\text{MAPbCl}_x\text{I}_{3-x}$ and FAPbI_3 and high band gap tri-bromides, FAPbBr_3 and MAPbBr_3 . We measured the broadband transmission spectra using a white halogen lamp in pumped liquid helium conditions ($T \simeq 2$ K) in magnetic fields up to 70 T, observing multiple optical transitions for each compound.

4.2.1 Iodine-based compounds: $\text{MAPbCl}_x\text{I}_{3-x}$ and FAPbI_3

First, we discuss the results obtained for the iodine - based compounds, namely $\text{MAPbCl}_x\text{I}_{3-x}$ and FAPbI_3 . The measurements on $\text{MAPbCl}_x\text{I}_{3-x}$ have been performed by Anatolie Mitioglou in LNCMI. Typical magneto - transmission spectra, measured at different values of magnetic field, are presented in Fig. 4.4 (a) and (c). This experiment was performed using polarization optics, and the blue and red curves correspond to σ^- and σ^+ circular polarizations, respectively. The points and dashed lines are added as a guide to the eye to follow the evolution of the absorption energies in magnetic field. The spectra in panel (a) and (c) show a well developed minimum at around 1.58 eV and 1.49 eV, respectively. As it will be later demonstrated, these absorptions correspond to the 1s state of the neutral exciton. In the case of $\text{MAPbCl}_x\text{I}_{3-x}$, a second, weaker minimum develops in fields above 20 T, around 1.6 eV, as can be seen in Fig. 4.4 (a). This transition will later be attributed to the 2s state. Both 1s and 2s absorptions reveal a clear Zeeman splitting.

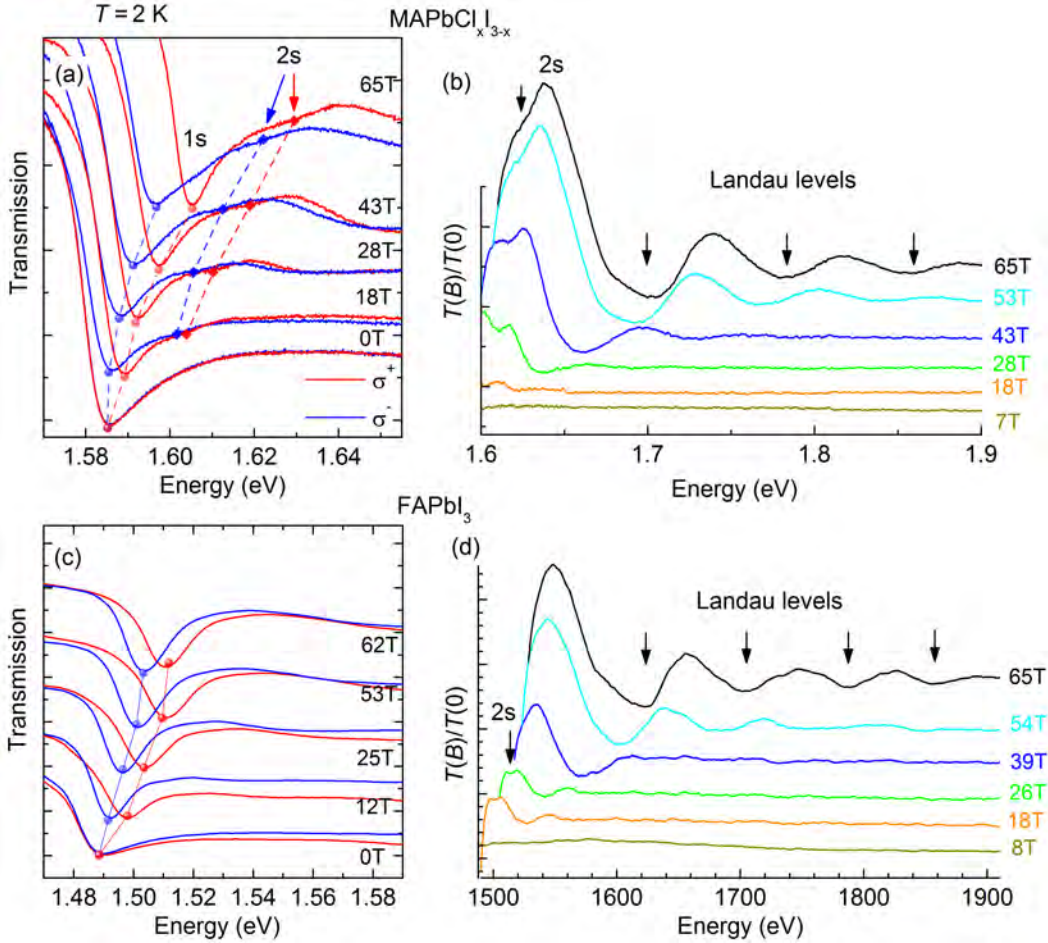


Figure 4.4: (a),(c): typical low temperature transmission data for $\text{MAPbCl}_x\text{I}_{3-x}$ and FAPbI_3 obtained using a long pulse technique. Red and blue lines correspond to two σ^+ and σ^- polarized light respectively. The blue/red points and dashed lines are added to ease the following of the 1s and 2s transitions. (b),(d): The spectra at different magnetic fields divided by the spectrum acquired at 0 T.

We extend the measurements into the visible light spectral range, where for the analysis we plot the spectra in the magnetic field divided by the spectrum taken at zero field, as shown in Fig. 4.4 (b) and (d). As the spin splitting is not well resolved over such a large energy scale due to a limited spectral range of the used polarization optics, these data are not polarization resolved. The first, low-energy spectral feature visible in panels (b) - (d) is a result of dividing the signal over the region of the magnetically shifted 1s state. Within this differential feature, we observe the minima corresponding to the 2s state. Remarkably, in FAPbI_3 this transition is resolved only in the divided spectra, for the region of the intermediate magnetic fields between 20 T to 45 T. For both of the compounds, we detect a sequence of additional minima of considerably weaker absorption, which are marked

with the arrows. These minima become more pronounced with the increase of the magnetic field and their energy encounter larger field-induced blue-shift than the low-energy transitions. This suggests a free electron origin of these absorptions.

4.2.2 Tri-bromides: FAPbBr₃ and MAPbBr₃

Complementary low-temperature studies on the representatives of the higher band gap (2.2-2.3 eV) organic-inorganic perovskites, have been performed on the tri-bromides, namely FAPbBr₃ and MAPbBr₃. For this energy range, we measure without resolving the circular polarization. The magneto-transmission spectra for these compounds, measured at different values of magnetic field are presented in Fig. 4.5, where panels (b) and (d) show the spectra divided by the zero - field spectra. As shown in Fig. 4.5 (a) and (c), the transmission spectra of tri-bromides are also dominated by one strong minimum, which we attribute to the 1s excitonic state. Compared to MAPbCl_xI_{3-x} and FAPbI₃, this resonance is approximately three times broader, and centered at around 2205 meV for FAPbBr₃ and 2270 meV for MAPbBr₃. Also, in the case of FAPbBr₃, we detect another absorption for magnetic fields above 20 T (marked in red in Fig. 4.5 (a)), analogous to the results for MAPbCl_xI_{3-x}. The energy of this minimum is approximately 2230 meV. However, this transition, originating from the 2s excitonic state, is not observed in MAPbBr₃, even in the differential spectra. In both FAPbBr₃ and MAPbBr₃ a further minimum corresponding to the $n = 1$ Landau level or higher excitonic transition appears at higher magnetic fields, separated from the 1s state by around 70 meV at 50 T. Unfortunately, this is the highest transition observed for the high band gap compounds. Unlike in the tri-iodides, where up to seven absorption minima are revealed in the long pulse experiment, in tri-bromides not more than three are observed.

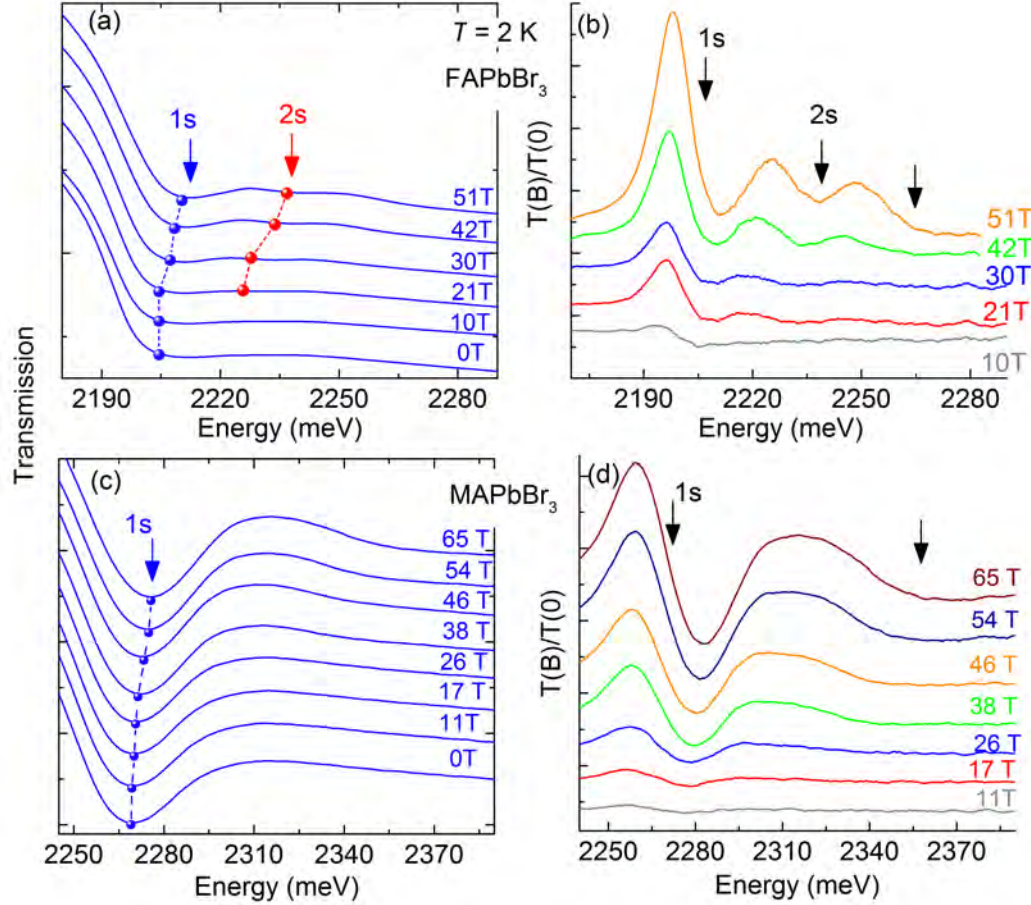


Figure 4.5: (a),(c): typical low temperature transmission data taken using a long pulse technique for FAPbBr₃ and MAPbBr₃. The blue/red points and dashed lines are added to ease the following of 1s and 2s transitions, respectively. (b),(d): The spectra at the magnetic field divided by the spectrum acquired at 0 T.

4.2.3 Analysis

To extract the binding energy and the reduced mass of the exciton from the magneto-transmission data, we fit the observed transitions with the theoretical hydrogen-like and free electron models presented in Section 4.1.1. The procedure of the analysis will be presented in detail for the example of MAPbCl_xI_{3-x}.

The transmission spectra for each value of the magnetic field are analyzed to find the energies of the particular absorption minima. We perform this by looking for the center of the absorption shape, assuming a Gaussian-like symmetry. All data points obtained for MAPbCl_xI_{3-x} - the absorption energies for both σ^- and σ^+ circular polarizations, plotted as a function of the magnetic field, are presented in Fig. 4.6 (a). An observation of the alignment of the data points allows us to discriminate between the particular transitions. Already at this stage, the significant

differences in magnetic field behaviour can be recognized. The high - energy transitions shift linearly with the increasing intensity of the magnetic field. Furthermore, the slope and separation are found to increase between the consecutive transitions. This strongly suggests the free - carrier nature of these states. In contrast, the low energy transitions, close to the band edge, reveal remarkably weaker magnetic - field dependence. Its initially diamagnetic character, with an enhancement of the magnetic-field dependence for fields above 40 T, corresponds to the hydrogen - like behaviour, typical of free excitons.

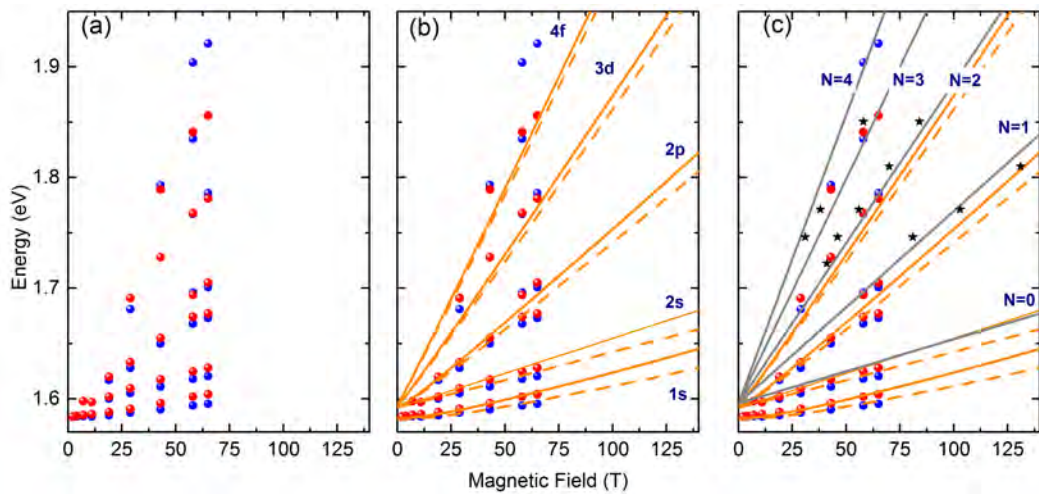


Figure 4.6: (a) The typical data points from the long pulse (red and blue spheres for σ^+ and σ^- circular polarizations, respectively) (b) the long pulse data with a simulation of hydrogen like model (orange curves) for 1s, 2s, 2p, 3d and 4f states. The Zeeman split transitions are shown by the solid and dashed lines. (c) The plot from panel (b) supplemented with Mega Gauss data (black stars) and Landau level simulations (gray lines). The value of μ is the same for free electron and hydrogen-like model.

Thus, as the first step, we use Makado and McGill's solutions to hydrogen-like Hamiltonian from Equation 4.7 to fit the data. By manipulating the values of the exciton reduced mass μ and the exciton binding energy R^* , we match the energies of the excitonic states $E_n(\gamma)$ with the data points. Simultaneously, we set the value of the band gap E_g to adjust the curve describing the 1s state with the corresponding absorption at the zero field. In the case of polarization resolved studies, we also add the Zeeman energy term (Equation 4.3), with g_{eff} being determined by fitting the Zeeman splitting in magnetic field, which is described in details at the end of this section.

The results of a typical fit of the excitonic states up to $n = 4$ to the experimental data points for $\text{MAPbCl}_x\text{I}_{3-x}$ are plotted in Fig. 4.6 (b) with the orange lines. The dashed and solid lines correspond to σ^- and σ^+ circular polarizations, respectively.

It is important to note that only the hydrogen-like states with $n \leq 3$ describe well the data, while no reliable match is possible with the same parameters for the high energy absorptions, observed at high magnetic fields. To fit this data range, we use the Equation 4.4 for the energies of the intrerband transitions between the Landau levels. Here, we support the analysis with the data from extended magnetic field range of 70-150 T, which is relevant for the free-carrier transitions. These results were obtained by Atsuhiko Miyata in the ultrashort pulse, extreme magnetic field Mega Gauss experiment, performed at LNCMI. These studies are based on monochrome light transmission, performed without the polarization optics. As a result, we neglect the Zeeman energy term in our modelling of the free electron states.

The full fan chart for $\text{MAPbCl}_x\text{I}_{3-x}$, now supplemented with the model of transitions between the Landau levels (gray lines) and Mega Gauss data (black stars) is shown in Fig. 4.6 (c). The free - electron calculations are performed for the same value of μ as used for the excitonic states, providing a good description for the high energy transitions. Thus, by the simultaneous application of both hydrogen-like and free electron models with agreed value for the reduced mass, it is possible to model the magneto-transmission data over the full energy range. Similarly to $\text{MAPbCl}_x\text{I}_{3-x}$, in other compounds we observe usually three: 1s, 2s and 2p excitonic transitions, and Landau levels up to $n = 4$.

As the reduced mass is the only fitting parameter for the Landau levels, the high energy, high magnetic field transitions provide a strong constraint for the determination of μ . Introducing the accurate value of μ , obtained from the modeling of the free electron states, into the hydrogen -like model, it is possible to refine the adjustment of R^* . However, to precisely determine the exciton binding energy, the simultaneous observation of the 1s and 2s transitions is paramount. Both of these states originate from the same Landau level, at same time being spectrally well resolved from free electron transitions. According to Equation 4.5, the energies corresponding to 1s and 2s absorption are separated by $E_{2s} - E_{1s} = \frac{3}{4}R^*$. Therefore, adjusting the value of R^* to reproduce the experimentally observed 1s-2s splitting, we obtain a direct evaluation of the exciton binding energy.

We have performed similar modelling for all the compounds studied at low temperatures, namely $\text{MAPbCl}_x\text{I}_{3-x}$, FAPbI_3 , FAPbBr_3 and MAPbBr_3 . The corresponding fan charts, consisting of experimental data, and the simulations for both the excitonic transitions (orange curves) and the Landau states (gray lines) are shown in Fig. 4.7; panels (a),(b),(c) and (d) for $\text{MAPbCl}_x\text{I}_{3-x}$, FAPbI_3 , FAPbBr_3 and MAPbBr_3 , respectively. The resulting parameters: E_g , R^* , μ and g_{eff} are collected in Table 4.1. The values for effective dielectric constant, ε_{eff} , have been calculated from Equation 1.6. We estimate the errors by comparison of accuracy of the fits performed with different parameters. To extend our analysis, we add the earlier results for the archetypal MAPbI_3 compound, obtained with the same experimental and analysis methods [Miyata 2015].

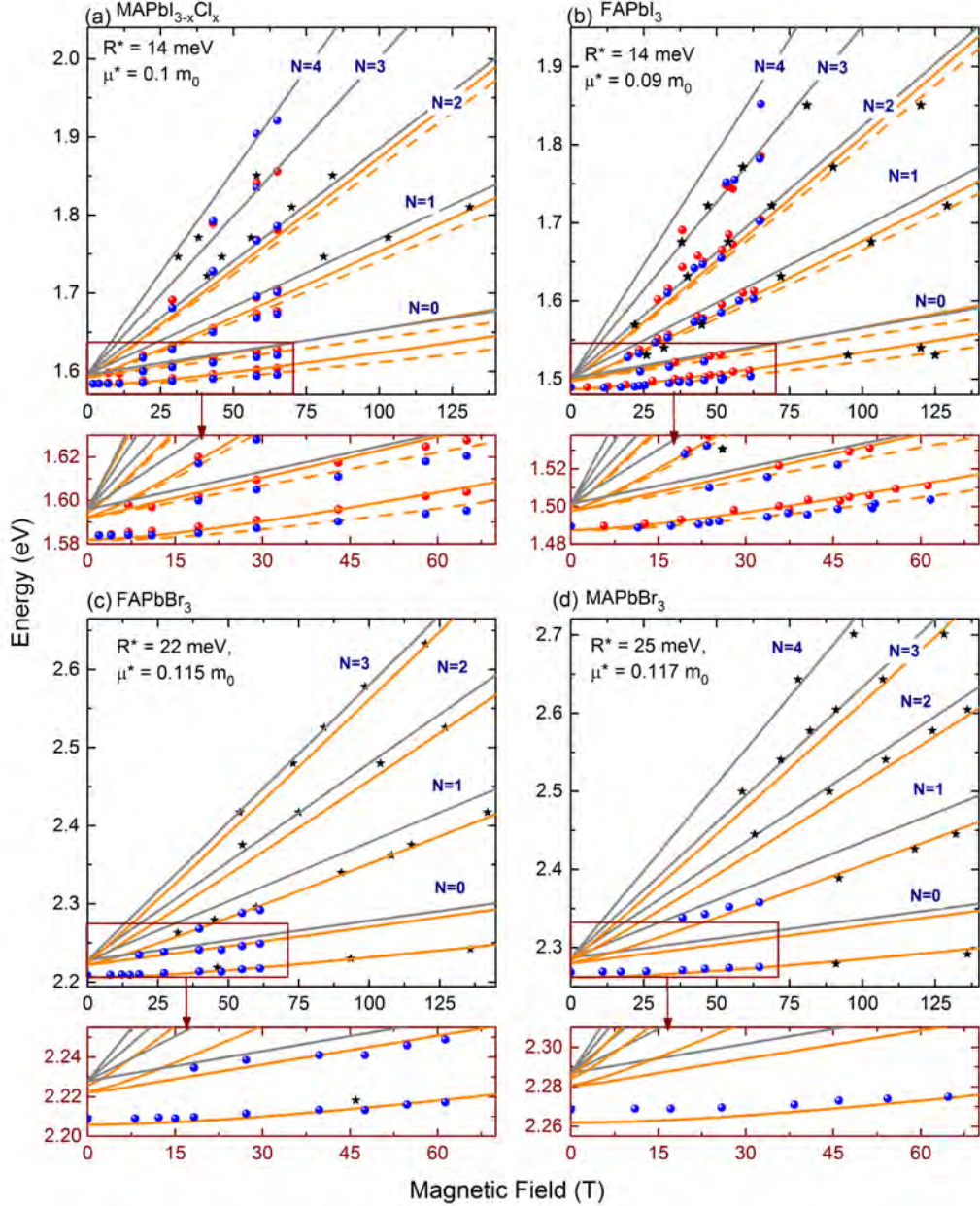


Figure 4.7: (a)-(d) Transition energies obtained from the experimental data and results of the fit to the data for MAPbCl_{3-x}I_x, FAPbI₃, FAPbBr₃ and MAPbBr₃ respectively. The red and blue points correspond to the polarization resolved minima in the absorption for σ^+ and σ^- respectively. The stars are the data obtained during the short pulsed measurements, where polarization was not used. The long pulsed data are also not polarization resolved for the FAPbBr₃ and MAPbBr₃ samples. The results of the theoretical fit are shown by grey and orange lines. Grey lines correspond to the interband transitions between Landau levels in the valence and conduction bands. The orange lines show the strongly bound levels of the hydrogen-like exciton. In (a) and (b) the Zeeman split transitions are shown by the solid and dashed lines. Below each graph the low field and low energy part of the full fan chart diagram is enlarged.

2K, orthorhombic phase

Compound	E_g (meV)	R^* (meV)	μ (m_e)	ε_{eff}	g_{eff}
FAPbI ₃	1501	14 ± 1	0.09 ± 0.01	9.35	2.3
MAPbI _{3-x} Cl _x	1596	14 ± 1	0.10 ± 0.01	9.85	2.3
MAPbI ₃	1652	16 ± 1	0.104 ± 0.01	9.4	
FAPbBr ₃	2233	22 ± 2	0.115 ± 0.01	8.42	
MAPbBr ₃ *	2292	25 ± 5	0.117 ± 0.01	7.5	

Table 4.1: The parameters of the fit full Landau fan chart for four different compounds in the low temperature, orthorhombic phase. *The data for the MAPbBr₃ do not show a detectable 2s state and therefore have a significant error of around ±20% for R^* .

Both R^* and μ are found to depend on the band gap, increasing as the gap increases. The differences are particularly small between the iodides. Although the band gap of FAPbI₃ (1501 meV) is almost 100 meV smaller than for the mixed halide, the fitting results for both materials are very similar, giving the same value of $R^* = 14$ meV. A slight distinction is observed in the reduced masses, which are $0.09 m_0$ and $0.10 m_0$ for FAPbI₃ and MAPbCl_xI_{3-x}, respectively.

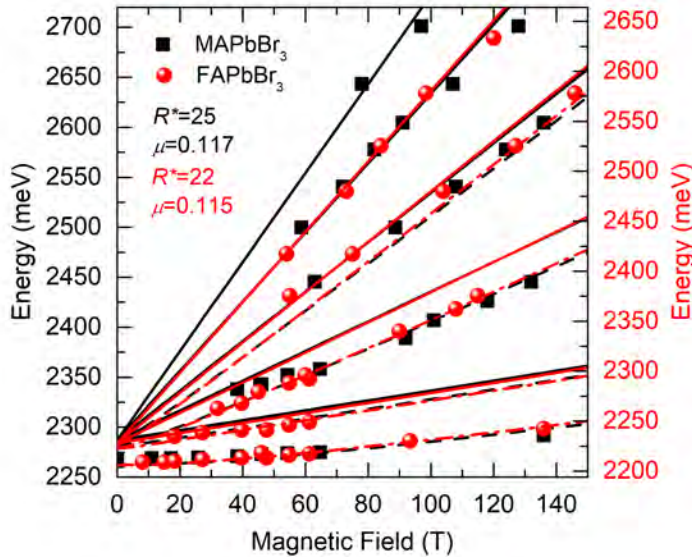


Figure 4.8: The low temperature data and corresponding fits for FAPbBr₃ (red) and MAPbBr₃ (black). The equal energy scales are the same for both compounds, shifted to match the band gaps.

In FAPbBr₃, for the band gap of 2233 meV, the increase of R^* to 22 meV is followed by the increase of μ to $0.115 m_0$. For MAPbBr₃, no observation of

the 2s transition and limited reliability of the low-field 2p state data results in higher uncertainties of the derived parameters. For this compound, characterized by the highest band gap $E_g = 2392$ meV, we estimate R^* to be of the order of (25 ± 5) meV and $\mu = (0.117 \pm 10\%) m_0$. The uncertainty of R^* is limited due to the accurate determination of the value of μ obtained by fitting the high field free electron transitions (see Fig. 4.7 (d)). To further confirm the reliability of the results obtained for MAPbBr₃, in Fig. 4.8 we compare the data and fits for MAPbBr₃ and FAPbBr₃. Both plots have the same scale, shifted to match the band gap. We observe a similarity in the curve profiles and slopes, thus we conclude that the exciton binding energy and reduced mass are indeed comparable in the tri-bromides.

To find the exact values of the gyromagnetic factor, we investigate the difference of energies for σ^+ and σ^- transitions, $\Delta E = E^{\sigma^+} - E^{\sigma^-}$. These are plotted as the function of the magnetic field in Fig. 4.9, for the 1s states of MAPbCl_xI_{3-x} and FAPbI₃, in panels (a) and (b) respectively. The errors of ΔE are determined to be equal to 0.5 meV for MAPbCl_xI_{3-x} and 0.8 meV for FAPbI₃. We fit the data points with the Zeeman splitting term:

$$\Delta E = g_{eff}\mu_B B$$

The fits are plotted in Fig. 4.9 with the red lines. We obtained $g_{eff} = 2.34 \pm 0.06$ and $g_{eff} = 2.30 \pm 0.10$ for MAPbCl_xI_{3-x} and FAPbI₃, respectively. Such values for g_{eff} are slightly larger than reported previously [Tanaka 2003]. The data is well reproduced by a linear spin splitting and therefore shows no evidence for a Rashba splitting which has been suggested for some crystal structures in the high temperature phase [Kim 2014, Even 2015].

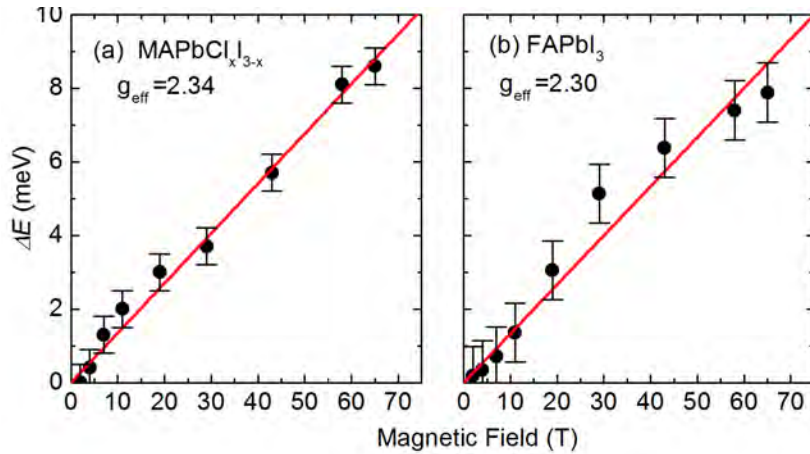


Figure 4.9: The differences in energies of σ^+ and σ^- transitions, $\Delta E = E^{\sigma^+} - E^{\sigma^-}$, plotted as a function of magnetic field for MAPbCl_xI_{3-x} and FAPbI₃ in panels (a) and (b), respectively. The linear fits are presented with the red lines.

4.3 High temperature magneto-spectroscopy

We extended the magneto - transmission measurements towards higher temperatures, more relevant to the operational conditions of a photovoltaic device. The temperature evolution of absorption spectra was discussed in details in Section 3.4. We performed the experiment just above the phase transition point, around 150-160 K, where the hybrid perovskites transform from the low temperature, orthorhombic, to the high temperature, tetragonal phase. In this way, we investigate the material of lattice parameters very similar to the parameters revealed at room temperature, while at $T \simeq 150$ K we have the considerable advantage that the absorption minima are remarkably stronger and better defined when compared to $T \simeq 300$ K (see Fig. 3.6, Fig. 3.7). At the same time, the mean thermal energy twice smaller than at the room temperature reduces the magnetic field threshold for the observation of Landau levels.

For the measurements in the tetragonal phase, we used $\text{MAPbI}_{3-x}\text{Cl}_x$, FAPbI_3 and FAPbBr_3 , the compounds for which we have determined R^* for the orthorhombic phase without significant uncertainties. Both experimental and data analysis procedures were the same as for the low temperature studies, described in Section 4.2.3.

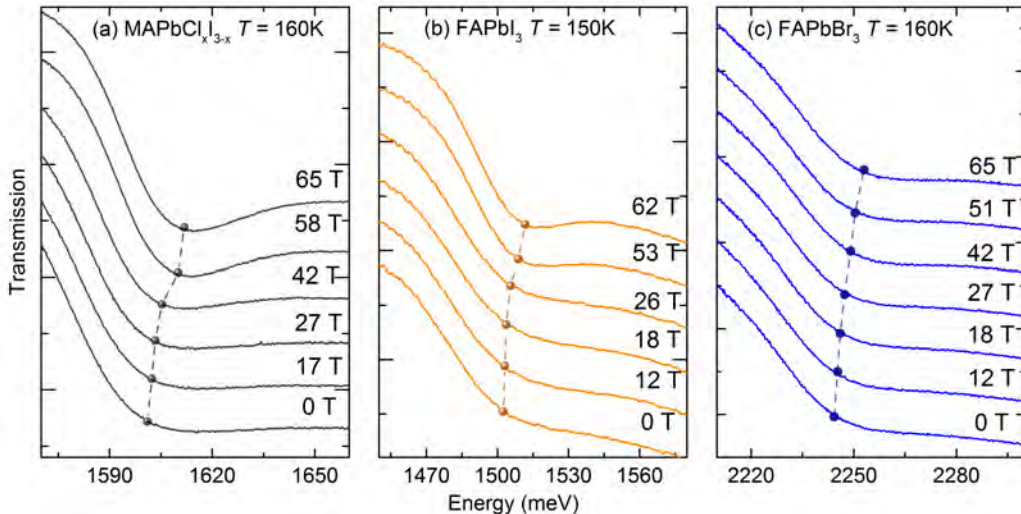


Figure 4.10: The typical absorption spectra for (a) $\text{MAPbI}_{3-x}\text{Cl}_x$, (b) FAPbI_3 and (c) FAPbBr_3 , measured at several values of magnetic field for the high temperature, tetragonal phase. Points and dashed lines are added to ease the following of the 1s transitions.

The typical absorption spectra at different values of magnetic field for $\text{MAPbI}_{3-x}\text{Cl}_x$, FAPbI_3 and FAPbBr_3 are shown in the Fig. (a),(b) and (c), respectively. For each material, the temperature of the experiment is given in the corresponding panel. Compared to $T \simeq 2$ K, the absorption minima at $T \simeq 160$ K are sig-

nificantly broader (on average by a factor of three). Therefore, in the long pulse measurements we detect only the 1s transition. The weaker transitions at higher energies are not resolved due to thermal broadening. Moreover, the direct observation of higher excitonic states is further disturbed by the expected increase of ε_{eff} [Even 2014b, Miyata 2015], resulting in a reduced spectral separation of these states.

Similarly as in the case of low-temperature measurements, we add to our long-pulse results the data obtained in the extreme magnetic field Mega Gauss experiment, performed by A. Miyata. We plot all data points obtained with long and short pulse techniques on fan charts in Fig. 4.11. In the analogy to Fig. 4.10, panels (a),(b) and (c) correspond to $\text{MAPbI}_{3-x}\text{Cl}_x$, FAPbI_3 and FAPbBr_3 , respectively. Following the procedure for the low temperature studies, we simulate the hydrogen-like and free electron transitions to extract the values of the exciton binding energy R^* and reduced mass μ . The results are drawn in Fig. 4.11, in orange for the excitonic states and in gray for Landau levels. The fitting parameters are summarized in Table 4.2.

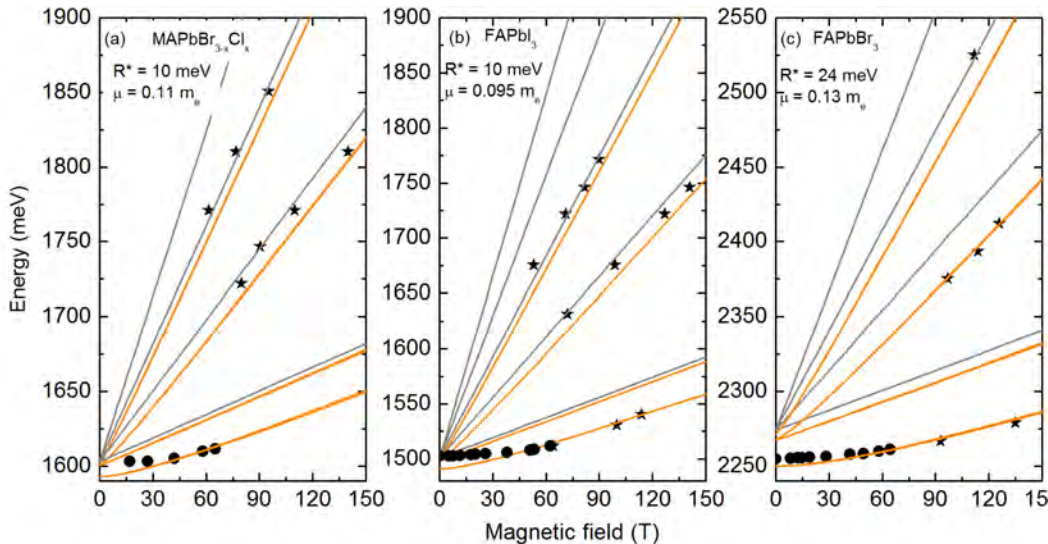


Figure 4.11: (a)-(c) Transition energies obtained from the experimental data and results of the fit to the data for $\text{MAPbCl}_x\text{I}_{3-x}$, FAPbI_3 and FAPbBr_3 , respectively. The stars are the data obtained during the short pulsed measurements. The results of the theoretical fit are shown by grey and orange lines. Grey lines correspond to the interband transitions between Landau levels in the valence and conduction bands. The orange lines represent the energy levels of the hydrogen-like exciton.

In the tetragonal phase, the interband transitions between the Landau levels are observed only in the Mega Gauss experiment, even in the case of $\text{MAPbI}_{3-x}\text{Cl}_x$ and FAPbI_3 , where at $T \simeq 2 \text{ K}$ such transitions were detected in the long pulse even

below 40 T. Although the number of data points is reduced, we are able to obtain a good linear fits for the high energy transitions. Therefore, we conclude that the values of μ increased slightly to $(0.095 - 0.13 \pm 0.01) m_0$. The biggest increase is observed for the tri-bromide, which is in the agreement with the increase in the band gap with respect to the low temperature value. This difference is around 60 meV for FAPbBr₃, and considerably lower (20 meV) for FAPbI₃, while the band gap remains almost unchanged for the mixed halide.

High temperature tetragonal phase

Compound	E_g (meV)	R^* (meV)	μ (m_e)	ε_{eff}	Temperature (K)
FAPbI ₃	1521	10 ± 2	0.095 ± 0.01	11.4	140-160
MAPbI _{3-x} Cl _x	1600	10 ± 2	0.105 ± 0.01	11.9	190-200
MAPbI ₃	1608	12 ± 4	0.104 ± 0.01	10.9	155-190
FAPbBr ₃	2294	24 ± 6	0.13 ± 0.01	8.6	160-170

Table 4.2: The parameters of the fit of the full Landau fan chart for four different compounds in the higher temperature, tetragonal phase.

The estimations for R^* have larger errors, as we see no trace of absorption corresponding to the 2s state in the intermediate field range of 10-65 T, where it is usually observed. In the iodides, the exciton binding energies are found to be reduced at the tetragonal phase to $R^* = 10 \pm 3$ meV, with a corresponding increase in ε_{eff} . By contrast, in the FAPbBr₃ we estimate $R^* = 24 \pm 4$ meV, which is a slightly higher value than measured for the low temperature, orthorhombic phase. However, it is important to note that fitting of the low field data for the 1s state with parameters corresponding to the high - field points is problematic. Below 50 T, the values of the experimental points for this transition in the iodides are up to 12 meV larger than the results of fit for hydrogen-like model, which is most visible in the absence of magnetic field. We attribute this differences to the low accuracy in the determination of the 1s absorption energy to thermal broadening of absorption shape. In the temperature range of phase transitions, the mean thermal energy is larger or comparable to exciton binding energies in the iodides, thus the band-edge absorption includes also higher and ionized states, and no single transition is resolved 4.10. A more discrete 1s minimum is observed only in higher magnetic fields, due to the increased separation between the states and enhanced oscillator strengths. In agreement with this picture, the differences between the values of low-field data and the model are less pronounced in the bromide. In this material, the exciton binding energy, thus, the separation between the states is around two times larger, and the shape of the absorption minimum does not change significantly in the magnetic field. Therefore, in our analysis we mainly focus on the high-field data. However, such observations may also indicate that the phonon contribution to the dielectric screening is reduced in the magnetic field, as it has been discussed previously [Miyata 2015]. Thus, the values obtained for R^* in magneto-optical studies will be an overestimate of the

zero-field values.

4.4 Discussion

In this section, we will perform a detailed analysis of the low- and high-temperature magneto-spectroscopy results, included in Table 4.1 and Table 4.2, respectively. The crucial electronic parameters - the reduced mass μ and exciton binding energy R^* measured at the low temperature, orthorhombic phase, are plotted as a function of the bandgap of the material in the Fig. 4.12 (a). Both parameters are found to weakly increase with the band gap.

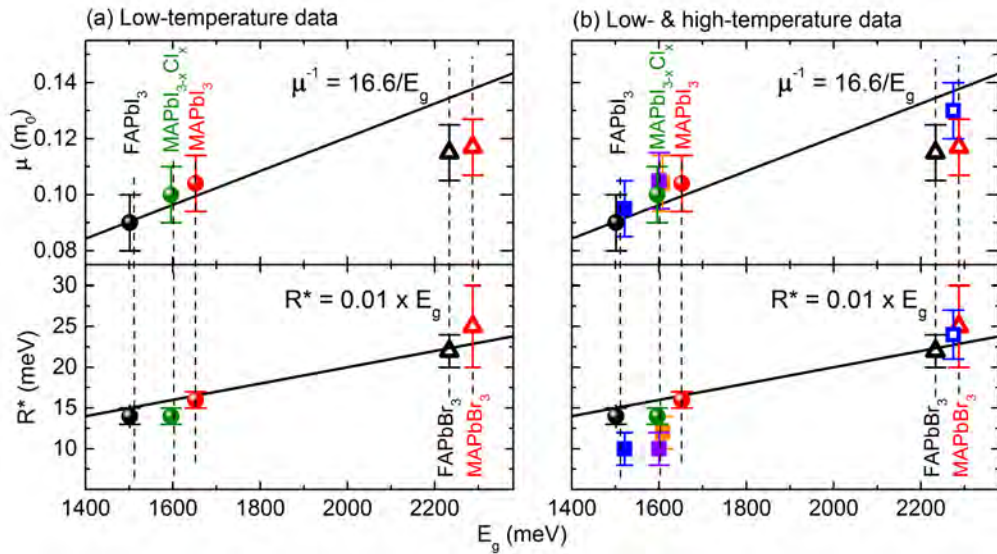


Figure 4.12: (a) and (b) Reduced mass and binding energy at $T = 2$ K as a function of the energy gap respectively. Black (red) symbols mark results for FA (MA) iodides (full symbols) and bromides (open symbols). Green circles show results for the mixed halide $\text{MAPbI}_{3-x}\text{Cl}_x$. The black solid lines show a linear fit to the data. (c) and (d) The low temperature data plot together with the values deduced for the higher temperature tetragonal phase (with squares) for the FA (blue), MA (orange) and mixed halide (purple) materials, measured in the temperature ranges given in Table 4.2

The values of reduced excitonic mass in studied materials are between 0.090 to 0.117 of mass of the free electron. In particular, for iodine dominated compounds, this range is limited to 0.095 - 0.105 m_0 , which is in a good agreement ($\mu = 0.09 - 0.1m_0$) with the recent density functional theorem (DFT) calculations, adjusted to fit the experimental value of the band gap for MAPbI_3 [Menéndez-Proupin 2014, Umari 2014]. As the organo-lead halide perovskites are characterized by relatively simple band structure, a simple semi-empirical two band $\mathbf{k} \cdot \mathbf{p}$ Hamiltonian approach

can be applied for the effective mass calculations [Even 2015]. The non - degenerate band edges are nearly isotropic, and the effective masses in the conduction and valence bands are similar. The effective masses for the electron and hole would be then given by:

$$\frac{1}{m_{e,h}^*} = \frac{1}{m_0} \left| \left(1 \pm \frac{2|P|^2}{m_0 E_g} \right) \right|$$

where $\frac{2|P|^2}{m_0 E_g}$ is the Kane energy, determining the strength of the optical transitions [Chuang 1995], with

$$P = \langle \psi_{VB} | i\hbar \frac{\partial}{\partial x} | \psi_{CB} \rangle$$

being the momentum matrix element arising from $\mathbf{k} \cdot \mathbf{p}$ term, coupling electron wavefunctions in the conduction and valence bands. Resulting from the properties of the band structure, this element is also considered to be isotropic [Zhou 2014, Umari 2014, Even 2012]. Following Equation 1.4, the reduced mass μ will be:

$$\frac{1}{\mu} = \left| \frac{1}{m_e^*} \right| + \left| \frac{1}{m_h^*} \right| = \frac{4|P|^2}{m_0^2 E_g}. \quad (4.8)$$

The direct DFT calculations predict the Kane energy for hybrid perovskites to be in the order of 5.3-6.3 meV [Even 2014b, Fang 2015], although more recent works, including the spin-orbit coupling, suggest higher values [Menéndez-Proupin 2014, Umari 2014]. A fit of Equation 4.8 to the low temperature data, presented in the upper panel of Fig. 4.12 (a), yields the value of the Kane energy equal to 8.3 meV. Taking into account the rise of μ values of around 10%, the estimation for the Kane energy at room temperature is around 7.5 meV.

Remarkably, there is no strong evidence for a change in the reduced mass when substituting Methylammonium with Formamidinium cations. We observe only small changes in the band gap, induced by the changes in the lattice parameters, like the octahedra tilting suggested by Amat et al. [Amat 2014].

The effective Rydberg constant turns out to be more material dependent, varying with the band gap from 14 to 25 meV approximately as:

$$R^* = 0.01 \times E_g$$

These values are around 3 times smaller than previously reported for magneto-optical measurements, where only the 1s state was observed [Tanaka 2003]. However, these values are in a good agreement with the value of 15 meV, deduced by Even et al. [Even 2014b] by fitting the highly resolved zero field absorption spectrum. The difference can then be explained by the observation of the 1s transition only, which does not permit a direct determination of R^* . Moreover, the temperature dependent reduction of R^* , which will be further discussed, indicates that the values measured at $T = 2$ K are the upper limit for the exciton binding energies in these materials. Therefore, being less than or comparable to the thermal energy at room temperature ($\simeq 25$ meV), our low temperature results for R^* suggest that

in the entire family of the hybrid tri-halide perovskites the photocreated carriers are expected to be thermally ionized at 300 K. This goes a long way to explain the excellent efficiencies of perovskite photovoltaic devices.

The values of effective dielectric constant ε_{eff} from Table 4.1 have been derived with a conventional formula for the effective Rydberg (Equation 1.6). The ε_{eff} , which takes into account the Coulomb potential screening by the lattice, is found to be in the range of 7.5 - 9.8. between the low $\varepsilon_0 = 25.7$ [Wehrenfennig 2014a] and high $\varepsilon_\infty = 5.6$ frequency values [Umari 2014, Brivio 2014]. A slight decrease of ε_{eff} is observed with the rise of R^* and μ , resulting from the reduction in size of the exciton Bohr radius and changes in the lattice parameters induced by varying halide content. Such behaviour is characteristic for highly polar materials with strong electron - phonon coupling, which was first demonstrated by Pollman and Buttner [Pollman 1975] and by Kane [Kane 1978] for II-VI and I-VII materials. Giving an example of TlCl, a I-VII compound with comparable parameters ($\varepsilon_0 = 37.6$, $\varepsilon_\infty = 5.4$, $\mu = 0.18 m_0$) it was found that $\varepsilon_{eff} = 2.48\varepsilon_\infty$. Although in perovskites the simulations of the dielectric constant are more complicated due to the presence of the multiple polar phonon modes, such rotational motion of the Methylammonium cations, the recent results suggest again the values of ε_{eff} being intermediate between ε_0 and ε_∞ [Even 2014b, Umari 2014, Brivio 2014, Wehrenfennig 2014a].

It is noticeable that the values for ε_{eff} are significantly lower for the tri-bromides, where the higher reduced masses cause the binding energy to be larger, with a consequent reduction in the strength of the screening. Due to the higher uncertainty in the values of R^* for the MAPbBr₃, at present we cannot consider the significance in the difference in ε_{eff} between the Methylammonium and Formamidinium tri-bromides.

The results for the crucial electronic parameters obtained at low temperatures may be now compared with our studies for the materials transformed to higher temperature tetragonal phase, characterized by an enhanced symmetry. To discuss the changes, in Fig. 4.12(b), we supplement the low temperature band-gap dependence of μ and R , previously presented in panel (a), with the values obtained for the tetragonal phase. The phase transition seems to have limited impact on the value of the reduced mass μ , which has been suggested in the previous studies of MAPbI₃, where no change was observed. Although our results indicate that after the phase transition the μ may increase by up to 10 % with respect to the 2 K values, this is still at the limit of the accuracy of the high temperature results. We then conclude, that the whole family of organo - lead trihalide perovskites may be described with Equation 4.8 in the terms of single parameter - the band gap energy, regardless of the crystalline phase or the temperature.

However, the effective dielectric constant ε_{eff} and consequently the exciton binding energy R^* are more affected by the transformation from orthorhombic to tetragonal phase. This is connected with additional collective rotational motion of the organic cations, allowed at higher temperatures, and further increasing the screening of the Coulomb potential [Poglitsch 1987]. The reduction of the ε_{eff} in the tetragonal phase has been suggested in several theoretical works. In a previously

cited report of Even et al. [Even 2014b], a value of approximately 5 meV is proposed for the exciton binding energy in MAPbI_3 in the tetragonal phase independently on the temperature. Another study with a similar approach of fitting absorption spectra [Yamada 2015] suggest the gradual reduction of R^* from 30 meV at low temperatures to 6 meV at 300 K. A decrease from 25 to 12 meV was also reported [Soufiani 2015]. This has a further experimental confirmation in the direct magneto-spectroscopic measurements, such as recent results of Miyata et al. [Miyata 2015] for MAPbI_3 and this work. We find the values of R^* for the iodide-based materials to be reduced to the range of 10 ± 3 meV, resulting in a rise in ε_{eff} . Moreover, the diamagnetic shift observed for 1s state is anomalously low when compared to the simulations (see Fig. 4.11(a),(b)), which may be an evidence for field-dependent increase in the exciton binding energy [Behnke 1978]. Therefore, the zero-field value of R^* may be even smaller, of the order of 5 meV predicted by Even et al. [Even 2014b], or less. By contrast, the FAPbBr_3 shows no significant reduction in the exciton binding energy in the higher temperature tetragonal phase, probably because the original binding energy corresponds to a frequency which is too high to respond to the additional screening. As a result, the low field diamagnetic shift is close to the theoretical prediction.

4.5 Conclusions

We performed magneto-transmission studies for several representatives of organo-lead halide perovskites, containing Methylammonium and Formamidinium organic cations. From the studies of iodine and bromine based materials, we obtain general relations for the exciton binding energy R^* and the reduced mass μ , which are principally determined by the band gap E_g for the whole family of hybrid perovskites. With the approximated values of $R^* = 0.01 \times E_g$ and $\frac{\mu}{m_0} = \frac{E_g}{16.6}$, the basic electronic properties can be easily estimated for newly synthesized compounds. There is no evidence for a significant influence of the organic cation type other than resulting from the changes in the band gap. This suggests that a simple two band $\mathbf{k} \cdot \mathbf{p}$ perturbation should enable the accurate modeling of the properties of devices made from materials in this system. We also demonstrate that the low temperature values of the exciton binding energies are smaller or comparable to the thermal energy at 300 K which makes a significant contribution to understanding the excellent performance of these devices in photovoltaic applications. For the tri-iodides, these values fall still further in the high temperature phase of the materials probably due to increased screening, which is not observed for FAPbBr_3 .

CHAPTER 5

Spatially resolved micro - photoluminescence studies of organo-lead halide perovskites

Contents

5.1	Introduction	67
5.2	Temperature dependence studies	68
5.3	Spatially resolved μ-PL at room temperature	71
5.4	Spatially resolved μ-PL below the phase transition temperatures	72
5.4.1	MAPbI ₃ and FAPbI ₃	72
5.4.2	MAPbCl _x I _{3-x}	75
5.4.3	FAPbBr ₃	76
5.5	The coexistence of crystalline phases in the proximity of strain or defects	77
5.6	Conclusions	80

This chapter describes the investigation of the morphology in several representatives of the organo lead halide perovskite family using spatially resolved μ -PL performed at different temperatures. We demonstrate that the perovskite thin film has a crystalline grain structure. Dark and bright grains are observed independently of the temperature in all studied materials. We also show, that the low temperature phase transition, from the tetragonal to orthorhombic crystal structure, is not uniform across the perovskite film. The remains of the high temperature tetragonal phase can be found even at very low temperatures. This suggests that the observed inhomogeneities result from the varying halide content, a hypothesis which is supported by the enhanced occurrence of tetragonal inclusions in the halide-depleted regions.

5.1 Introduction

Due to their spin-coated nature, perovskite thin films have a limited uniformity [Chen 2014b, Zhou 2014, Eperon 2014b]. The structural defects and non-stoichiometrical inclusions, formed during the solvent evaporation, can adversely influence the device performance. However, to date there is a limited number of investigations of the impact

of the perovskite thin film morphology on solar cell efficiency. Only recently, the significant inhomogeneities of the perovskite thin film, affecting their performance, have been shown [de Quilettes 2015]. Combined scanning electron microscopy and confocal microscopy methods were applied to study a film of $\text{MAPbCl}_x\text{I}_{3-x}$, produced in the same way as the material used for photovoltaic devices. The film structure revealed the presence of microcrystalline grains with size of the order of a few micrometers. The photoluminescence intensity and the carrier lifetime were found to strongly depend on the position across the film, as a result of the existence of specific, dark grains. Such dark grains are characterized by an emission intensity weakened approximately by a factor of four and a reduced carrier lifetime. The dark grains act as non-radiative traps for the photo-created carriers, leading to a decrease of the overall solar cell performance. As an example of a method to reduce the number and impact of the dark grains, the substitution of Methylammonium cations with guanidine was proposed [Marco 2016]. These results underline the importance of the material morphology for the future development of perovskite thin film technology.

In this chapter, we investigate the microscopic properties of organo-lead halide perovskites with spatially resolved micro-photoluminescence performed at different temperatures. We show that the presence of the bright and dark crystalline grains is an intrinsic property of the hybrid perovskites. We also demonstrate that not all of the grains undergo the low temperature transition from the tetragonal to orthorhombic phase, with some grains remaining in the high temperature phase even at $T = 4$ K. As this phenomenon clearly intensifies in the proximity of structural defects, we attribute the incomplete phase transition to variations in the halide content.

5.2 Temperature dependence studies

The μ -PL studies were performed for several Methylammonium and Formamidinium based compounds, in the experimental setup which are described in Chapter 2. First, the case of the archetypal MAPbI_3 compound will be discussed. The μ PL spectra, typical for this material, acquired for one position on the sample in the temperature range from 4 K to 200 K are presented in Fig. 5.1(a). At temperatures of 130 K or above, the spectra show only a single emission peak from the tetragonal phase (TP) [Kong 2015]. However, the picture becomes more complicated as the temperature is lowered. Between 130 K and 110 K another peak appears, with an emission energy higher by around 90 meV. This peak gains in intensity as the temperature further decreases, becoming dominant at around 100 K. Thus, we attribute this emission to the low temperature, orthorhombic phase (OP). At low temperatures, below 60 K, the orthorhombic phase peak has a shoulder towards the low energy side, at around 1635 meV, which is evidence for emission from the orthorhombic phase bound exciton.

It is remarkable that the first observation of OP emission occurs far below the

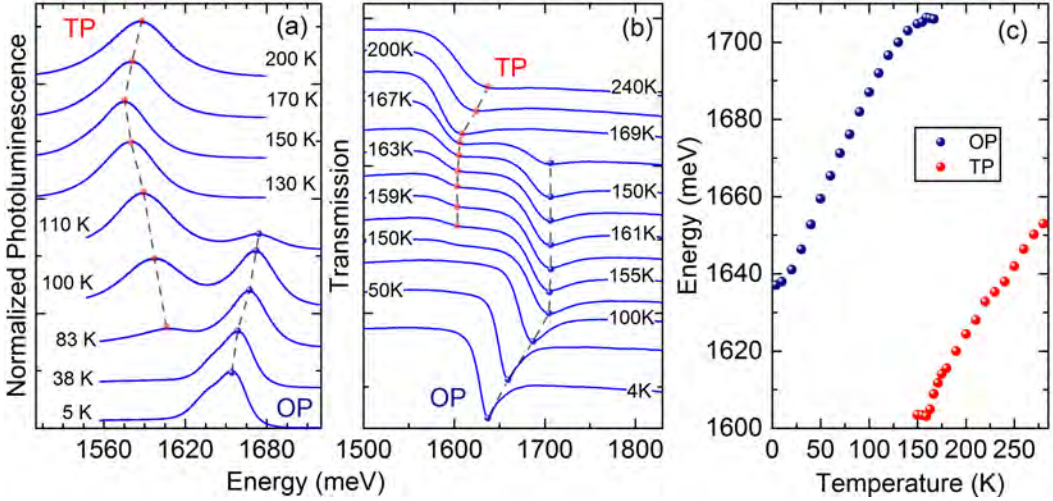


Figure 5.1: (a) μ PL spectra, (b) transmission spectra and (c) energy of the absorption as a function of temperature for MAPbI_3 .

temperatures $\simeq 150 - 160$ K, where the phase transition is expected, as discussed in the Chapter 3. Moreover, there is some evidence for the coexistence of both phases over a temperature range of almost 30 K, as the tetragonal phase peak is still detected at 80 K (see Fig. 5.1(a)). To further investigate the evolution of the phase transition with temperature, complementary measurements of the absorption were performed. The typical transmission spectra for MAPbI_3 taken at different temperatures are presented in the Fig. 5.1 (b), while panel (c) shows resulting absorption energies plotted as a function of the temperature. To precisely follow the phase transition progress, the separation between the data points has been reduced to 2 K in the temperature range between 150 K to 170 K. The spectra plotted in Fig. 5.1 (b) reveal the simultaneous presence of two absorption minima, corresponding to both orthorhombic and tetragonal phases. As shown in panel (c), the transition from tetragonal to orthorhombic phase causes an abrupt increase of around 90 meV in the energy of the absorption edge. Such observations have already been reported [Wang 2015a, Kong 2015], also with the simultaneous detection of both absorption edges [Yamada 2015]. Moreover, the temperature dependence of the high temperature phase reveals a turning point at 168 K, as we observe a continuous band gap energy increase above this value. This leads to the conclusion that above 168 K the material is entirely in the tetragonal phase, as no trace of the OP is found above 170 K in both transmission and the μ PL studies. However, there is a significant difference in the temperature evolution of the relative intensity of both phases when we compare the absorption and photoluminescence results. The emission of the tetragonal phase peak dominates the PL spectrum already at 110 K, while the tetragonal phase absorption is detected not sooner than 145 K. It takes a further 20 K until it dominates the OP absorption, which quickly diminishes between 165 K

and 170 K. These phenomena can be explained by a concurrent collection of photo created carriers in grains of different crystalline phases, which is further discussed in the Section 5.3.

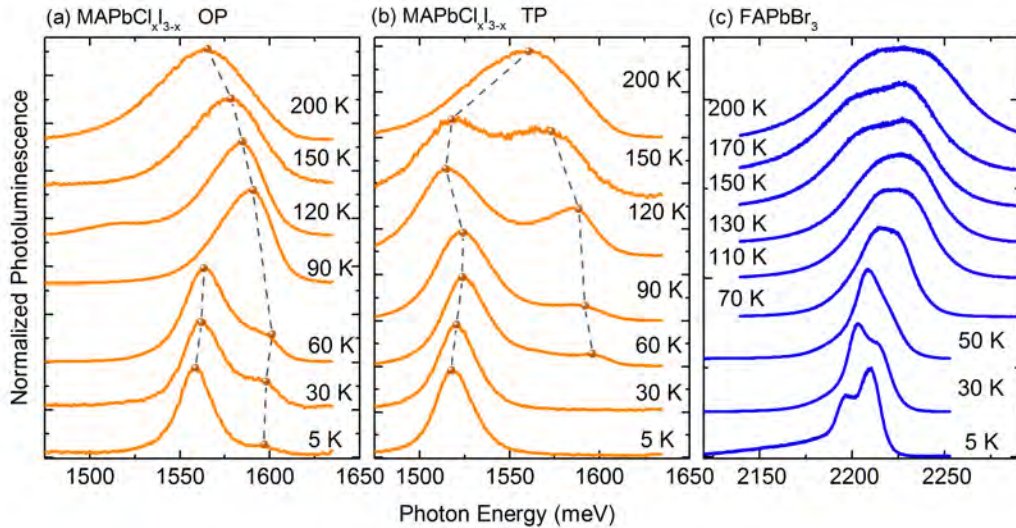


Figure 5.2: (a),(b) Temperature dependence of the μ PL for two different spot positions on $\text{MAPbCl}_x\text{I}_{3-x}$ corresponding to the domains of the orthorhombic and tetragonal phases, respectively. (c) Temperature dependence of the μ PL spectra for FAPbBr_3

In the case of the mixed halide material, $\text{MAPbCl}_x\text{I}_{3-x}$, the presence of the tetragonal phase at low temperatures is even more significant than in the pure triiodide. In this compound, both phases can be fully resolved, leading to the observation of areas, where exclusively one of the phases is detected. The typical spectra acquired at two such positions, measured as a function of the temperature, are shown in Fig. 5.2 (a) and (b). Panel (a) represents the transition from the tetragonal to orthorhombic phase, whereas panel (b) refers to the region which remains in the tetragonal phase even at $T = 4$ K. In the Fig. 5.2 (a), the tetragonal phase emission totally vanishes below 120 K. The remaining orthorhombic phase peak has a high energy shoulder at ≈ 1600 meV, which is attributed to orthorhombic phase free exciton emission. Below 60 K, the intensity of the orthorhombic phase free exciton considerably decreases, and the emission is dominated by the peak around 1560 meV, which corresponds to the orthorhombic phase bound exciton state. In contrast, the spectra in Fig. 5.2 (b) show the dominance of the tetragonal phase peak, which starts already at the phase transition temperature. With further temperature decrease, the orthorhombic phase peak is consequently weakened, and no remains of it are found at temperatures of 30 K or below. The emission energy of tetragonal phase peak at low temperatures is at ≈ 1525 meV, reproducing the energy shift between tetragonal and orthorhombic phases identified at the phase

transition temperature.

An evidence for the coexistence of different phase domains at low temperatures is also found in the high band gap FAPbBr_3 . The typical μ -PL spectra measured at various temperatures are presented in the Fig. 5.2 (c). At around 150-160 K the low energy component of the high temperature emission peak is suppressed. In contrast to the iodine based compounds, in the vicinity of the phase transition we do not observe well resolved peaks, which can be identified with either orthorhombic or tetragonal crystalline phases. However, the reduction of the spectral width with decreasing temperature reveals two strong peaks, which are well resolved below 30 K. These strongly position - dependent spectral features are separated by only around 15 meV, which is a few times less than in the case of the iodine- based compounds.

Thus, the presence of the remains of the tetragonal phase far below the phase transition temperature is observed in all studied materials. It is a strong indication for the inhomogeneous progress of the phase transition in perovskite films. This complexity is interesting for further investigation with spatially resolved methods, in order to evaluate the magnitude and size of the tetragonal phase inclusions.

5.3 Spatially resolved μ -PL at room temperature

The morphology studies performed at the room temperature are important due to their relevance for the operation of photovoltaic devices. The results of spatially resolved room temperature μ PL for MAPbI_3 , $\text{MAPbCl}_x\text{I}_{3-x}$ and FAPbBr_3 , respectively, are presented in the Fig. 5.3 (a)-(c). The color maps, each $80 \times 80 \mu\text{m}$ with a $2 \mu\text{m}$ step, represent the integrated intensity of the photoluminescence peak. In all the samples we observe noticeable variations of the emission intensity across the investigated areas, revealing the presence of the regions of stronger and weaker photoluminescence. We therefore conclude, that all three compounds have micro-crystalline grain structure, and that the recently reported presence of the dark grains [de Quilettes 2015, deQuilettes 2016] is typical for organo lead halide perovskites.

The archetypal MAPbI_3 forms a relatively uniform layer, with the dominance of bright areas (Fig. 5.3 (a)). The grain size can be estimated to between 5 and $10 \mu\text{m}$, and the PL intensity ratio of the bright to dark grains is around 5, similar to the ratios reported in the Reference [de Quilettes 2015]. The high temperature properties of the $\text{MAPbCl}_x\text{I}_{3-x}$ compound are very similar (panel (b)). However, the grain size in the case of the mixed halide is considerably larger, typically around $10-20 \mu\text{m}$, which may contribute to the reported better performance of $\text{MAPbCl}_x\text{I}_{3-x}$ based devices [Deschler 2014]. In contrast, the FAPbBr_3 film (panel (c)) is considerably less uniform. The increased number of the dark grains is accompanied by an increased bright-to-dark grain emission intensity ratio, of the order of 10. The grain size, similarly to MAPbI_3 , varies between 5 and $10 \mu\text{m}$.

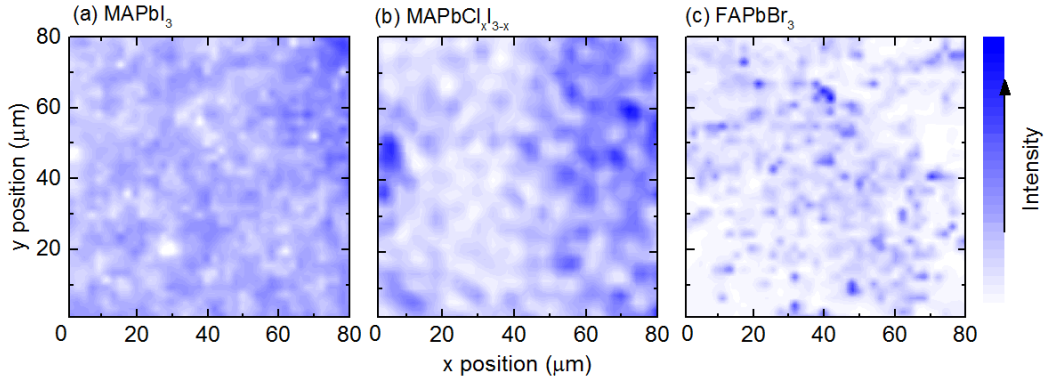


Figure 5.3: Integrated intensity of the μ PL peak as a function of the position for (a) MAPbI_3 , spot illumination intensity 40 nW (4 W/cm^2), (b) $\text{MAPbCl}_x\text{I}_{3-x}$, spot illumination intensity 60 nW (6 W/cm^2), and (c) FAPbBr_3 , spot illumination intensity 100 nW (10 W/cm^2), respectively at 300K. The integrated intensity increases from white to blue. The scanning step is $2\mu\text{m}$.

5.4 Spatially resolved μ -PL below the phase transition temperatures

5.4.1 MAPbI_3 and FAPbI_3

The low temperature ($T = 4 \text{ K}$) spatially resolved μ PL for MAPbI_3 is presented in the Fig. 5.4. Panel (a) shows photoluminescence from the low temperature, orthorhombic phase. Similarly to the room temperature results (Fig. 5.3 (a)), the emission is fairly uniform, with some variation on a few μm scale related to the microcrystalline structure of the perovskite film. Nevertheless, we still observe the dark and bright grains. Remarkably, the low energy peak, corresponding to the high temperature tetragonal phase, accompanies the orthorhombic emission at certain positions across the sample. The typical spectra acquired for two different positions on the sample are presented in the panel (c). The spectrum drawn with the blue curve represents a position, where only the orthorhombic peak occurs. The red curve corresponds to the position, where both orthorhombic and tetragonal phase peaks are detected simultaneously. The difference in the emission energy between the tetragonal and orthorhombic phase peaks is the same as the change in the band gap observed at the phase transition temperature (see Fig. 2.5), where the tetragonal phase absorption is lower in energy by approximately 90 meV. Although the intensity of the tetragonal phase emission is always lower than the intensity of dominant orthorhombic phase peak, the occurrence of the tetragonal phase peak appears to decrease the intensity of the OP peak. The integrated intensity of the tetragonal phase peak, indicated with the red color, is superimposed upon the integrated intensity of orthorhombic phase peak in Fig. 5.4 (b). The tetragonal phase

5.4. Spatially resolved μ -PL below the phase transition temperatures 73

emission is found within rather infrequent, isolated areas of typical size of 1 to 5 μm , where the orthorhombic phase peak is usually weaker. To precisely determine, if there is a correlation between the emission intensities of the two phases, we analyze the proportions of the total emission in each peak $\frac{I_{OP,TP}}{I_{TP}+I_{TP}}$ as a function of the emission intensity of the tetragonal phase peak (I_{TP}). The results, presented in Fig. 5.4 (d) reveal an anti-correlation: as the proportion of the emission in the tetragonal phase peak (orange points) rises, the OP phase falls progressively.

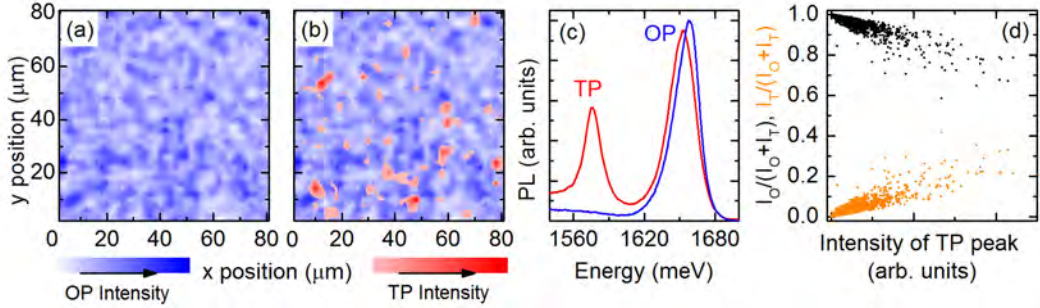


Figure 5.4: Spatially resolved micro-photoluminescence for MAPbI_3 : (a) Integrated intensity of the high energy (OP) peak as a function of position. The intensity increases from white to dark blue. (b) A second map of the low energy (TP) peak is superimposed onto the map shown in (a). The intensity increases from white to red. (c) Typical spectra for positions where only the OP peak was observed (blue) and where both peaks were observed (red). (d) Correlation of the integrated intensity of the TP (orange) and OP (black) peaks versus intensity of the low energy TP peak. All the measurements have been performed at $T = 4$ K, with the scanning step 2 μm and spot illumination intensity 5 nW (0.5 W/cm²).

A similar behaviour is found in a Formamidinium triiodide. The low temperature μPL map for the FAPbI_3 sample is presented in Fig. 5.5. Similarly to MAPbI_3 , the intensity of the orthorhombic phase peak (indicated with the blue color in panel (a)) is relatively uniform across the sample, with isolated inclusions of the tetragonal phase (superimposed upon the orthorhombic phase map with the red color in panel (b)). Again, the regions of the occurrence of the emission from the tetragonal phase are few μm in size. However, in FAPbI_3 , the relative intensity of the tetragonal phase is increased, and at certain positions is comparable with the intensity of the orthorhombic phase peak. An example of such behaviour is presented in the panel (c), containing typical spectra, which correspond to the positions of the dominance of the orthorhombic phase peak (the blue curve) and a significant presence of the tetragonal phase peak (the red curve). The $\frac{I_{OP,TP}}{I_{TP}+I_{TP}}$ ratios plotted in the panel (d) confirm that both phases can similarly contribute to the total emission.

The results obtained on the triiodides strongly indicate the coexistence of two crystalline phases at low temperatures, proving that although the majority of the film transforms into the orthorhombic phase, certain perovskite grains remain in

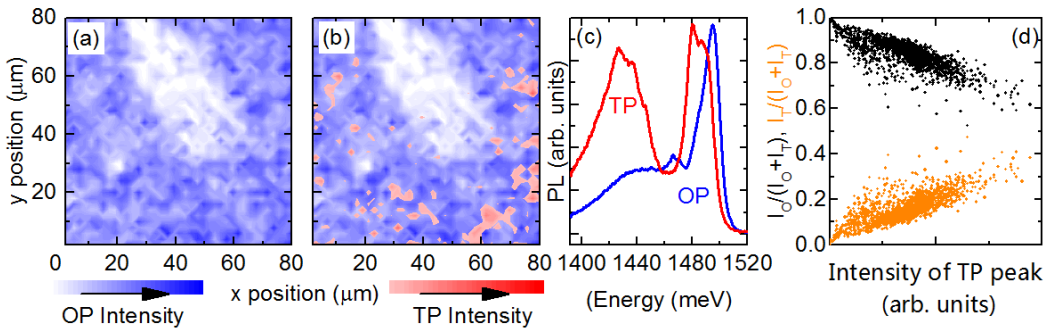


Figure 5.5: (a) Integrated intensity of the high energy (OP) peak as a function of position for FAPbI_3 . The intensity increases from white to dark blue. (b) A second map of the low energy (TP) peak is superimposed onto the map shown in (a). The intensity increases from white to red. (c) Typical spectra for positions where only the OP peak was observed (blue) and where both peaks were observed (red). (d) Correlation of the integrated intensity of the TP (orange) and OP (black) peaks versus intensity of the low energy TP peak. All the measurements have been performed at $T = 4\text{ K}$, with the scanning step $2\text{ }\mu\text{m}$ and spot illumination intensity 5 nW (0.5 W/cm^2).

the tetragonal phase far below the phase transition temperature. The phase domains collect the photo created carriers concurrently, which is revealed in the positive/negative intensity correlation. Due to the lower band gap, the micro-domains of the high temperature tetragonal phase might preferably collect the carriers excited in the orthorhombic phase regions, as it was suggested previously for $\text{MAPbCl}_x\text{I}_{3-x}$ [Wehrenfennig 2014b]. This is consistent with the comparison of photoluminescence and transmission measured as a function of temperature (see Fig. 5.2 and Fig. 5.1). The tetragonal phase peak dominates the PL for temperatures significantly below the phase transition, while remaining undetectable in absorption. The separations of the tetragonal inclusions are typically of the order of $10 - 20\text{ }\mu\text{m}$. This is an indication that the diffusion length in these materials remain at a comparable value until the temperature falls below 80 K , where we can completely resolve both phases. It also suggests the importance of the inter grain diffusion in this temperature range. Since the diffusion lengths are expected to be proportional to \sqrt{T} at low temperatures, and PL is excited by the laser spot of approximately $1\text{ }\mu\text{m}$ diameter, the low temperature maps give an upper limit to the size of the tetragonal phase domains. This limit is in the range of a few μm , which is comparable with the size of individual crystallites. However, the tetragonal domains may be even smaller. As the perovskite materials are characterized by relatively long diffusion lengths [Stranks 2013, Xing 2013], the excitons can be supposedly collected over comparable distances even by the microscopic scale regions of a smaller band gap material. As a consequence, these small regions can dominate the PL response without re-

5.4. Spatially resolved μ -PL below the phase transition temperatures⁷⁵

vealing a detectable absorption in the transmission measurements. Thus, the overall proportion of the high temperature tetragonal phase, estimated with the spatially resolved PL images to be not higher than a few per cent of the total area, may be significantly smaller.

5.4.2 MAPbCl_xI_{3-x}

We turn now to the material synthesized in the presence of chloride precursors, namely MAPbCl_xI_{3-x}. The μ PL maps measured at 4 K and 150 K are presented in Fig. 5.6. Panels (a) - (d) contain the results of the low temperature scan, while panels (e) - (h) refer to data acquired at 150 K, over a different region of the sample. The integrated intensity of the orthorhombic phase peak (panels (a) and (e) for 4K and 150K, respectively) show similar structure as in the room temperature scan (Fig. 5.3 (b)), with a grain structure of the typical size in the order of 5-10 μ m. However, when we superimpose the map of tetragonal phase emission upon the OP distribution, we find a strong positive/ negative correlation between both the phases, as presented in the panels (b) and (f). In the regions of tetragonal phase inclusions, the intensity of the orthorhombic phase peak is significantly weakened or completely suppressed. Furthermore, the size of the phase domains, considerably larger than in the pure iodides, is scalable with the size of crystalline grains. This allows the orthorhombic and tetragonal phases to be completely resolved. This effect is especially clear at 4 K, where we practically do not observe simultaneous emission from both phases. This anti correlation is additionally proved by the $\frac{I_{OP,TP}}{I_{TP}+I_{TP}}$ ratios, plotted in the panels (d) and (h). The positive / negative correlation of integrated PL is clear in both cases: the maximum for the orthorhombic phase peak corresponds to the minimum for the tetragonal phase peak.

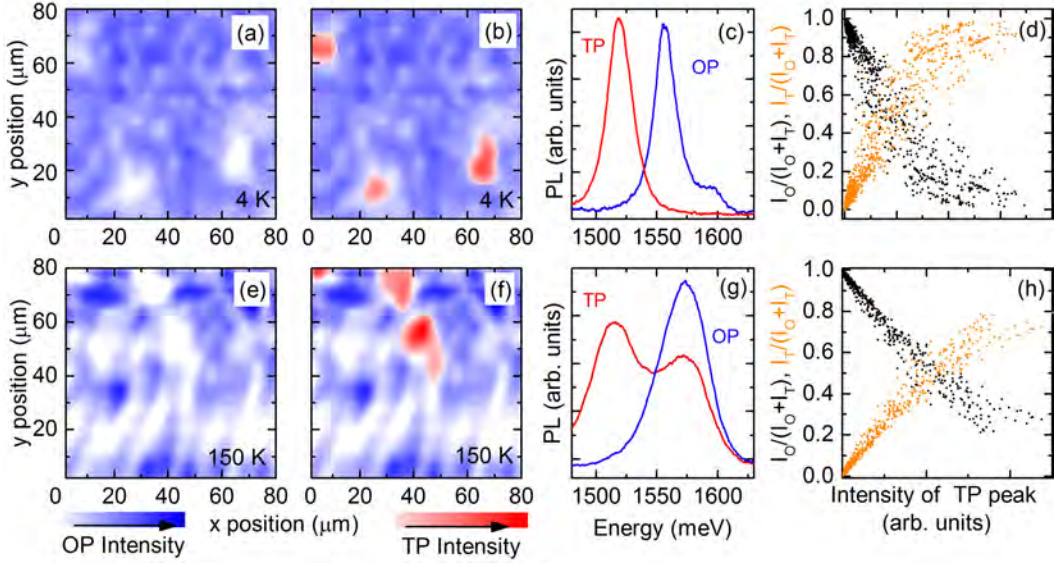


Figure 5.6: (a) Integrated intensity of the high energy (OP) peak as a function of position for $\text{MAPbCl}_x\text{I}_{3-x}$. The intensity increases from white to dark blue. (b) A second map of the low energy (TP) peak is superimposed onto the map shown in (a). The intensity increases from white to red. (c) Typical spectra for positions where only the OP peak was observed (blue) and where the TP peak was seen also (red). (d) Correlation of the integrated intensity of the TP (orange) and OP (black) peaks versus intensity of the low energy TP peak. (a) - (d) were performed at 4K, spot illumination intensity 0.3 nW, and (e) - (h) show the same measurements performed at 150K, spot illumination intensity 3 nW (0.3 W/cm^2). The scanning step was $2 \mu\text{m}$.

5.4.3 FAPbBr_3

The results obtained for iodine based materials are supplemented by the investigation of another halide compound, a large band gap FAPbBr_3 . The low temperature mapping over a $180 \times 180 \mu\text{m}$ region, is presented in the Fig. 5.7. It shows that the spatial scale of the variations in the photoluminescence intensity is remarkably larger than those observed in the iodides or mixed halide. The phase domain structure in the bromide is seemingly independent on the grain structure of the layer, with the domains spreading over $100 \mu\text{m}$. As seen in the Fig 5.7 (a), the integrated emission of the orthorhombic phase peak at 2205 meV is present only in a limited area of the sample, while most of the film practically does not emit at this energy. However, the emission of the tetragonal phase peak at 2190 meV, indicated with the red color in panel (b) is complementary to the emission of the low temperature phase. The occurrence of the tetragonal phase corresponds very well to the dark region of the orthorhombic phase emission, while both tetragonal and orthorhombic intensities are relatively uniform and continuous within their domains. The spectra

from both regions are well resolved, as seen in the Fig 5.7(c). This marked positive/negative correlation is also revealed in the $\frac{I_{OP,TP}}{I_{TP}+I_{TP}}$ ratios, plotted as a function of orthorhombic phase peak intensity in the Fig. 5.7(d).

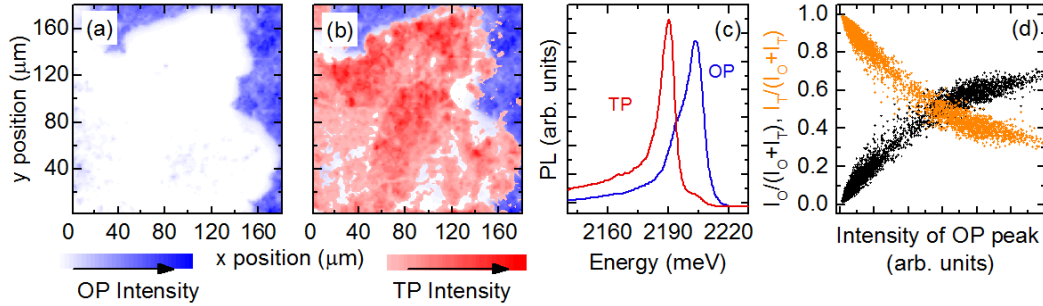


Figure 5.7: (a) Integrated intensity of the high energy (OP) peak for FAPbBr_3 : as a function of position. The intensity increases from white to dark blue. . (b) A second map of the low energy (TP) peak is superimposed onto the map shown in (a). The intensity increases from white to red. (c) Typical spectra for positions where only the OP peak was observed (blue) and where both peaks were observed (red). (d) Correlation of the integrated intensity of the TP (orange) and OP (black) peaks versus intensity of the TP peak. All the measurements have been performed at $T = 4$ K, with the scanning step $2 \mu\text{m}$ and spot illumination intensity 5nW (0.5 W/cm^2).

The presence of the macroscopic domains possibly originates from a relatively small difference between the emission energy of the two phases, which is only 15 meV. This suggests that the difference in the band structure or the free energy between the two phases may also be smaller, as has been shown previously [Kunugita 2015]. This would facilitate the propagation of a particular structure towards adjacent grains, creating domains of $100 \mu\text{m}$ in size or greater.

5.5 The coexistence of crystalline phases in the proximity of strain or defects

Naturally formed defects in the perovskite thin film are the first candidates to be considered as the cause of the observed inhomogeneities in the progression of the phase transition. Here, we will discuss the coexistence of the orthorhombic and tetragonal phases within damaged or strained material. In the proximity of such defects, we observe an enhanced occurrence of the tetragonal phase at low temperatures, which brings further insight into the origin of domain-formation behaviour observed in the organic/inorganic perovskites.

To investigate this, we intentionally introduced a defect in the perovskite thin film material by exposing it to a focused laser spot. It has been shown, that photo -

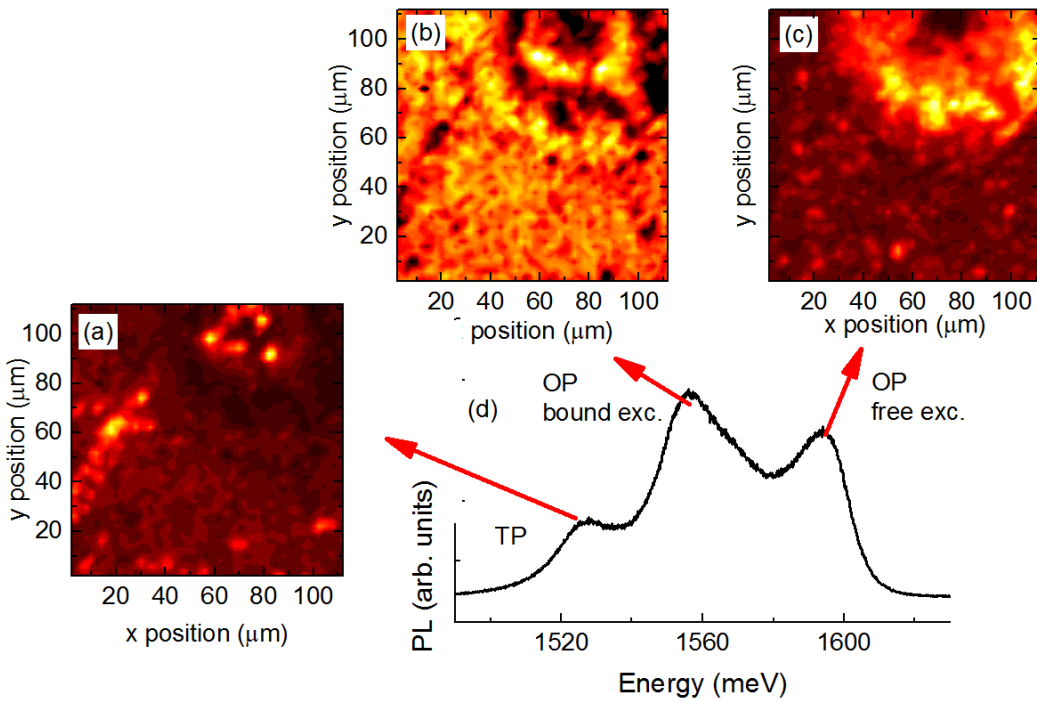


Figure 5.8: Spatially resolved micro-photoluminescence for $\text{MAPbCl}_x\text{I}_{3-x}$ in the region exposed to the focused laser spot; $T = 5 \text{ K}$, scanning step $2 \mu\text{m}$: (a)-(c) Integrated intensities across the sample for: tetragonal phase (a), bound (b) and free (c) excitons of orthorhombic phase. (d) Photoluminescence spectrum revealing all observed transitions.

annealing induces the migration of halide ions away from the point of exposure, influencing the PL properties of the material [deQuilettes 2016]. We scanned another region of the $\text{MAPbCl}_x\text{I}_{3-x}$ sample, which was illuminated for several minutes with a 532 nm laser spot of high power density (10^5 W/cm^2) at room temperature. The low temperature μPL for that area is presented in the Fig 5.8. A typical PL spectrum plotted in the panel (d) contains three emission peaks at 1535 meV, 1555 meV and 1600 meV, attributed to the tetragonal phase, and bound/free exciton of orthorhombic phase, respectively. The map reveals the dominance of the OP bound exciton across the sample (panel (b)). The center of the laser spot is a dark core (upper right corner of the map). This region of a very weak PL is surrounded by spots of bright emission from the tetragonal phase (panel (a)). Consecutively, we observe ring-shaped areas where the bound and free exciton of the orthorhombic phase dominate (panels (b),(c), respectively).

Such a distribution of the phase domains can be explained by the presence of regions of decreased and enhanced halide content, formed during the photo annealing. We expect that the ion migration reported in [deQuilettes 2016] would cause

a non - uniform halide distribution in the exposed area, as schematically presented in Fig. 5.9. The intensive light creates a depleted region, surrounded by the region with iodine excess. The crystalline phases are correlated with the halide content, which is in agreement with the pattern of domains observed in the colour maps from Fig. 5.8. The depleted region in the center of the laser spot has a weak photoluminescence. Moving away from that center (with increasing iodine content) we observe sequentially the rings of emission from the tetragonal phase (a), orthorhombic phase bound excitons (b), orthorhombic phase free excitons (c). The unaffected regions are characterized by the emission of the orthorhombic phase bound exciton. Thus, the orthorhombic phase bound exciton emission characterizes the standard iodine content, while the presence of the tetragonal phase indicates a deficiency of the halide. The orthorhombic phase free excitons are only dominant at low temperatures in the regions of enhanced iodine content.

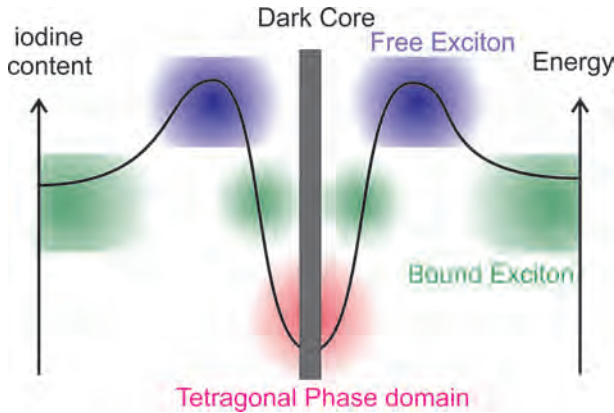


Figure 5.9: The schematic drawn of photo-annealing induced distribution of iodine ions as a function of the distance from the point of exposure.

The picture of the emission being controlled by the iodine content is supported by the further results of low temperature μ PL mapping on the FAPbI₃ sample, shown in the Fig. 5.10. It presents a selected region in the proximity of a dark ribbon of approximately 100 μ m length, which is probably a crack or a fissure. In comparison with the homogenous region pictured in Fig. 5.5, we observe an intensified presence of the high temperature tetragonal phase (compare the red areas in the panels (b) of Fig. 5.5 and Fig. 5.10), which is localized mainly at the ribbon borders. The tetragonal phase domain grains in the proximity of the dark region are also significantly larger than in the uniform parts of the sample. Furthermore, the positive / negative correlation of the orthorhombic and tetragonal phase peaks (panel (d)) is here more highlighted than in the uniform region. This observation, featuring enhanced presence of tetragonal phase around the weakly emitting region, can be considered as a 1D analogy to the photo annealing. This is also consistent with the the iodine content being significantly perturbed close to the edges of cracks formed during film deposition.

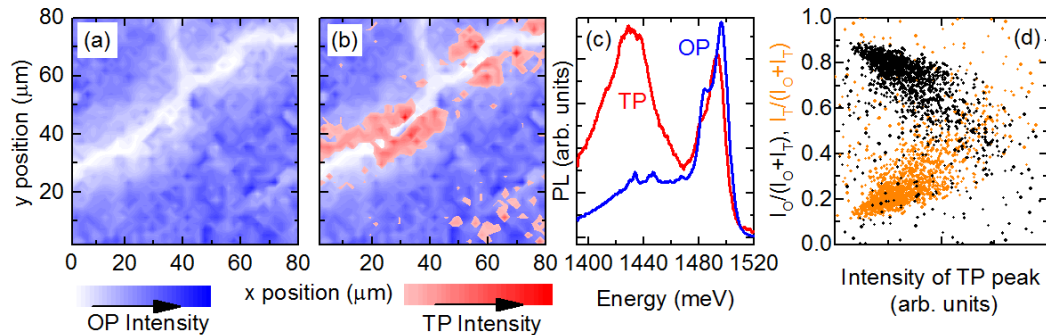


Figure 5.10: Spatially resolved micro-photoluminescence for FAPbI_3 in the proximity of a dark ribbon: (a) Integrated intensity of the high energy (OP) peak as a function of position. The intensity increases from white to dark blue. (b) A second map of the low energy (TP) peak is superimposed onto the map shown in (a). The intensity increases from white to red. (c) Typical spectra for positions where only the OP peak was observed (blue) and where both peaks were observed (red). (d) Correlation of the integrated intensity of the TP (orange) and OP (black) peaks versus intensity of the low energy TP peak. All the measurements have been performed at $T = 4$ K, with the scanning step $2 \mu\text{m}$ and spot illumination intensity 5nW (0.5 W/cm^2).

5.6 Conclusions

We performed temperature-dependent spatially resolved micro-Photoluminescence on different representatives of organo - lead halide perovskite family. The resulting maps show that perovskite thin films are composed from the dark and bright crystalline grains, which are around few micrometer in size, and up to $20 \mu\text{m}$ in the case of the mixed halide $\text{MAPbCl}_x\text{I}_{3-x}$. We demonstrate that the low temperature phase transition from tetragonal to orthorhombic phase is incomplete in all studied materials, as the remains of the tetragonal phase are found even at $T = 4$ K. This is most evident in the FAPbBr_3 , where macroscopic domains of both orthorhombic and tetragonal phases coexist at low temperatures. In other compounds, the area of tetragonal inclusions is limited to the size of single crystalline grains. These inclusions can be even smaller, as due to the long carrier diffusion lengths reported for the perovskites, the lower band gap tetragonal material can preferably collect the carriers over large regions, which gives a rise to a relatively strong PL peak corresponding to the tetragonal phase. By investigating damaged and photo annealed regions, where the occurrence of the tetragonal phase at low temperatures is enhanced, we attribute its presence to the depleted halide content.

CHAPTER 6

Caesium lead halide perovskites - characterization and magneto-optical studies

Contents

6.1	Fully inorganic caesium-based perovskite compounds	81
6.2	Characterization of the samples	83
6.3	Low-temperature magneto - transmission	84
6.4	Discussion	87

In this chapter, we briefly discuss our preliminary results obtained for the family of fully inorganic caesium lead halide perovskites. First, we describe the samples and the characterization of the temperature dependence of the band gap. Then, we present the low-temperature measurements of exciton binding energy and effective mass determined using magneto-spectroscopy.

6.1 Fully inorganic caesium-based perovskite compounds

The family of caesium lead halides has also been investigated as potential perovskite light absorbers [Eperon 2015, Kulbak 2015, Beal 2016]. In particular, the CsPbI₃, characterized by a band gap of around 1.73 eV is considered as a suitable candidate for the top solar cell in tandem architectures [Beal 2016]. The main advantage of the fully inorganic CsPbX₃ materials over their hybrid, organic A-cation analogues is their resistance to high temperatures, up to their melting point at around 450 °C [Møller 1958, da Silva 2015, Kulbak 2016]. However, the relatively small ionic radius of the Cs⁺ cation (1.73 Å, comparable to the size of I⁻ anion) results in rather low values of the Goldschmidt's tolerance factor. Therefore, the CsPbX₃ compounds reveal a high level of structural distortion, while the relatively symmetric cubic structures are formed only at temperatures far above the operational conditions of the photovoltaic devices. In CsPbI₃, the perovskite, "black" cubic phase is stable above ≈ 320 °C [Møller 1958, Eperon 2015, da Silva 2015]. When the temperature is lowered, a transformation to the non-perovskite, orthorhombic "yellow" polymorph ($E_g \approx 2.8$ eV) occurs, which is schematically presented in Fig 6.1 [Møller 1958,

Trots 2008, Eperon 2015]. At room temperature and under the air, a full conversion to the yellow phase completes within minutes, or almost immediately in a humid environment. The changes in the structural properties are less abrupt, when smaller halides are incorporated in to the lattice. For example, all three polymorphs of CsPbBr_3 have a perovskite structure [Møller 1958, Sakata 1979] and similar band gaps in the range of 2.3-2.4 eV, corresponding to their orange colour [Kulbak 2015]. This compound transforms from the cubic to tetragonal phase at 130 °C and further to the orthorhombic structure at 88 °C [Møller 1958, Sakata 1979].

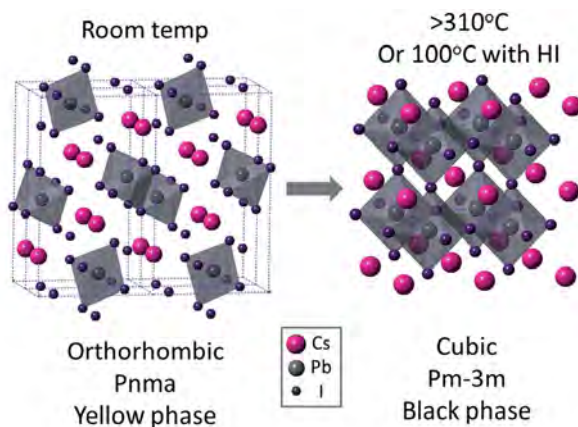


Figure 6.1: Two polymorphs of CsPbI_3 : non-perovskite "yellow" phase (left) and "black" perovskite cubic phase (right). After Reference [Eperon 2015].

Caesium versus the organic molecules The spherical symmetry of the Cs^+ cations significantly changes the picture of the interactions between the A-cations and the rest of the lattice, known from the case of the organic molecules. With the factors such as the cation orientation and the hydrogen bonds eliminated, the structural properties in the fully inorganic CsPbX_3 perovskites are governed by the Goldschmidt's tolerance factor in a more direct way. In hybrid perovskite compounds, the libration (rotation) modes of the organic lattice, allowed in the tetragonal (cubic) phase, contribute to the increase of the static dielectric constant and result in a dynamic disorder of the structure. One can intuitively expect that without these phenomena, the room-temperature electronic properties of the caesium-based compounds may significantly differ from the parameters describing their hybrid, organic-inorganic analogues. In particular, with no additional screening of the Coulomb interaction between the electron and hole, the exciton binding energies are expected to be almost identical to the low-temperature values.

The problems of structural stability (CsPbI_3) and the unsuitable band gap (CsPbBr_3) will presumably limit the development of photovoltaic devices based on fully inorganic Caesium perovskites. However, the organic-inorganic mixed cations compounds, containing the caesium atoms, are intensively studied due to their superior structural and temperature stability. This success is a motivation to define

the after-effects of the substituting of the organic molecules with Caesium atoms in the perovskite light absorbers, especially with respect to their electronic properties. Therefore, we are currently performing magneto-spectroscopic studies on the CsPbX_3 family, in order to determine the exciton binding energies and the reduced masses and compare the derived parameters with the results obtained for the organic-inorganic perovskites. In this chapter, we present our first, low-temperature results for CsPbBr_3 , CsPbBrI_2 and CsPbI_3 compounds.

6.2 Characterization of the samples

The samples were produced in the Clarendon Laboratory, Oxford, by Rebecca Sutton. Upon the arrival at LNCMI, the iodine-dominated CsPbBrI_2 and CsPbI_3 compounds were already converted to the orthorhombic phase. To restore the cubic phase in these materials, we use a procedure of a few-minute annealing at 350 °C, commonly described in the literature [Eperon 2015, da Silva 2015]. Immediately after the annealing, the samples are put into an inert helium gas atmosphere. To characterize the samples, we measure the energy of the near - band gap absorption as the function of temperature, using a macro-transmission technique. The methodology is the same as in the case of the organic-inorganic compounds, which was described in Section 3.4.

The transmission spectra, taken at different temperatures between 4 K and 270 K, are shown in Fig. 6.2. Panels (a)-(c) correspond to the spectra for CsPbBr_3 , CsPbBrI_2 and CsPbI_3 , respectively. As for the organic-inorganic perovskites, the absorption spectra are dominated by single absorption minima. With increasing temperature, the absorption energy blue-shifts, which is a phenomenon known from the hybrid perovskites (see Section 3.4). The transition energies for all three compounds are plotted as the function of temperature in Fig. 6.2 (d). Consistent with previous reports, which suggest the absence of phase transitions in this temperature range, the observed change of the absorption energy is continuous. These energies are in the range of 1725 – 1805 meV for CsPbI_3 (Fig. 6.2 (c)) and 1940 – 2000 meV for CsPbBrI_2 (panel (b)). This confirms that the cubic phase was successfully preserved even at low temperatures. In the case of CsPbBr_3 (Fig. 6.2 (a)), we have investigated both non-annealed material in the orthorhombic phase and a sample annealed at 250 °C in order to form the cubic phase (orange solid and black dashed curves, respectively). However, we do not observe any changes in the absorption spectra introduced by such annealing. This suggests that independently on the thermal processing, CsPbBr_3 will always transform to the orthorhombic phase below the phase transition point at 88 °C. Therefore, we conclude that preserving the iodine-rich compounds in the cubic phase is possible due to a relatively large energy required for a conversion to the significantly different, yellow polymorph. It is also important to note that the absorption spectrum of CsPbBr_3 has a well defined minimum even at 270 K, while the two other compounds encounter a considerably larger thermal broadening of the absorption shape. This minimum, more pronounced than

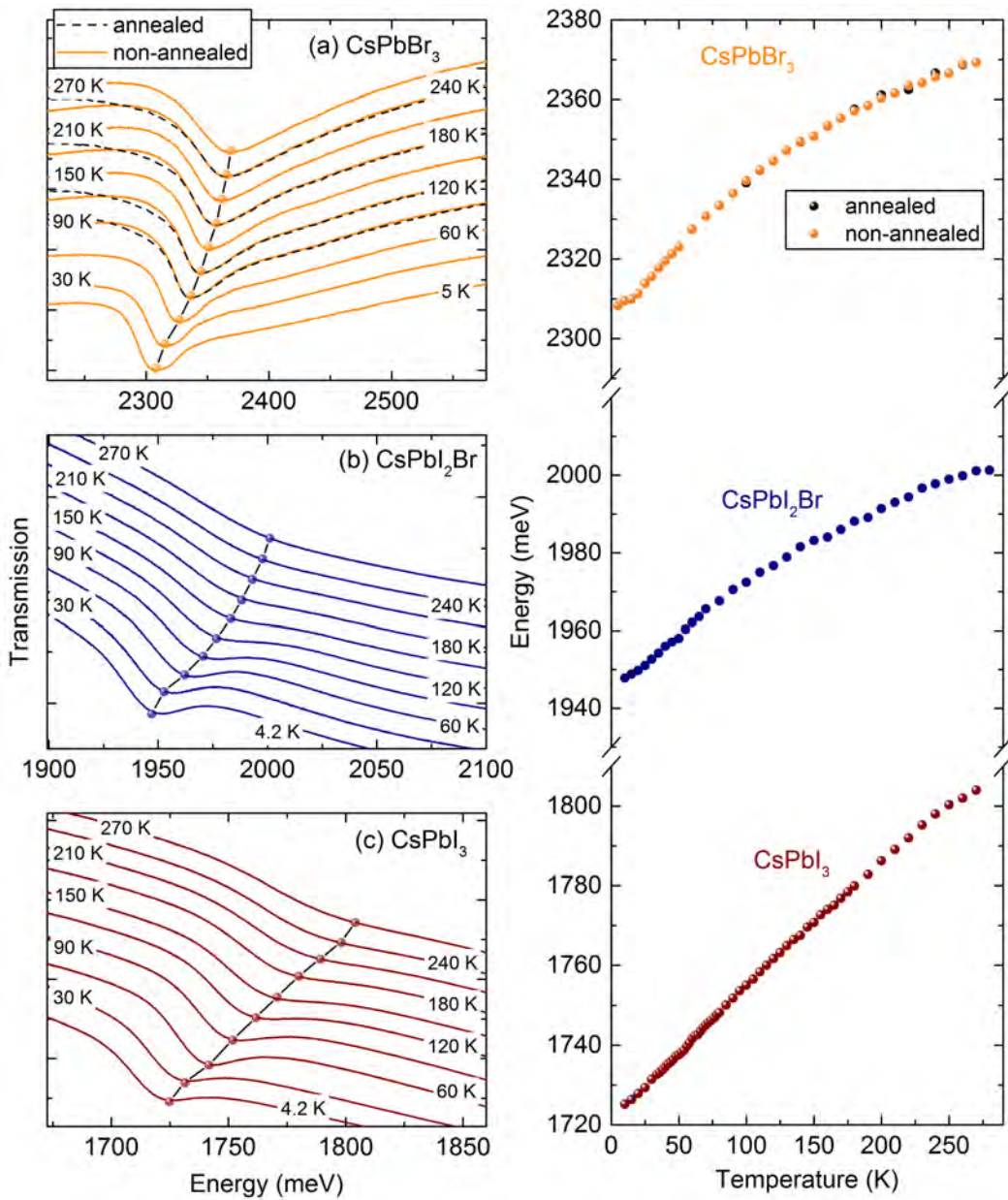


Figure 6.2: (a)-(c) Typical transmission spectra measured at different temperatures for CsPbBr_3 , CsPbBrI_2 and CsPbI_3 , respectively and (d) the energies corresponding to the observed transitions plotted as the function of temperature. The author acknowledges the participation of Yang Zhuo in obtaining the data for CsPbBr_3 .

in the case of the organo-lead tri-bromides (Fig. 3.7 (c) and (d)) suggests a strongly excitonic character of the photocreated carriers even at the room temperature.

6.3 Low-temperature magneto - transmission

To determine the exciton binding energies and reduced masses we applied analogous measurement techniques and analysis methods as previously used for the studies of the organic-inorganic compounds (Chapter 4). Typical magneto-transmission spectra measured at $T = 2$ K are shown in Fig. 6.3 for CsPbI_3 , CsPbI_2Br and CsPbBr_3 . The left column (panels (a),(c) and (e)) presents the raw transmission spectra at different values of magnetic field. Similarly as in the organic-inorganic compounds, when magnetic field is increased, we observe a blue-shift of the 1s transition with the appearance of weaker minima corresponding to the higher transitions. In order to more precisely determine their energies, we analyze the magnetic field spectra ratioed by the spectrum acquired at 0 T, presented in Fig. 6.3 (b),(d) and (f). For the CsPbI_3 , at 65 T we detect up to 5 transitions, including the crucial 2s state absorption. This weak minimum appears at the right top of the differential feature, resulting from the ratioing in the region of the 1s absorption (inset in Fig. 6.3 (b)). In agreement with the hybrid FAPbBr_3 bromide, where three excitonic transitions were observed in the long pulse, the number of minima detected for CsPbBr_3 is also reduced to three, which suggest a higher value of the exciton binding energy. In this compound, the 2s absorption is particularly well resolved. In contrast, only two transitions are observed for the CsPbI_2Br mixed halide, with no trace of the absorption minimum corresponding to the 2s state. This can be explained by the lower optical quality of this sample, revealed in the relatively weak minimum of the 1s transition. Such a problem may indicate either worsened morphology reported in the mixed halide perovskite compounds, or a need for further optimization of the annealing procedure.

To extract the effective Rydberg constant R^* and reduced mass μ , we plot the absorption energies as the function of magnetic field and describe particular transitions within the terms of the hydrogen-like atom or free carrier models. The results of such analysis, obtained for all three investigated compounds, are shown in Fig. 6.4. The blue spheres correspond to the long-pulse experimental data points. We support our analysis with the short pulse, extreme magnetic field data, measured by A. Miyata with the Mega Gauss installation, and marked with the black stars. The orange curves and gray lines are the transition energies for the excitonic states and Landau levels, respectively.

The number of the Mega Gauss data points for CsPbI_3 (Fig. 6.4 (a)) is limited to only three. This originates from the lifetime of the material in the cubic phase, shorter than the duration of the sample installation procedure, which is performed in the air. Despite this problem, five transitions observed in the long pulse measurement allow a satisfying fit for both models, which enables us to determine the values of $R^* = 15$ meV and $\mu = 0.115m_0$. The situation is reversed for the CsPbI_2Br mixed halide (Fig. 6.4 (b)); the longer lifetime of the cubic phase in air allows the collection of the numerous short-pulse data points. Their lowered slopes suggest considerably higher value of the reduced mass, $\mu = 0.126m_0$. The relatively low number of the long pulse data, with no observable trace of the 2s transition, limits

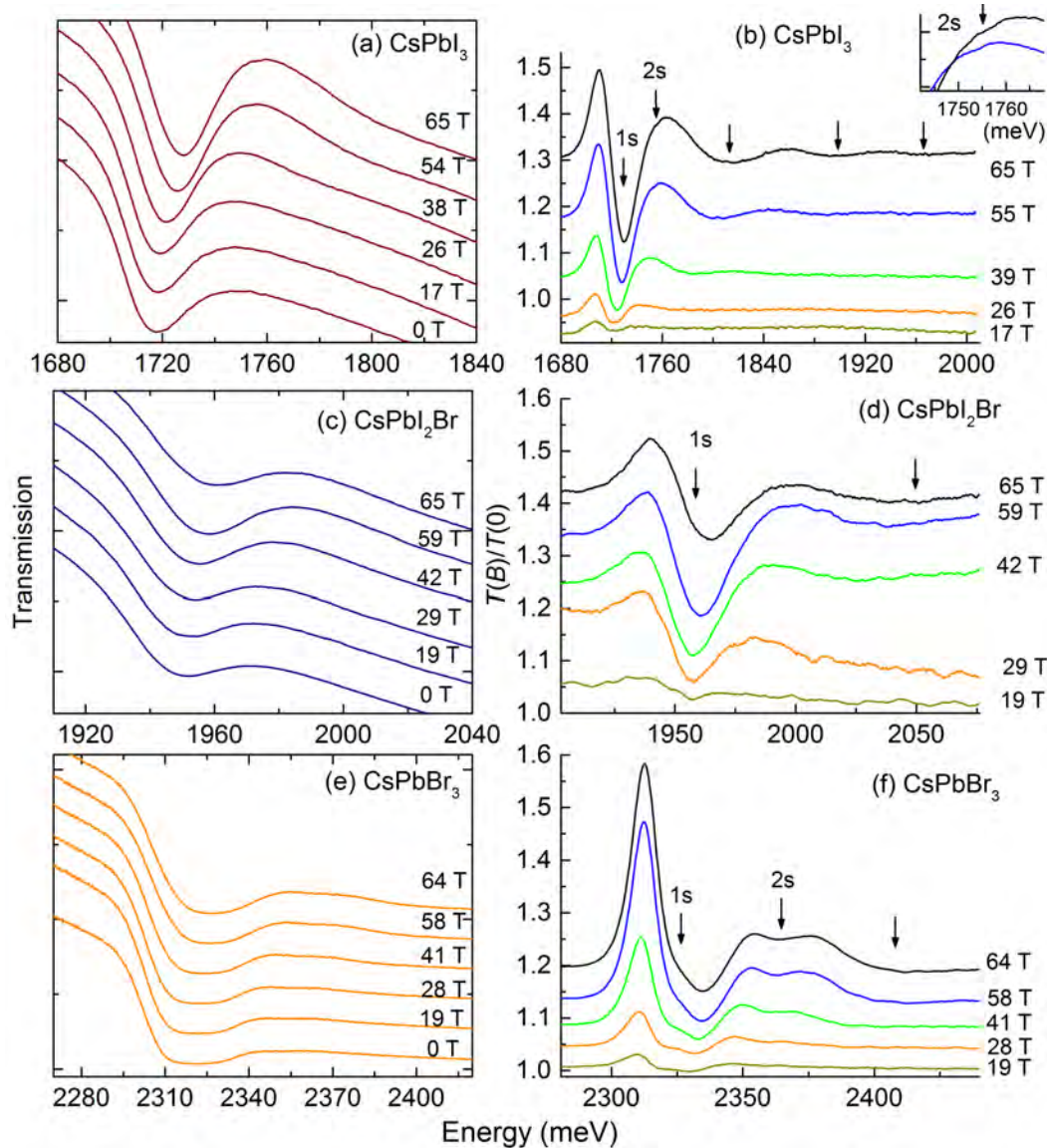


Figure 6.3: (a),(c),(e): Typical low temperature transmission data taken using a long pulse technique for CsPbI_3 , CsPbI_2Br and CsPbBr_3 , respectively. (b),(d),(f): The spectra in magnetic field divided by the spectrum acquired at 0 T.

the precision of extracting the effective Rydberg constant. We obtain the best fit for $R^* = 15 \text{ meV}$, which is the same value as for the pure tri-iodide. In the case of the wide-bandgap CsPbBr_3 (Fig. 6.4 (c)) both long and short pulse data sets are complete, resulting in a good accuracy of the derived electronic parameters. The exciton binding energy is as high as $R^* = 30 \text{ meV}$. If this value remains unchanged up to the room temperature, then a substantial fraction of the photocreated electron-hole pairs is bound as the excitons. This is suggested by the well developed absorption

minima observed in our temperature-dependence characterization studies. On the other hand, the reduced mass $\mu = 0.127 m_0$ is only slightly higher than the result obtained for CsPbI_2Br .

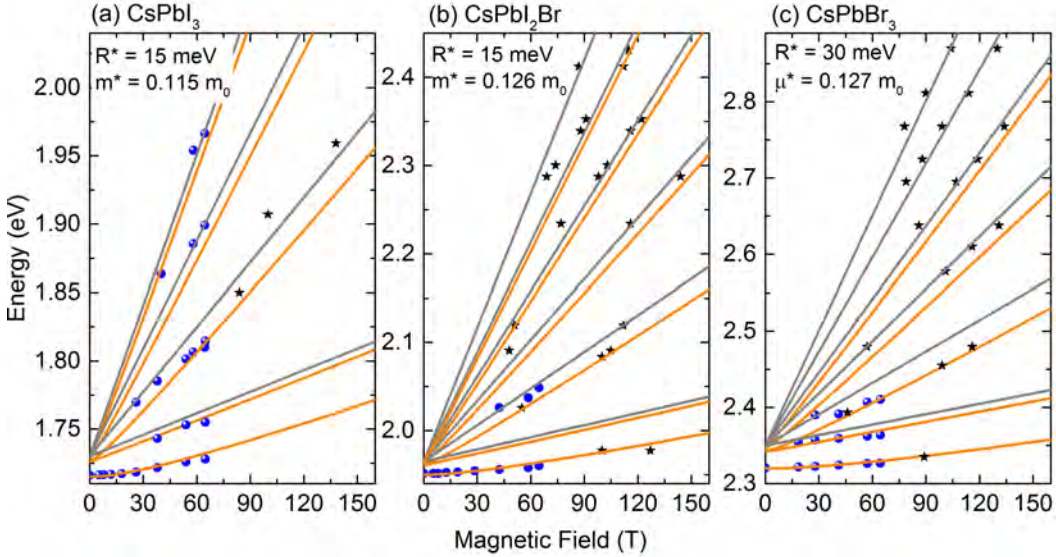


Figure 6.4: (a)(c) Transition energies obtained from the experimental data and results of the fit to the data for CsPbI_3 , CsPbI_2Br and CsPbBr_3 , respectively. The stars are the data obtained during the short pulsed measurements. The results of the theoretical fit are shown by grey and orange lines. Grey lines correspond to the interband transitions between Landau levels in the valence and conduction bands. The orange lines represent the energy levels of the hydrogenlike exciton.

Compound	Phase	E_g (meV)	R^* (meV)	μ (m_e)	ε_{eff}
CsPbI_3	cubic	1730	15 ± 1	0.115 ± 0.02	10.0
CsPbI_2Br	cubic	1965	15 ± 3	0.126 ± 0.01	10.7
CsPbBr_3	orthorhombic	2350	30 ± 3	0.127 ± 0.01	7.6

Table 6.1: The parameters of the fit of the full Landau fan chart for caesium-based compounds at $T = 2$ K.

6.4 Discussion

The results of the full fits for all three compounds are summarized in Table 6.1, where we also calculate the effective dielectric constant ε_{eff} , using Equation 1.6. Further

in Fig. 6.5, we compare these low-temperature parameters for Caesium-based compounds (color stars) with corresponding results for the hybrid organic-inorganic materials from Fig. 4.12 (blue spheres). Also for the fully inorganic compounds, the values of R^* and μ increase with the band gap energy, in a close agreement with the linear fits obtained for the hybrid perovskites. From this similarity we conclude that at low temperatures, when the organic cations are ordered, the qualitative picture of the interactions within the lattice is almost the same for both the inorganic and hybrid compounds. We plan to determine if a more pronounced difference occurs at higher temperatures, corresponding to the tetragonal phase range in the hybrid compounds, when the libration modes of the organic lattice are allowed. This will be investigated with our upcoming magneto-transmission measurements on the CsPbX_3 materials at ≈ 170 K. Moreover, we expect that with the new samples of improved optical quality and a reduced preparation time for the short pulse experiment, we will be able to determine the values of R^* and μ for the iodine-rich compounds more precisely. In particular, it is important to confirm, if the partial substitution of the Iodine with Bromine in 2:1 ratio indeed leads to an increase of the reduced mass by more than 10%, while the exciton binding energy remains unaffected.

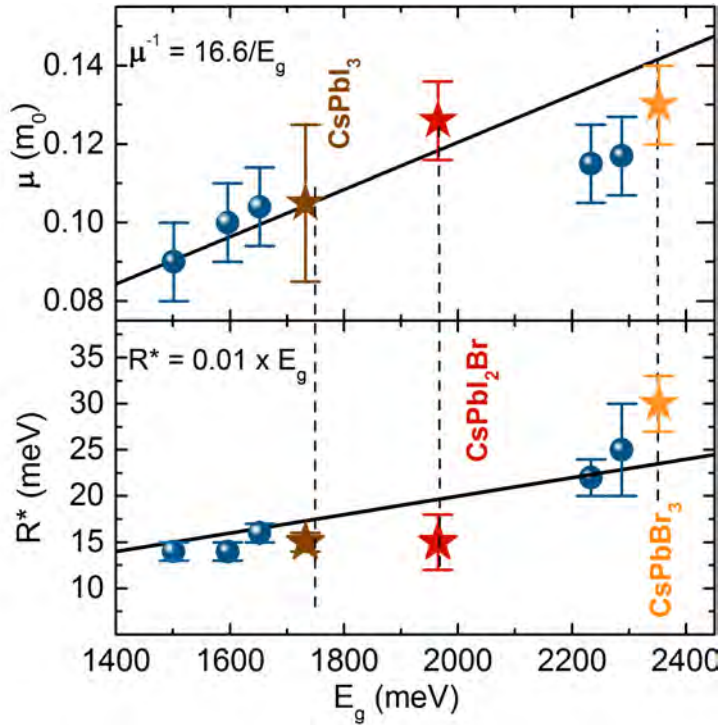


Figure 6.5: (a) Reduced mass and (b) binding energy at $T = 2$ K as a function of the energy gap respectively. The color stars are results for the fully inorganic CsPbX_3 compounds, presented in Table 6.1. The blue spheres are the low temperature results for the hybrid compounds, included in Table 4.1. The black solid lines show a linear fit to the data for the hybrid compounds.

CHAPTER 7

Conclusions

The organo - lead halide perovskites are promising candidates for light absorbers in a new generation of low-cost, high efficiency solar cells and high-performance light emitting devices. Recently, it has been demonstrated that the solar cells based on the multiple-cation hybrid perovskites can achieve photon conversion efficiencies up to 22% and are stable under the operational conditions. This indicates that the future of perovskite - based photovoltaics is determined by the development of new alloyed compounds. Therefore, further optimization of performance of these materials requires an advanced control of both electronic properties and morphology, originating from an understanding how these parameters change with chemical composition. In this thesis, we use optical methods to investigate basic electronic parameters, namely the exciton binding energy and reduced mass, as well as the morphology in several representatives of organo-lead halide perovskites. By studying compounds based on the Methylammonium or Formamidinium organic cations and different halides, we determine how these parameters are influenced by the type of accommodated ions.

Prior to the measurements in a magnetic field, we characterize our samples using temperature dependent macro-transmission. These studies, performed at temperatures ranging from 4 to 300 K, allow us to follow the changes of the band gap energy with the increase of the temperature. In particular, we analyze the development of the structural transition from the orthorhombic to tetragonal phase, occurring at around 160 K. We conclude that conversion to the tetragonal phase always leads to a drop in the band gap energy, in the range of 15 – 90 meV for different compounds. Another difference is the temperature range for which the phase transition progresses, varying from 15 K to 50 K. This is an indication that the phase transition is not uniform within the film; precisely, particular crystalline grains encounter the phase transition at different temperatures.

Further, we investigate the values of the exciton binding energy and reduced mass performing magneto-transmission in long-pulse high magnetic fields up to 67 T. Additionally, we support our analysis with the data points obtained from the short-pulse Mega Gauss experiment in the fields up to 150 T (in cooperation with A. Myiata, LNCMI). We analyze the magnetic field evolution of energies of the interband transitions between the excitonic and free-carrier states. We extract R^* and μ by fitting particular transitions with the hydrogen - like atom model in magnetic field (excitonic states) and Landau levels (free carrier states). This direct method enables an accuracy of derived parameters surpassing previously reported results, obtained by indirect measurements. We find general relations for the exciton

binding energy R^* and the reduced mass μ , which are principally determined by the band gap E_g for the whole family of hybrid perovskites. With the approximated values of $R^* = 0.01 \times E_g$ and $\frac{\mu}{m_0} = \frac{E_g}{16.6}$, basic electronic properties can be easily estimated for newly synthesized compounds. There is no evidence for a significant influence of organic cation type other than resulting from the changes in the band gap. This suggests that simple two band $\mathbf{k}\cdot\mathbf{p}$ perturbation theory should enable the accurate modeling of the properties of devices made from hybrid perovskites. We also demonstrate that the low temperature values of the exciton binding energies are smaller or comparable to the thermal energy at 300 K which makes a significant contribution to understanding the excellent performance of these devices in photovoltaic applications. For the tri-iodides, these values are further reduced in the high temperature phases of these materials. This is in agreement with the contribution of librations of the dipolar organic cations to the dielectric screening, suggested earlier in the literature for high temperature crystal structures. Remarkably, this phenomenon is not observed in the tri-bromide, characterized by a wider bandgap. The possible explanation is that the exciton binding energy in this compound, significantly larger than the energy of phonons corresponding to the librations of organic cations, is presumably too high to be effectively reduced by the cation - related phenomena.

In order to confirm the role of the organic cations in reducing the exciton binding energy at higher temperatures, we are currently performing the magnetooptical studies of fully inorganic, caesium-based compounds. Our preliminary result were obtained at low temperatures, at which the movements of organic lattice are quenched. In such conditions, the picture of electron-hole interactions is very similar for both hybrid and inorganic families of perovskite compounds.

Finally, we perform temperature-dependent spatially resolved micro - photoluminescence. The resulting maps show that perovskite thin films are composed from the dark and bright crystalline grains, which are around few micrometer in size, and up to $20 \mu\text{m}$ in the case of the mixed halide $\text{MAPbCl}_x\text{I}_{3-x}$. We demonstrate that the low temperature phase transition from tetragonal to orthorhombic phase is incomplete in all studied materials, as the remains of the tetragonal phase are found even at $T = 4 \text{ K}$. This is most evident in the FAPbBr_3 , where macroscopic domains of the tetragonal phase, spreading over hundreds of adjacent grains, are observed. In other compounds, the area of tetragonal inclusions is limited to the size of single crystalline grains. These inclusions can be even smaller, as due to the long carrier diffusion lengths reported for the perovskites, the lower band gap tetragonal material can preferably collect the carriers over large regions, which gives a rise to a relatively strong PL peak corresponding to the tetragonal phase. By investigating structurally damaged and photo annealed regions, where the occurrence of the tetragonal phase at low temperatures is enhanced, we attribute its presence to the depleted halide content. Therefore, the spatially resolved photoluminescence performed at low temperatures enables to detect meager inhomogeneities within the perovskite films, which are not observable at the room temperature.

APPENDIX A

Publications

PUBLICATIONS BASED ON THE RESULTS OF THIS THESIS:

1. **K. Galkowski**, A. A. Mitioglu, A. Surrente, Z. Yang, D. K. Maude, G. E. Eperon, J. T-W. Wang, H. J. Snaith, P. Plochocka and R. J. Nicholas
“Spatially resolved studies of the phases and morphology of methylammonium and formamidinium lead tri-halide perovskites”
Submitted to NanoLetters
2. **K. Galkowski**, A. A. Mitioglu, A. Miyata, P. Plochocka, O. Portugall, G. E. Eperon, J. T-W. Wang, T. Stergiopoulos, S. D. Stranks, H. J. Snaith R. J. Nicholas
“Determination of the exciton binding energy and effective masses for methylammonium and formamidinium lead tri-halide perovskite semiconductors”
Energy and Environmental Science **9(3)**, 962-970 (2016)

OTHER PUBLICATIONS:

1. A. Osherov, E. M. Hutter, **K. Galkowski**, R. Brenes, D. K. Maude, R. J. Nicholas, P. Plochocka, V. Bulovic, T. J. Savenije and S.D. Stranks
“The Impact of Phase Retention on the Structural and Optoelectronic Properties of Metal Halide Perovskites”
Advanced Materials, available online, (2016)
2. A. Surrente, A. A. Mitioglu, **K. Galkowski**, L. Klopotowski, W Tabis, B. Vignolle, D. K. Maude and P. Plochocka
“Onset of exciton-exciton annihilation in single layer black phosphorus”
Physical Review B **94(7)**, 075425 (2016)
3. A. A. Mitioglu, **K. Galkowski**, A. Surrente, L. Klopotowski, D. O. Dumcenco, A. Kis, D. K. Maude and P. Plochocka
“Magnetoexcitons in large area CVD-grown monolayer MoS₂ and MoSe₂ on sapphire”
Physical Review B **93(16)**, 164412 (2015)
4. A. Surrente, A. A. Mitioglu, **K. Galkowski**, W Tabis, D. K. Maude and P. Plochocka
“Excitons in atomically thin black phosphorus”
Physical Review B **93(12)**, 121405 (2015)

5. **K. Galkowski** P. Wojnar, E. Janik, J. Papierska, K. Sawicki, P. Kossacki and J. Suffczynski
"Exciton dynamics in individual semimagnetic (Zn,Mn)Te/(Zn,Mg)Te nanowires"
Journal of Applied Physics **118**, 095704 (2015)
6. K. Sawicki, F. K. Malinowski, K. Galkowski, T. Jakubczyk, P. Kossacki, W. Pacuski and J. Suffczynski
"Single-color, in situ photolithography marking of individual CdTe/ZnTe quantum dots"
Applied Physics letters **106(1)**, 012101 (2015)
7. A. Derkachova, K. P. Korona, J. Binder, **K. Galkowski**, L. Wachnicki, M. Godlewski, T. Dietl and J. Suffczynski
"Modification of Emission Properties of ZnO Layers due to Plasmonic Near-Field Coupling to Ag Nanoislands"
Plasmonics **8**, 913-919 (2013)

APPENDIX B

Résumé de la thèse en français

Dans cette annexe, nous présentons un résumé en français de ce travail de thèse. Le lecteur ne trouvera aucune nouvelle information et les figures utilisées sont les mêmes que dans la version anglaise.

B.1 Introduction

Le premier chapitre introduit la physique de base des excitons de Wannier-Mott exciton et résume l'état actuel des connaissances sur les pérovskites hybrides.

Les pérovskites hybrides organiques-halogénure de plomb représentent une classe de matériaux émergents, proposés comme absorbeurs de lumière dans le cadre des cellules solaires de troisième génération. La formule chimique de ces composés est ABX₃, où A est un cation organique, X représente un anion halogénure (normalement Cl-, Br-, ou I-, ou bien, un alliage composé par ces éléments). La structure pérovskite, dans sa forme cubique la plus simple, est schématiquement représentée sur la Figure B.1.

Les pérovskites hybrides combinent d'excellentes propriétés d'absorption avec une grande longueur de diffusion des porteurs de charge ainsi de longues durée de vie, ce qui permet d'atteindre des efficacités de conversion de photons de 22%. Un autre avantage est leur bas cout de fabrication. Par conséquent, avec le développement de cette classe de matériaux, le photovoltaïque basé sur les pérovskites peut potentiellement améliorer fortement les performances des technologies actuelles, basée sur le silicium.

Les objectifs de ce travail sont, d'une part, d'étudier les propriétés électroniques de base de pérovskites hybrides, ainsi que leur morphologie.

B.2 Techniques expérimentales

Le deuxième chapitre décrit les techniques expérimentales qui ont été utilisées pour étudier les propriétés de pérovskites hybrides. Deux types des techniques sont utilisés. D'une part, la spectromètre d'absorption optique inter-bande en champs magnétiques intenses a été utilisée pour obtenir les résultats présentés dans les chapitres A4 et A6. D'autre part, la micro photoluminescence(μ PL) a été utilisée pour étudier la morphologie des couches minces de plusieurs types de pérovskites (chapitre A5).

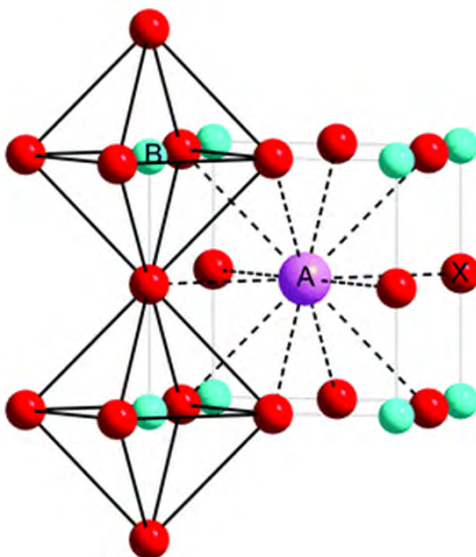


Figure B.1: La structure cubique idéale des pérovskites: BX_6 occupe le sommet des octaèdres (B = blue sphères bleues, X = sphères rouges) et le cation A (sphere violette) occupe centre de la maille unitaire avec une coordinence cuboctaèdrale (12). D'après [Johnsson 2007].

B.3 La description et caractérisation des échantillons

Les études présentées dans cet ouvrage ont été réalisés sur plusieurs représentants de la famille de perovskite hybride. Nous étudions le composés à base de Methylammonium ($\text{MA} = \text{CH}_2\text{NH}_3^+$) ou Formamidinium ($\text{FA} = \text{CH}(\text{NH}_2)_2^+$) cations organique. Tous les échantillons ont été fabriqués dans le groupe du Henry Snaith dans Clarendon Laboratory, University of Oxford.

Les échantillons étudiés dans cette these sont des films minces de la un matériau perovskite déposé sur des substrats en verre. Les films sont environ 350 nm d'épaisseur, ce qui est comparable à la profondeur de pénétration la lumière visible [Stranks 2013]. L'épaisseur est uniforme à travers l'échantillon, et le matériau est exempt de les défauts de trous d'épingles analogues. L'épaisseur du substrat est 1 mm. Fig B.2 présent la photographie de trois échantillons de formamidinium base typiques utilisés pour notre recherche. la différences dans le contenu halogénure - changent d'iode pur est brome pur - sont responsables de la variation observée de la couleur. Tout film mince perovskite ont été synthétisées à partir d'une solution, en utilisant méthodes de revêtement par centrifugation.

Afin d'assurer le code que le film est une enquête perovskite conservés dans la phase de perovskite, en minimiser l'influence de la l'humidité et de température pendant la période de stockage. Les échantillons, Quels sont scellés sous vide pour le transport, sont placés dans un vide box Immédiatement après l'arrivée. Les



Figure B.2: Photographies d'un échantillon typique a base de Formamidinium

échantillons sont stockés sous une pression $\approx 10^{-5}$ bar et un ambient temperature de 18° C. Les films perovskite sont exposée a l'atmosphère que pendant la préparation de la expérience, qui ne dure pas plus de 30 minutes. Nous analysons également les échantillons pour les premiers symptômes de la désintégration avant de la la mesure. Une preuve visible de la dégradation de l'échantillon est la présence des chefs de file de di-halogénures est dans les couleurs observées: jaune pour PbI₂ et blanche pour PbBr₂.

Pour la caractérisation initiale des échantillons, dans la mesure l'énergie de l'absorption proche d'intervalle de bande en fonction de la température. Dans ces études sur l'utilisation de la large bande macro-transmission, réalisée en l'absence de champ magnétique. la Les spectres de transmission typique acquis a différentes températures pour l'archétype MAPbI₃ are dominated by a single notre magnéto - études de transmission montrent que cette absorption correspond a la transition excitonique 1s. Nous extrayons la les énergies d'absorption du spectre de transmission en recherchant la centre de la forme d'absorption. Ces énergies sont représentées graphiquement en tant que fonction de la température dans Fig. B.3 (b). L'augmentation de la température, nous observons le bleu-shift et l'élargissement de la résonance d'absorption. Le coefficient de température positif de la largeur de bande interdite est caractéristique pour tous les pérovskites hybrides.

Au-dessus de 145 K, nous trouvons la premiere preuve de la transition de phase développement dans le MAPbI₃ film. A 169 K La conversion est complete, car nous ne détectons que l'absorption correspondant a la phase tétragonale. Augmenter la température au-dessus 169 K, nous observons a nouveau une augmentation constante de l'énergie d'absorption et elargissement de sa forme. Des mesures de caractérisation ont été effectuées pour tous les composés étudiés.Nous pouvons comparer en détail le développement de la transition de phase dans Tous les matériaux étudiés en analysant leur absorption Énergies représentées en fonction de la température. Ils sont résumés dans Fig. B.4.

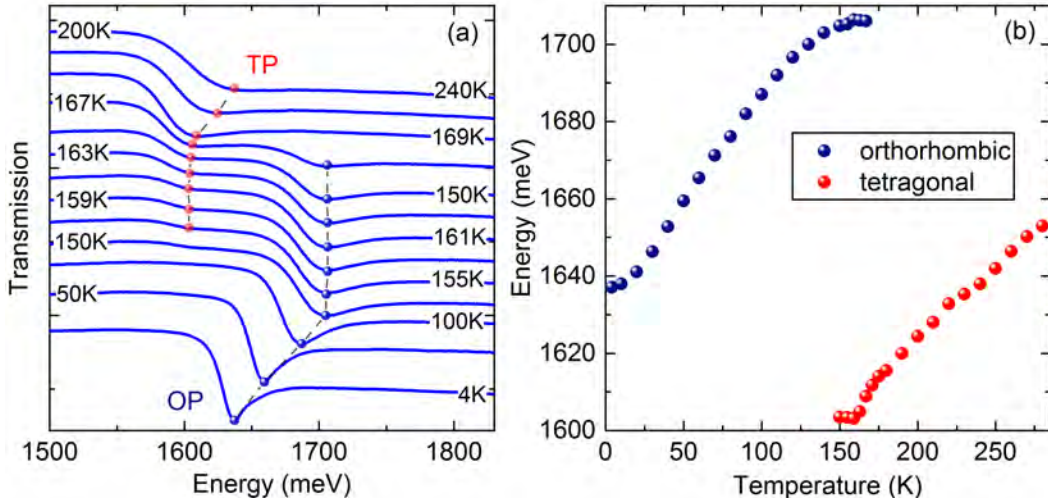


Figure B.3: (a) Spectre de transmission typique pour MAPbI₃ mesuré à différentes températures (b) Energies des transitions observées en fonction de la température. Les points et les tirets ont été ajoutés pour suivre les transitions

B.4 Magnéto-transmission

Le chapitre 4 décrit des études de magnéto-photoluminescence, fournissant des informations sur les paramètres électroniques de base - l'énergie de liaison de l'excitons et la masse réduite. Il introduit également l'influence du champ magnétique sur les transitions optiques.

Les paramètres électroniques de base des pérovskites organiques-inorganiques, comme l'énergie de liaison de l'exciton R^* et la masse réduite μ , ont fait l'objet d'un débat intense dans la littérature. Les images des porteurs soit liés, soit complètement ionisés dans les composés de pérovskite à base d'iode ont été proposées en se fondant sur diverses méthodes expérimentales indirectes. Alors que l'énergie thermique moyenne à la température ambiante est $k_B T \simeq 26$ meV, des valeurs de R^* dans la gamme de 2 – 50 meV ont été reportées. En 2015, Miyata *et al.*, en utilisant des mesures de magnéto-transmission, a démontré que l'énergie de liaison de l'exciton dans le composé photovoltaïque archétypal de la pérovskite MAPbI₃ se trouve à l'extrême inférieure de cette gamme [Miyata 2015].

Dans ce travail, nous étendons les études de magnéto-transmission sur des pérovskites organiques-inorganiques à d'autres matériaux de cette famille nouvellement synthétisés. Dans tous les composés étudiés, les énergies de liaison des excitons sont inférieures ou comparables à l'énergie thermique moyenne à température ambiante. Nous constatons aussi que l'énergie de liaison de l'exciton ainsi que la masse réduite augmentent proportionnellement à l'énergie de la bande interdite. Les valeurs de la masse réduite sont cohérentes avec une approche de perturbation $\mathbf{k} \cdot \mathbf{p}$ à deux bandes simples pour la structure de bande. Ces conclusions peuvent être généralisées

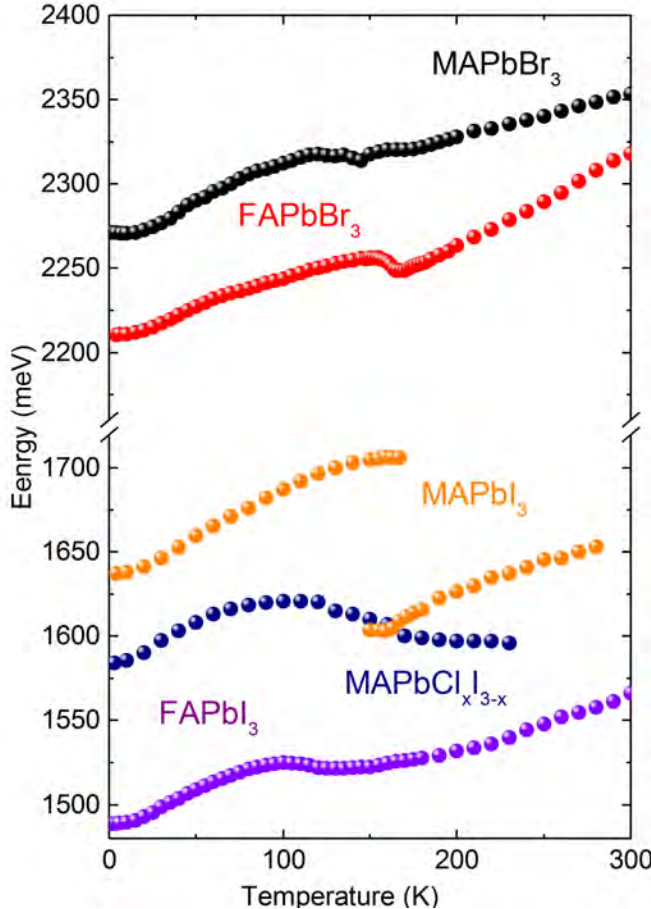


Figure B.4: Les énergies d'absorption des bords proches de la bande en fonction de température pour tous les matériaux étudiés.

pour prédire les valeurs de la masse réduite et de l'énergie de liaison pour les autres membres de la famille des pérovskites hybrides.

Nous avons mesuré les spectres de transmission à large bande en utilisant une lampe halogène blanche, dans de l'hélium liquide pompé ($T \simeq 2$ K) sous champs magnétiques allant jusqu'à 70 T, en observant de multiples transitions optiques pour chaque composé. Les résultats de transmission typiques obtenus pour les composés à base d'iodine, à savoir $\text{MAPbCl}_x\text{I}_{3-x}$ et FAPbI_3 sont présentés sur la Fig. B.5. Cette expérience a été effectuée en utilisant de l'optique de polarisation, et les courbes bleues et rouges correspondent respectivement aux polarisations circulaires σ^- and σ^+ . Les spectres présentés sur les figures (a) et (c) montrent un minimum bien marqué à environ 1.58 eV et 1.49 eV respectivement. Ces absorptions correspondent à l'état 1s de l'exciton neutre. Dans le cas de $\text{MAPbCl}_x\text{I}_{3-x}$, un second minimum plus faible à environ 1.6 eV apparaît dans les champs au-dessus de 20 T. Cette transition est attribuée aux états 2s. Les absorptions 1s et 2s révèlent une séparation

de Zeeman claire.

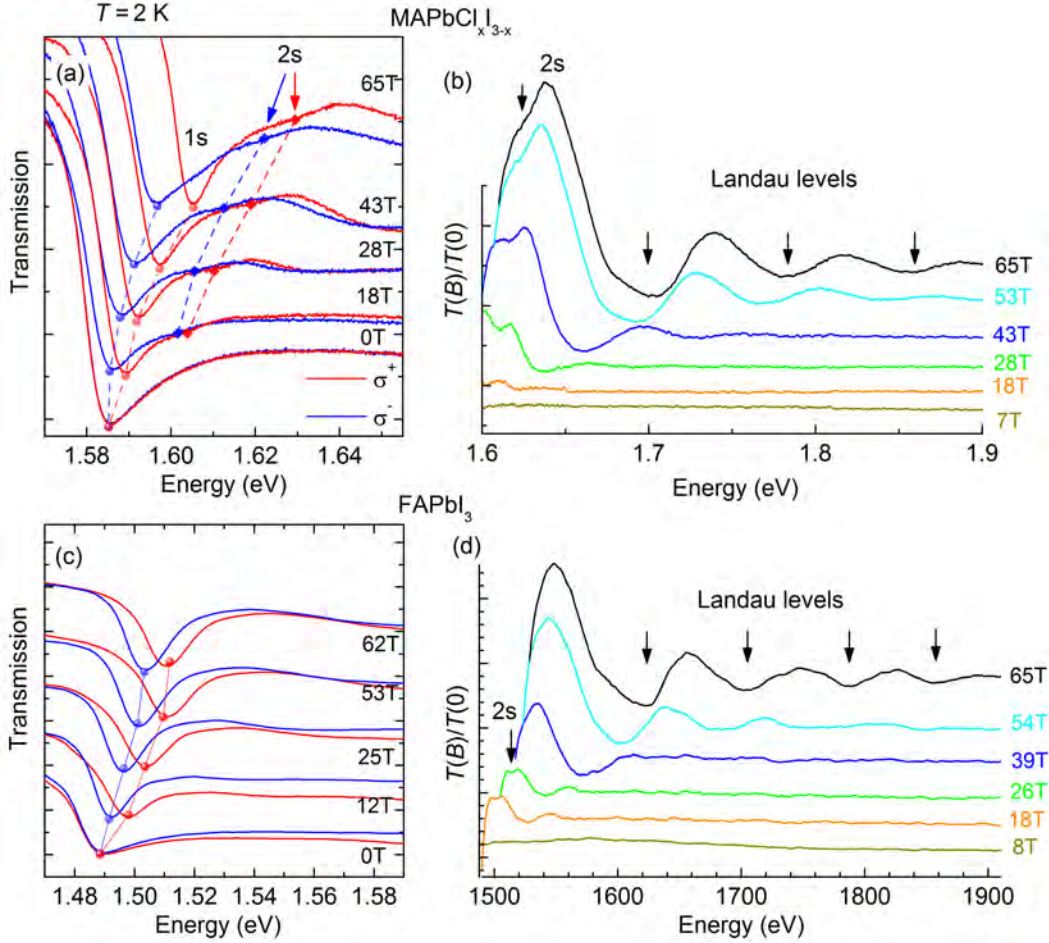


Figure B.5: (a),(c): données typiques de transmission à basse température $\text{MAPbCl}_{x}\text{I}_{3-x}$ et FAPbI_3 obtenues en utilisant la technique de pulse long. Les lignes rouges et bleues correspondent à deux lumières polarisées respectivement σ^+ et σ^- . Les points bleus/rouges et les lignes en pointillés sont ajoutées afin de faciliter le suivi des transitions 1s et 2s. (b), (d): Les spectres à différents champs magnétiques divisés par le spectre acquis à 0 T.

Nous étendons les mesures dans la gamme spectrale de la lumière visible, où nous traçons pour l'analyse les spectres en champ magnétique divisés par le spectre pris à zéro champ, comme indiqué dans la Fig. B.5, (b) et (d). Ces données ne sont pas résolues en polarisation. La première caractéristique spectrale à basse énergie visible dans les figures (b) et (d) est le résultat de la division du signal sur la région de l'état 1s décalé magnétiquement. Selon cette caractéristique différentielle, nous observons les minima correspondant à l'état 2s également dans FAPbI_3 . Des études complémentaires à basse température, sur les bandes interdites supérieures (2.2-

2.3 eV) représentatives des pérovskites organiques-inorganiques, ont été effectuées sur des tri-bromures, à savoir FAPbBr_3 et MAPbBr_3 . Pour cette gamme d'énergie, nous effectuons les mesures sans résoudre la polarisation circulaire.

Les spectres de transmission pour chaque valeur du champ magnétique sont analysés afin de trouver les énergies des minimums d'absorption particuliers. Nous effectuons ces analyses en recherchant le centre de la géométrie d'absorption, en supposant une symétrie de type gaussien. Des données supplémentaires prises en champs jusqu'à 150 T sont fournies par la technique expérimentale de MegaGauss, réalisée par A. Miyata au LNCMI. Dans le but d'extraire l'énergie de liaison et la masse réduite de l'exciton à partir des données de magnéto-transmission, nous analysons les transitions observées avec les modèles de la théorie des hydrogénées et celui des électrons libres. Comme la masse réduite est le seul paramètre d'ajustement pour les niveaux de Landau, les transitions à haute énergie et champ magnétique élevé constituent une forte contrainte pour la détermination de μ . Pour déterminer précisément l'énergie de liaison de l'exciton, l'observation simultanée des transitions 1s et 2s est primordiale. Les données recueillies et les ajustements correspondants sont résumés sur la Fig. B.6. Les deux paramètres R^* et μ dépendent de la bande interdite, augmentant au fur et à mesure que le gap augmente.

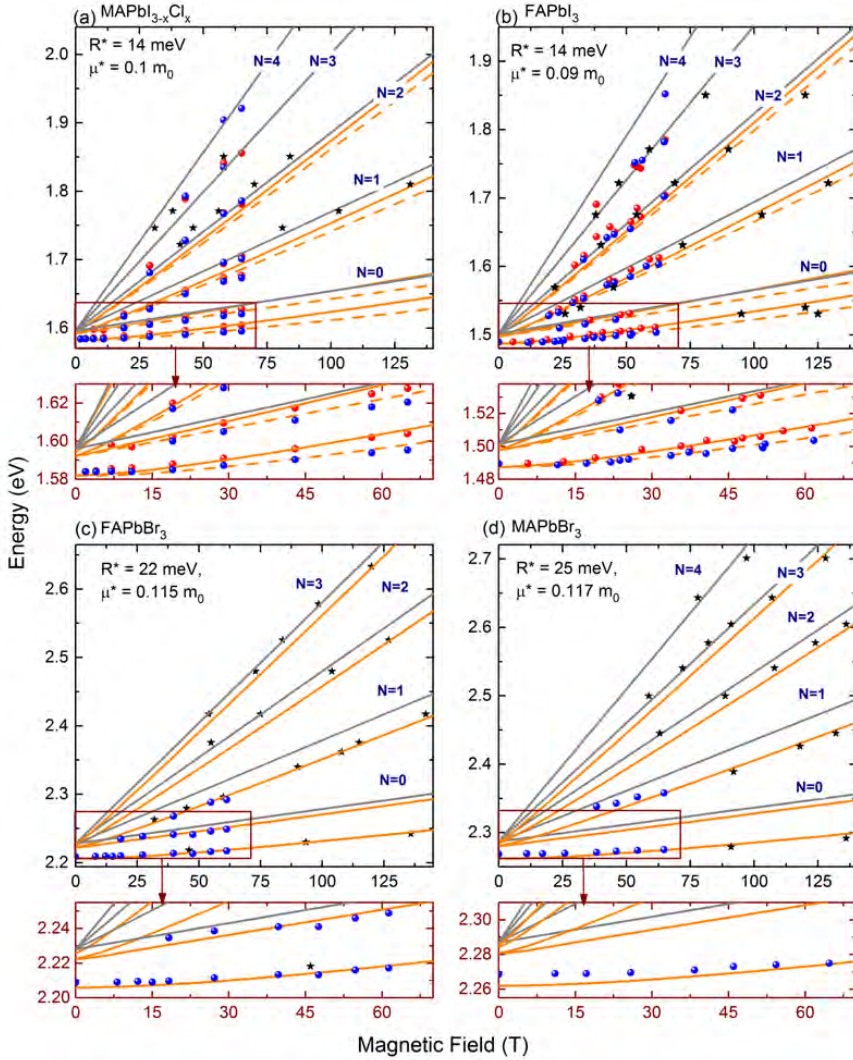


Figure B.6: (a)-(d) Les énergies de transition obtenues à partir des données expérimentales et des résultats de l'ajustement aux données pour $\text{MAPbCl}_x\text{I}_{3-x}$, FAPbI_3 , FAPbBr_3 et MAPbBr_3 , respectivement. Les points rouges et bleus correspondent aux minima résolus en polarisation dans l'absorption pour σ^+ et σ^- respectivement. Les étoiles sont les données obtenues lors de courtes mesures pulsées, où la polarisation n'a pas été utilisée. Les données prises en longs pulses ne sont pas non plus résolues en polarisation pour les échantillons FAPbBr_3 et MAPbBr_3 . Les résultats de l'ajustement théorique sont indiqués par les lignes grises et orange. Les lignes grises correspondent aux transitions interbandes entre les niveaux de Landau dans les bandes de valence et de conduction. Les lignes oranges montrent les niveaux fortement liés de l'exciton de type hydrogène. Dans (a) et (b), les transitions de séparation de Zeeman sont représentées par les lignes pleines et en pointillés. Au-dessous de chaque graphique, la partie bas champ et basse énergie du diagramme complet est agrandie.

Nous avons étendu les mesures de magnéto-transmission à des températures plus élevées, plus pertinentes pour les conditions opérationnelles d'un dispositif photovoltaïque. Nous avons effectué l'expérience juste au-dessus du point de transition de phase, autour de 150-160 K, où les pérovskites hybrides se transforment de la phase orthorhombique à basse température, à la phase tétragonale à haute température. De cette façon, nous étudions un matériau de paramètres du réseau très semblables aux paramètres révélés à température ambiante, alors qu'à $T \simeq 150$ K nous avons l'avantage considérable que les minima d'absorption sont remarquablement plus forts et mieux définis par rapport à $T \simeq 300$ K. Le résultat de la magnéto-transmission à haute température avec des ajustements correspondants est présenté sur la Fig. B.7

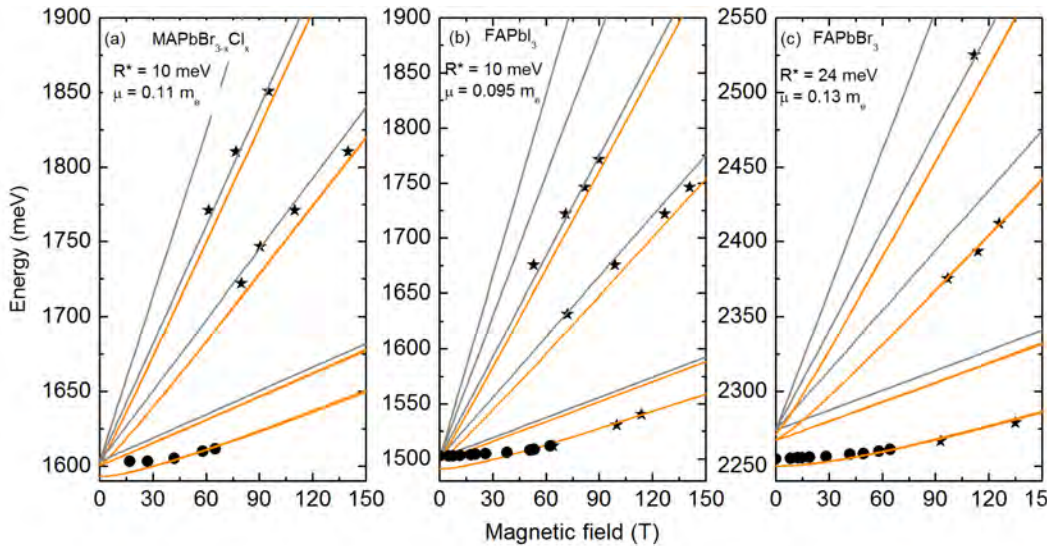


Figure B.7: (a)-(c) Les énergies de transition obtenues à partir des données expérimentales et des résultats de l'ajustement aux données pour $\text{MAPbCl}_{3-x}\text{Cl}_x$, FAPbI_3 et FAPbBr_3 , respectivement. Les étoiles sont les données obtenues lors des mesures de pulse court. Les résultats de l'ajustement théorique sont représentés par des lignes grises et oranges. Les lignes grises correspondent aux transitions interbandes entre les niveaux de Landau dans les bandes de valence et de conduction. Les lignes oranges représentent les niveaux d'énergie de l'exciton de type hydrogène.

Les valeurs de μ ont augmenté légèrement à $(0.095 - 0.13 \pm 0.01) m_0$. La plus forte augmentation est observée pour le tri-bromure, ce qui est en accord avec l'augmentation de la bande interdite par rapport à la valeur basse température. Dans les iodures, nous trouvons que les énergies de liaison des excitons sont réduites à la phase tétragonale à $R^* = 10 \pm 3$ meV, avec une augmentation correspondante de ϵ_{eff} . En revanche, pour FAPbBr_3 nous estimons $R^* = 24 \pm 4$ meV, ce qui est une valeur légèrement plus élevée que celle mesurée pour la phase orthorhombique basse température.

Les paramètres électroniques essentiels - la masse réduite μ et l'énergie de liaison de l'exciton R^* mesurées à la basse température, phase orthorhombe, sont tracées en fonction de la bande interdite du matériau dans le champ Fig. 4.12 (a). On constate que les deux paramètres augmentent faiblement avec la bande interdite.

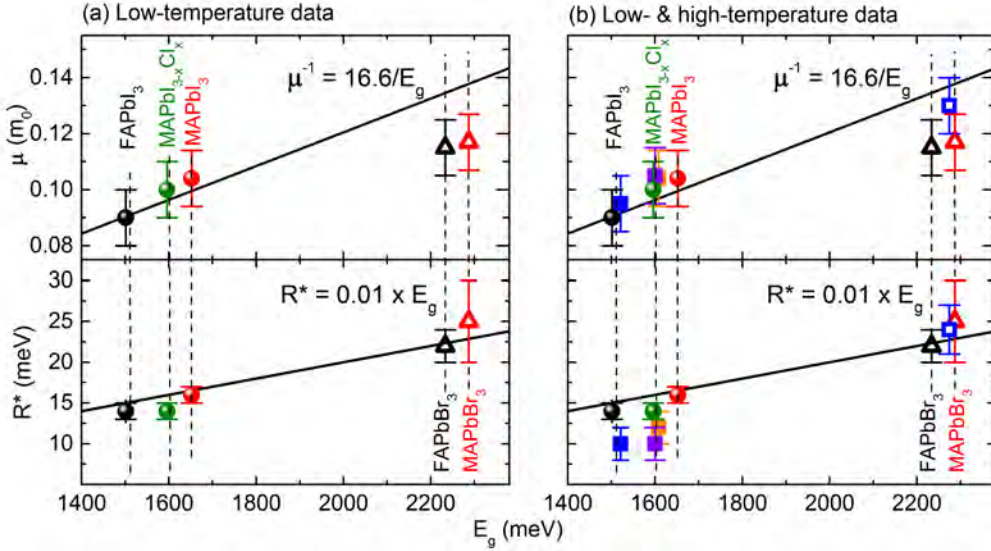


Figure B.8: (a) et (b) masse réduite et énergie de liaison à $T = 2$ K en fonction du gap d'énergie respectivement. Les symboles noirs (rouges) indiquent les résultats pour les iodures FA (MA) (symboles complets) et les bromures (symboles ouverts). Les cercles verts montrent des résultats pour l'halogénure mixte $MAPbI_{3-x}Cl_x$. Les lignes pleines noires montrent un ajustement linéaire aux données. (c) et (d) Le graphique des données à basse température ainsi que les valeurs déduites pour la phase tétragonale à température plus élevée (avec carrés) pour les matériaux FA (bleu), MA (orange) et mixte (violet), mesurées dans la gamme de températures données dans le tableau 4.2

Les valeurs de masse excitonique réduite dans les matériaux étudiés sont comprises entre 0.090 et 0.177 fois la masse de l'électron libre. Comme les pérovskites à l'halogénure d'organo-plomb sont caractérisées par une structure de bandes relativement simple, nous pouvons appliquer une approche Hamiltonienne semi-empirique à deux bandes $\mathbf{k} \cdot \mathbf{p}$ pour les calculs efficaces de masse [Even 2015]. La masse réduite μ sera :

$$\frac{1}{\mu} = \left| \frac{1}{m_e^*} \right| + \left| \frac{1}{m_h^*} \right| = \frac{4m_0|P|^2}{E_g}. \quad (\text{B.1})$$

Où $\frac{2(|P|^2)}{m_0}$ est l'énergie de Kane, déterminant la force des transitions optiques [Chuang 1995], avec

$$P = \langle \psi_{VB} | i\hbar \frac{\partial}{\partial x} | \psi_{CB} \rangle$$

étant l'élément de la matrice de la quantité de mouvement provenant du terme $\mathbf{k} \cdot \mathbf{p}$, c'est-à-dire du couplage des fonctions d'ondes électroniques dans les bandes de conduction et de valence. Un ajustement de l'équation B.1 aux données de basse température, présenté dans l'encadré supérieur de la Fig. B.8 (a), donne la valeur de l'énergie de Kane égale à 8.3 meV. Compte tenu de l'augmentation de μ d'environ 10%, l'estimation de l'énergie de Kane à température ambiante est d'environ 7.5 meV.

Fait remarquable, il n'existe aucune preuve solide d'un changement de la masse réduite lors de la substitution de Méthylammonium par des cations de Formamidinium. Nous n'observons que de petits changements dans la bande interdite, induits par les changements dans les paramètres du réseau, comme l'inclinaison des octaèdres suggérée par Amat et al. [Amat 2014].

La constante efficace de Rydberg se révèle être plus dépendante du matériau, variant avec la bande interdite de 14 à 25 meV approximativement comme:

$$R^* = 0.01 \times E_g.$$

Les valeurs mesurées sont en bon accord avec la valeur de 15 meV, déduite pour MAPbI₃ par Even et al. [Even 2014b]. La réduction de R^* dépendant de la température indique que les valeurs mesurées à $T = 2$ K sont la limite supérieure des énergies de liaison des excitons dans ces matériaux. Par conséquent, étant inférieures ou comparables à l'énergie thermique à température ambiante ($\simeq 25$ meV), nos résultats à basse température pour R^* suggèrent que dans toute la famille des pérovskites hybrides tri-halogénés, les porteurs photocréés sont espérés être thermiquement ionisés à 300 K. Cela explique en grande partie les excellentes efficacités des dispositifs pérovskites photovoltaïques.

Les valeurs de la constante diélectrique effective ϵ_{eff} se trouvent dans la gamme de 7.5 - 9.8, entre les valeurs de basse $\epsilon_0 = 25.7$ [Wehrenfennig 2014a] et haute $\epsilon_\infty = 5.6$ valeurs de fréquence [Umari 2014, Brivio 2014]. Une légère baisse de ϵ_{eff} est observée avec la montée de R^* et μ . Ce type de comportement est caractéristique pour les matériaux fortement polaires avec un fort couplage électron-phonon. Les valeurs de ϵ_{eff} sont significativement plus faibles pour les tri-bromures, où les masses réduites plus élevées font que l'énergie de liaison est plus grande, avec une réduction conséquente de la résistance d'écrantage.

La transition de phase semble avoir un impact limité sur la valeur de la masse réduite μ . Nos résultats indiquent qu'après la transition de phase, le μ peut augmenter jusqu'à 10 % par rapport aux valeurs obtenues 2 K. Nous concluons que toute la famille des pérovskites organo-halogénures de trihalogénures peut être décrite par l'équation 4.8 en termes de paramètre unique - l'énergie de bande interdite, quelle que soit la phase cristalline ou la température. La constante diélectrique effective ϵ_{eff} et par conséquent l'énergie de liaison exciton R^* sont plus affectées par la transformation de la phase orthorhombique, à la phase tétragonale. Ceci est lié à un mouvement de rotation collectif supplémentaire des cations organiques, autorisé à des températures plus élevées, et augmentant encore l'écrantage du potentiel Coulombien [Poglitsch 1987]. Nous trouvons que les valeurs de R^* pour les

matériaux à base d'iodure réduites à l'intervalle de 10 ± 3 meV, résultant d'une augmentation de ε_{eff} . En outre, le décalage diamagnétique observé pour l'état 1s est anormalement bas par rapport aux simulations (voir Fig. 4.11(a),(b)), ce qui peut être une preuve de l'augmentation dépendante en champ de l'énergie de liaison de l'exciton [Behnke 1978]. Par conséquent, la valeur en champ nul de R^* peut être encore plus petite, de l'ordre de 5 meV prédit par Even et al. [Even 2014b], ou moins.

B.5 Études de micro-photoluminescence résolues en temps de pérovskites d'halogénure d'organo-plomb

En raison de leur nature "spin-coated", les films minces de pérovskite ont une uniformité limitée [Chen 2014b, Zhou 2014, Eperon 2014b]. Les défauts de structure et les inclusions non stoechiométriques, formés lors de l'évaporation du solvant, peuvent influencer négativement la performance du dispositif. Cependant, à ce jour, il existe un nombre limité d'études sur l'impact de la morphologie de la couche mince de la pérovskite sur l'efficacité des cellules solaires. Seulement récemment, les inhomogénéités significatives de la pellicule mince de pérovskite, affectant leurs performances, ont été montrées [de Quilettes 2015]. La structure du film a révélé la présence de grains microcristallins de taille de l'ordre de quelques micromètres. On a constaté que l'intensité de la photoluminescence et la durée de vie du porteur dépendaient fortement de la position à travers le film, du fait de l'existence de grains foncés spécifiques. Ces grains foncés agissent comme des pièges non radiatifs pour les porteurs photo-créés, conduisant à une diminution de la performance globale des cellules solaires.

De plus, nos résultats de micro-photoluminescence dépendant de la température fournissent une indication forte pour le progrès non homogène de la transition de phase dans les films de pérovskite. Les spectres typiques obtenus à deux positions différentes de l'échantillon de $\text{MAPbCl}_x\text{I}_{3-x}$, mesurés en fonction de la température, sont représentés sur la Fig. B.9 (a) and (b). L'encadré (a) représente la transition de la phase tétragonale à la phase orthorhombique, alors que l'encadré (b) fait référence à la région qui reste dans la phase tétragonale même à $T = 4$ K. Dans la Fig. B.9 (a), l'émission de phase tétragonale disparaît totalement au-dessous de 120 K. Le pic de phase orthorhombique restant a un épaulement d'énergie élevé à ≈ 1600 meV, ce qui est attribué à l'émission de l'exciton libre de phase orthorhombique. Au-dessous de 60 K, l'intensité de l'exciton libre de phase orthorhombique diminue considérablement, et l'émission est dominée par le pic autour de 1560 mV, ce qui correspond à l'état d'exciton lié à la phase orthorhombique. En revanche, les spectres de la Fig. B.9 (b) montrent la dominance du pic de phase tétragonale, qui commence déjà à la température de transition de phase. Avec une diminution supplémentaire de la température, le pic de phase orthorhombique est par conséquent affaibli et disparaît totalement à des températures de 30 K ou moins. Une preuve de la coexistence de différents domaines de phase à basses températures se trouve également dans

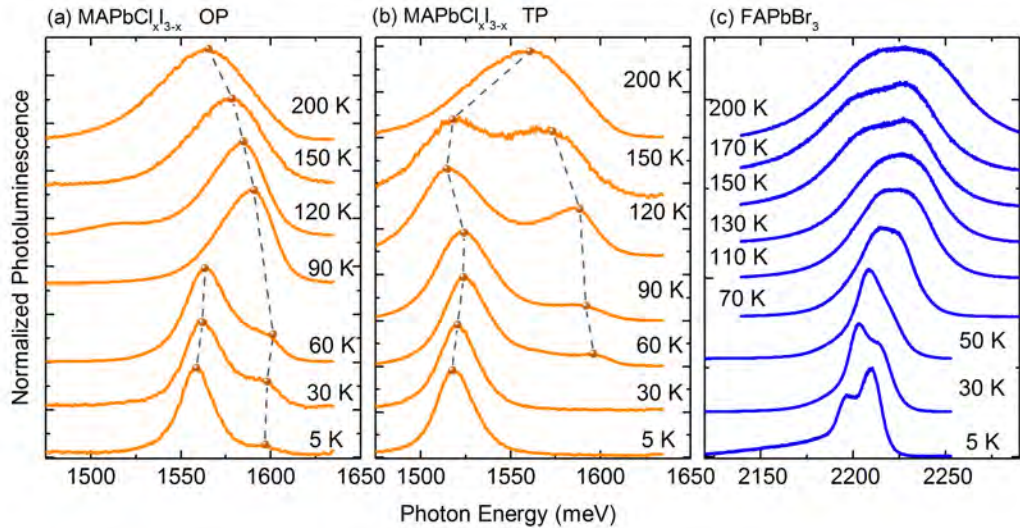


Figure B.9: (a), (b) dépendance en température de la *muPL* pour deux positions différentes sur $\text{MAPbCl}_x\text{I}_{3-x}$ correspondant respectivement aux domaines des phases orthorhombique et tétragonale. (c) Dépendance en température des spectres de *muPL* pour FAPbBr_3 .

la haute bande interdite FAPbBr_3 (Fig. B.9 (c)). A environ 150 - 160 K la composante basse énergie du pic d'émission à haute température est supprimée. Deux pics d'émission sont bien résolus en-dessous de 30 K.

Les inhomogénéités décrites ci-dessus sont notre motivation à étudier les propriétés microscopiques des pérovskites organo-plomb- halogénures avec micro- photoluminescence résolue spatialement, réalisées à différentes températures. Les résultats des mesures à température ambiante pour MAPbI_3 , $\text{MAPbCl}_x\text{I}_{3-x}$ et FAPbBr_3 respectivement, sont présentés dans la Fig. 5.3 (a) - (c). Les cartographies chromatiques, chaque $80 \times 80 \mu\text{m}$ avec des pas de $2 \mu\text{m}$, représentent l'intensité intégrée du pic de photoluminescence. Dans tous les échantillons, nous observons des variations notables de l'intensité d'émission dans les zones étudiées, révélant la présence des régions de photoluminescence plus forte et plus faible. Nous concluons donc que les trois composés ont une structure granulaire microcristalline et que la présence récemment remarquée des grains foncés [de Quilettes 2015, deQuilettes 2016] est typique des pérovskites organo-halogénures de plomb. Les résultats μPL à température ambiante résolue spatialement pour MAPbI_3 , $\text{MAPbCl}_x\text{I}_{3-x}$ et FAPbBr_3 respectivement, sont présentés sur la Fig. B.10 (a) - (c). Les cartographies chromatiques, chaque $80 \times 80 \mu\text{m}$ avec des pas de $2 \mu\text{m}$, représentent l'intensité intégrée du pic de photoluminescence. Dans tous les échantillons, nous observons des variations notables de l'intensité d'émission dans les zones étudiées, révélant la présence des régions de photoluminescence plus forte et plus faible. Nous concluons donc que les

trois composés ont une structure de grains microcristallins et que la présence récemment signalée des grains foncés est typique pour les pérovskites organo-halogénures de plomb.

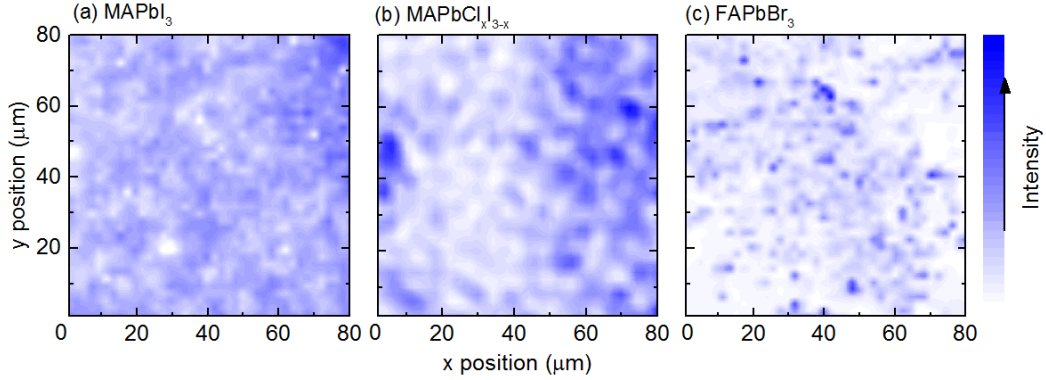


Figure B.10: Intensité intégrée du pic de μ PL en fonction de la position pour (a) MAPbI_3 , intensité d'illumination du spot 40 nW (4 W/cm^2), (b) $\text{MAPbCl}_x\text{I}_{3-x}$, intensité d'illumination du spot 60 nW (6 W/cm^2), et (c) FAPbBr_3 , intensité d'illumination du spot 100 nW (10 W/cm^2), respectivement à 300K. L'intensité intégrée passe du blanc au bleu. L'étape de numérisation est de $2\mu\text{m}$.

La μ PL spatialement résolue à basse température ($T = 4 \text{ K}$) pour MAPbI_3 est présentée dans la Fig. L'encadré (a) montre la photoluminescence de la phase orthorhombe à basse température. De même que les résultats de la température ambiante, l'émission est assez uniforme, avec une certaine variation sur une échelle de quelques μm liée à la structure microcristalline du film de pérovskite. Néanmoins, nous observons toujours les grains sombres et lumineux. Remarquablement, le pic de faible énergie, correspondant à la phase tétragonale à haute température, accompagne l'émission orthorhombe à certaines positions à travers l'échantillon. Les spectres typiques acquis pour deux positions différentes sur l'échantillon sont présentés dans l'encadré (c). Le spectre tracé en bleu représente une position où seul le pic orthorhombe se produit. La courbe rouge correspond à la position où les pics de phase orthorhombe et tétragonale sont détectés simultanément. Bien que l'intensité de l'émission de la phase tétragonale soit toujours inférieure à l'intensité du pic de phase orthorhombe dominante, l'apparition du pic de la phase tétragonale semble diminuer l'intensité du pic OP. L'intensité intégrée du pic de la phase tétragonale, indiquée par la couleur rouge, est superposée à l'intensité intégrée du pic de phase orthorhombe sur la Fig. 5.4 (b). L'émission de la phase tétragonale se trouve dans des zones isolées, peu fréquentes, de taille typique de 1 à 5 μm , où le pic de phase orthorhombe est généralement plus faible. Pour déterminer précisément s'il existe une corrélation entre les intensités d'émission des deux phases, nous analysons les proportions de l'émission totale dans chaque pic $\frac{I_{OP,TP}}{I_{TP}+I_{TP}}$ en fonction de l'intensité d'émission du pic de phase tétragonale (I_{TP}). Les résultats, présentés

à la Fig. (d), révèlent une anti-corrélation : à mesure que la proportion de l’émission dans le pic de la phase tétragonale (points oranges) augmente, la phase OP diminue progressivement.

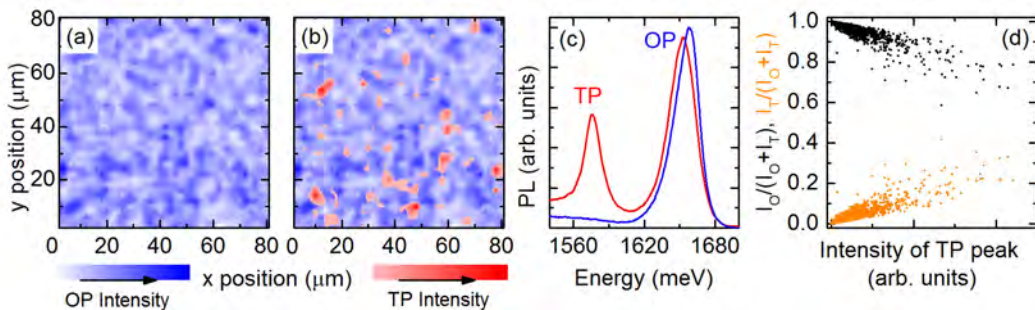


Figure B.11: Micro-photoluminescence résolue spatialement pour MAPbI_3 : (a) Intensité intégrée du pic (OP) à haute énergie en fonction de la position. L’intensité passe du blanc au bleu foncé. (b) Une deuxième cartographie du pic (TP) de faible énergie est superposée à la cartographie montrée en (a). L’intensité passe du blanc au rouge. (c) Spectres typiques pour des positions où seul le pic OP a été observé (bleu) et où les deux pics ont été observés (rouge). (d) Corrélation de l’intensité intégrée des pics TP (orange) et OP (noir) par rapport à l’intensité du pic TP à basse énergie.

Les restes à basse température de la phase tétragonale se retrouvent dans tous les films de pérovskite étudiés. La taille de ces inclusions varie généralement avec la taille des grains cristallins. Seulement pour FAPbBr_3 , l’échelle spatiale des variations de l’intensité de photoluminescence est remarquablement plus grande que celles observées dans d’autres composés. La structure du domaine de phase dans le bromure est apparemment indépendante sur la structure de grain de la couche, avec les domaines s’étendant sur 100 μm .

Les défauts formés naturellement dans le film mince de pérovskite sont les premiers candidats à être considérés comme la cause des inhomogénéités observées dans la progression de la transition de phase. À proximité de tels défauts, on observe une augmentation de la présence de la phase tétragonale à basse température, ce qui permet de mieux comprendre l’origine du comportement de formation de domaines observés dans les pérovskites organiques/inorganiques. Pour étudier ce problème, nous avons intentionnellement introduit un défaut dans le matériau de pellicule mince de la pérovskite en l’exposant à un spot de laser focalisé, comme présenté dans la Fig. B.12. Un spectre de PL typique représenté graphiquement dans l’encadré (d) contient trois pics d’émission à 1535 meV, 1555 meV et 1600 meV, attribués respectivement à la phase tétragonale et à l’exciton lié/libre de la phase orthorhombique. La cartographie révèle la dominance de l’exciton lié à OP dans l’échantillon (encadré (b)). Le centre du spot laser est un noyau foncé (coin supérieur droit de la cartographie). Cette région de PL très faible est entourée de taches d’émission lumineuse

provenant de la phase tétragonale (encadré (a)). Conséutivement, on observe des zones de formes annulaires où les excitons liés et libres de la phase orthorhombique dominant (encadrés (b), (c), respectivement).

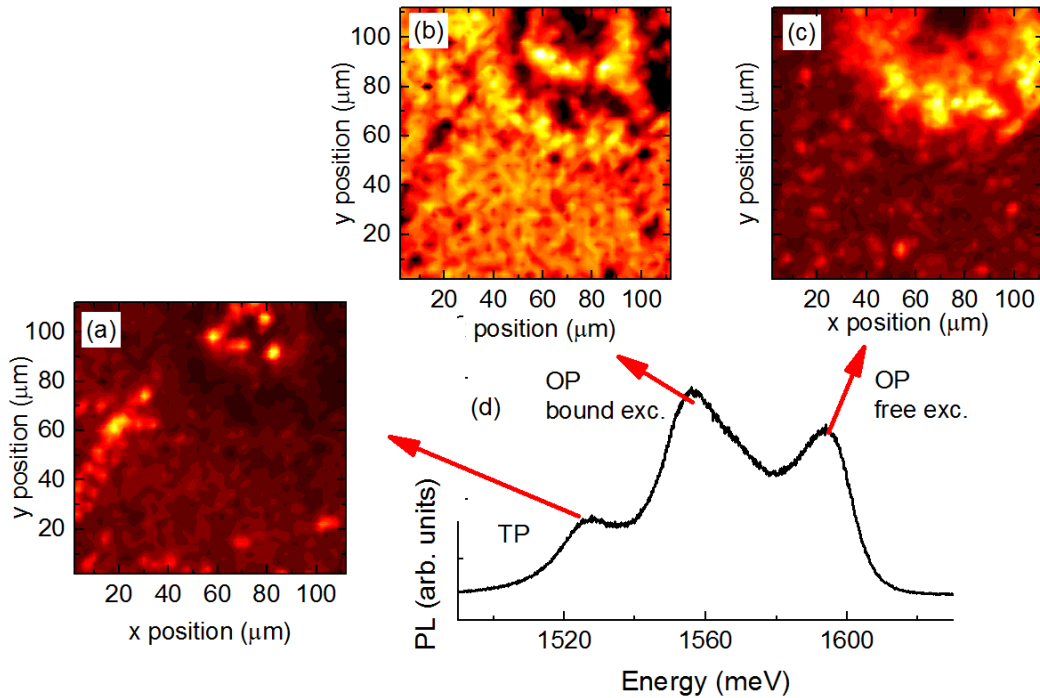


Figure B.12: (a) distribution des ions iodés en fonction de la distance par rapport au point d'exposition. (b) - (d) les cartographies d'intensité intégrées de l'échantillon correspondant à : (b) haute température, du pic TP et des pics d'exciton lié (c) et libre de l'OP à basse température. (e) Spectre de photoluminescence montrant toutes les transitions observées.

Une telle répartition des domaines de phase peut être expliquée par la présence de régions en teneur d'halogénure diminuée et augmentée, formées lors du photo-recuit. Nous nous attendons à ce que la migration ionique signalée dans [deQuilettes 2016] entraîne une distribution non-uniforme des halogénures dans la zone exposée, comme le montre schématiquement la Fig. (a). La lumière intense crée une région appauvrie, entourée par la région avec un excès d'iode. Les phases cristallines sont corrélées avec la teneur en halogénure, ce qui est en accord avec le modèle des domaines observés dans les cartographies chromatiques. Les régions non-affectées sont caractérisées par l'émission de l'exciton lié à la phase orthorhombique. Ainsi, l'émission d'excitons liée à la phase orthorhombique caractérise la teneur en iode standard, alors que la présence de la phase tétragonale indique une déficience de l'halogénure.

B.6. Les pérovskites halogénure d'plomb - et études magneto-optique

B.6 Les pérovskites halogénure d'plomb - et études magneto-optique

Dans le dernier chapitre, nous décrivons brièvement nos résultats préliminaires obtenu pour la famille de totalement inorganique halogénure de césum plomb pérovskites. Tout d'abord, nous décrivons les échantillons et la caractérisation études - la dépendance en température de la bande interdite. Ensuite, dans le présent mesures de l'énergie de liaison de l'exciton et efficace masse déterminée à basse température , a l'aide magnéto-spectroscopie. A basse température, lorsque les cations organiques sont ordonnées, l'image qualitative de la les interactions au sein du réseau est presque la même pour les deux des composés inorganiques ou hybrides. Nous prévoyons de déterminer si un plus différence marquée Survient a des températures plus élevées, correspondant a la gamme de phase tétragonale dans les composés hybrides, lorsque le modes du treillis organiques de libration sont autorisés. Ce sera étudié avec nos prochaines mesures magnéto-transmission sur la CsPbX_3 matériaux à ≈ 170 K.

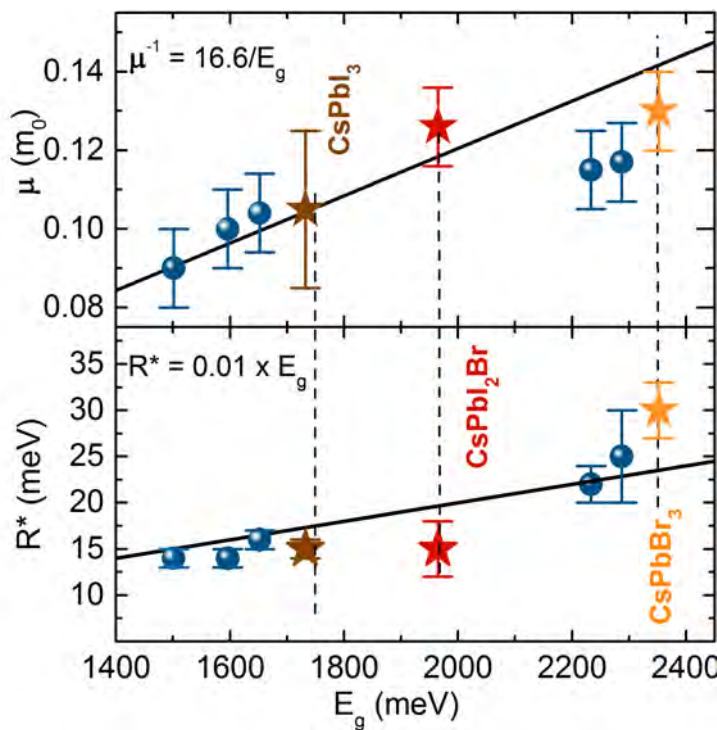


Figure B.13: (a) et (b) masse réduite et énergie de liaison à $T = 2$ K en fonction du gap d'énergie respectivement pour CsPbX_3 . Les symboles bleus indiquent les résultats pour les perovskites hybrides

B.7 Conclusions

Les perovskites organo-métalliques à base d'halogénure de plomb sont des candidats prometteurs comme absorbeurs de lumière dans les cellules solaires à faible coût et à haut rendement, ainsi que pour les OLEDs. Il a été récemment démontré, que le rendement de conversion des cellules basées sur les pérovskites hybrides à cations multiples peuvent atteindre jusqu'à 22 % et sont stables en conditions réelles. Cela indique que l'avenir des pérovskites pour le photovoltaïque est déterminé par le développement de nouveaux alliages. Par conséquent, une optimisation plus poussée des performances de ces matériaux nécessite un contrôle avancé à la fois des propriétés électronique et de la morphologie. Pour cela, il faut une compréhension fine de l'évolution ces paramètres avec la composition chimique. Dans cette thèse, nous utilisons des méthodes optiques pour étudier les paramètres électroniques de base: l'énergie de liaison de l'exciton et sa masse réduite en fonction de la morphologie chez plusieurs perovskites organo-métalliques à base d'halogénure de plomb. En étudiant des composés basés sur les cations organiques tels que le méthylammonium ou le formamidinium ainsi que différents halides, nous déterminons comment ces paramètres sont influencés par le type d'ions.

Avant les mesures dans un champ magnétique, nous caractérisons notre échantillons utilisant la dépendance en température de la transmission optique UV-VIS. Ces études, réalisées à des températures allant de 4 à 300K, nous permettent de suivre les changements de l'énergie de bande interdite avec l'augmentation de la température. En particulier, nous analysons le développement de la transition structurelle de la phase orthorhombique à la phase tétragonale, se produisant à environ 160K. Nous montrons que l'apparition la phase tétragonale conduit toujours à une baisse de l'énergie de bande interdite, dans la gamme de 15 – 90 meV pour les différents composés. Une autre différence est la plage de température pour laquelle la transition de phase progresse, variant de 15K à 50K. Ceci est une indication que la transition de phase n'est pas uniforme dans le film à cause de la distribution de température de transition des différents grains cristallins.

En outre, nous étudions les valeurs de l'énergie de liaison exciton et masse réduite mesurant la magnéto-transmission en champs magnétiques intenses jusqu'à 67 T. De plus, nous étayons notre analyse avec des mesures obtenus lors l'impulsion courte Mega Gauss dans les champs jusqu'à 150T (en coopération avec A. Miyata, LNCMI). Nous analysons l'évolution du champ magnétique des énergies des transitions interbandes entre les états excitoniques et libres. Nous extrayons R^* et μ en ajustant ces transitions particulières avec le modèle de l'atome d'hydrogène dans un champ magnétique (états excitoniques) et Landau (États de porteurs libres). Cette méthode directe permet une meilleure précision d'estimation des ces paramètres comparés à ceux obtenus par des mesures indirectes. Nous obtenons ainsi des relations générales pour l'énergie de liaison des excitons R^* et la masse réduite μ , qui sont principalement déterminés par la bande interdite E_g pour toute la famille des pérovskites hybrides: $R^* = 0,01 \times E_g$ et $\frac{\mu}{m_0} = \frac{E_g}{16.6}$,

Les propriétés électroniques de base peuvent ainsi être facilement estimées pour

de nouveau composés synthétisés. Il n'y a pas de preuve d'une importante influence du type de cations organiques autre que celle résultant de changements dans l'énergie de bande interdite. Cela suggère un modèle à deux bandes simples en théorie des perturbations $\mathbf{k} \cdot \mathbf{p}$ qui devrait permettre la modélisation précise des propriétés des dispositifs fabriqués à partir de pérovskites hybrides. Nous avons aussi démontré que les valeurs de l'énergie de liaison des excitons sont plus petites ou comparables à l'énergie thermique à 300K, ce qui apporte une contribution significative à la compréhension des excellentes performances de ces matériaux dans les dispositifs photovoltaïques.

Pour les tri-iodures, ces valeurs sont encore réduites dans les phases à haute température de ces matériaux. Ceci est en accord avec le contribution de la libraisons des cations organiques polaires sur l'écrantage diélectrique, suggéré dans la littérature pour structures cristallines à haute température. Par contre, ce phénomène n'est pas observé dans le tri-bromure, caractérisé par une bande interdite plus large. Une explication possible est que l'énergie de liaison exciton dans ce composé, significativement plus grande que l'énergie des phonons correspondant aux libraisons des cations organiques, est probablement trop élevée pour être efficacement réduit par le cation lié.

Afin de confirmer le rôle des cations organiques dans la réduction de l'énergie de liaison exciton à haute température, nous effectuons actuellement, des études magnéto-optiques de composés totalement inorganiques, à base de césum. Nos résultats préliminaires ont été obtenus à basse température, au cours de laquelle les mouvements du réseau organique sont réduits. Dans de telles conditions, les interactions électrons-trous sont très similaires pour les familles hybrides et inorganiques des perovskites.

Enfin, nous avons effectués de la micro-photoluminescence dépendant de la température. Les cartes résultantes montrent que les films minces de pérovskite sont composés à partir des grains cristallins sombres et brillants, avec des tailles comprises entre 1 et 20 micromètres dans le cas de l'halogénure mixte $\text{MAPbCl}_x\text{I}_{3-x}$. Nous démontrons que la transition de phase à basse température de tétragonale à orthorhombique est incomplete dans tous les matériaux étudiés, car des restes de la phase tétragonale se trouve même à $T = 4$ K. Ceci est le plus évident dans le FAPbBr_3 , où les domaines macroscopiques de la phase tétragonale, s'étendant sur des centaines de grains adjacents. Dans d'autres composés, la surface des inclusions tétragonales est limitée à la taille de grains monocristallins. Ces inclusions peuvent être encore plus petites, en raison des grandes longueurs de diffusion des porteurs dans les perovskites. Les matériaux tétragonaux à faible bande interdite peuvent collecter des porteurs sur de grandes régions, ce qui donne lieu à un pic PL relativement fort correspondant à la phase tétragonale. En étudiant les régions structurellement endommagées et photo-recuites, où l'apparition de la phase tétragonale à basse température est renforcée, nous attribuons sa présence à la teneur réduite en halogénures.

En effet, la micro-photoluminescence à basse température permettent de détecter de faibles inhomogénéités dans les films de pérovskite, qui ne sont pas observées.

ables à température ambiante.

Bibliography

- [Aguado 2012] Fernando Aguado, Fernando Rodríguez, Rafael Valiente, Jean-Paul Itiè and Michael Hanfland. *Pressure effects on Jahn-Teller distortion in perovskites: The roles of local and bulk compressibilities.* Phys. Rev. B, vol. 85, page 100101, Mar 2012. (Cited on page 8.)
- [Amat 2014] Anna Amat, Edoardo Mosconi, Enrico Ronca, Claudio Quarti, Paolo Umari, Md. K. Nazeeruddin, Michael Grätzel and Filippo De Angelis. *Cation-Induced Band-Gap Tuning in Organohalide Perovskites: Interplay of Spin-Orbit Coupling and Octahedra Tilting.* Nano Letters, vol. 14, no. 6, pages 3608–3616, 2014. PMID: 24797342. (Cited on pages 7, 8, 9, 10, 11, 64 and 103.)
- [Anaraki 2016] Elham Halvani Anaraki, Ahmad Kermanpur, Ludmilla Steier, Konrad Domanski, Taisuke Matsui, Wolfgang Tress, Michael Saliba, Antonio Abate, Michael Gratzel, Anders Hagfeldt and Juan-Pablo Correa-Baena. *Highly efficient and stable planar perovskite solar cells by solution-processed tin oxide.* Energy Environ. Sci., pages –, 2016. (Cited on page 9.)
- [Aukerman 1967] L. W. Aukerman. *Diffusion Lengths of Electrons and Holes in GaAs.* J. Appl. Phys., vol. 38, no. 2, page 685, 1967. (Cited on page 18.)
- [Bailie 2015] Colin D. Bailie, M. Greyson Christoforo, Jonathan P. Mailoa, Andrea R. Bowring, Eva L. Unger, William H. Nguyen, Julian Burschka, Norman Pellet, Jungwoo Z. Lee, Michael Gratzel, Rommel Noufi, Tonio Buonassisi, Alberto Salleo and Michael D. McGehee. *Semi-transparent perovskite solar cells for tandems with silicon and CIGS.* Energy Environ. Sci., vol. 8, pages 956–963, 2015. (Cited on page 20.)
- [Beal 2016] Rachel E. Beal, Daniel J. Slotcavage, Tomas Leijtens, Andrea R. Bowring, Rebecca A. Belisle, William H. Nguyen, George F. Burkhard, Eric T. Hoke and Michael D. McGehee. *Cesium Lead Halide Perovskites with Improved Stability for Tandem Solar Cells.* J. Phys. Chem. Lett., vol. 7, no. 5, pages 746–751, mar 2016. (Cited on pages 23 and 81.)
- [Béard 2012] J. Béard, J. Billette, P. Frings, M. Suleiman and F. Lecouturier. *Special Coils Development at the National High Magnetic Field Laboratory in Toulouse.* Journal of Low Temperature Physics, vol. 170, no. 5, pages 442–446, 2012. (Cited on page 27.)
- [Behnke 1978] G. Behnke, H. Buttner and J. Pollmann. *Ground state energy of the exciton-phonon system in a magnetic field.* Solid State Communications, vol. 20, pages 873–876, 1978. (Cited on pages 66 and 104.)

- [Bi 2016] D. Bi, W. Tress, M. I. Dar, P. Gao, J. Luo, C. Renevier, K. Schenk, A. Abate, F. Giordano, J.-P. Correa Baena, J.-D. Decoppet, S. M. Zakeeruddin, M. K. Nazeeruddin, M. Gra tzel and A. Hagfeldt. *Efficient luminescent solar cells based on tailored mixed-cation perovskites*. Science Advances, vol. 2, no. 1, pages e1501170–e1501170, jan 2016. (Cited on page 22.)
- [Binek 2016] Andreas Binek, Irene Grill, Niklas Huber, Kristina Peters, Alexander G. Hufnagel, Matthias Handloser, Pablo Docampo, Achim Hartschuh and Thomas Bein. *Control of Perovskite Crystal Growth by Methylammonium Lead Chloride Templating*. Chem. Asian J., vol. 11, no. 8, pages 1199–1204, mar 2016. (Cited on page 21.)
- [Brenner 2015] Thomas M. Brenner, David A. Egger, Andrew M. Rappe, Leeor Kronik, Gary Hodes and David Cahen. *Are Mobilities in Hybrid Organic-Inorganic Halide Perovskites Actually High?* The Journal of Physical Chemistry Letters, vol. 6, no. 23, pages 4754–4757, 2015. PMID: 26631359. (Cited on page 18.)
- [Brenner 2016] Thomas M. Brenner, David A. Egger, Leeor Kronik, Gary Hodes and David Cahen. *Hybrid organic-inorganic perovskites: low-cost semiconductors with intriguing charge-transport properties*. Nature Reviews Materials, vol. 1, no. 1, page 15007, jan 2016. (Cited on page 17.)
- [Brivio 2014] F. Brivio, K.T. Butler, A. Walsh and M. van Schilfgaarde. *Relativistic quasiparticle self-consistent electronic structure of hybrid halide perovskite photovoltaic absorbers*. Phys. Rev. B, vol. 89, page 155204, 2014. (Cited on pages 65 and 103.)
- [Brivio 2015] Federico Brivio, Jarvist M. Frost, Jonathan M. Skelton, Adam J. Jackson, Oliver J. Weber, Mark T. Weller, Alejandro R. Goñi, Aurélien M. A. Leguy, Piers R. F. Barnes and Aron Walsh. *Lattice dynamics and vibrational spectra of the orthorhombic, tetragonal, and cubic phases of methylammonium lead iodide*. Phys. Rev. B, vol. 92, page 144308, Oct 2015. (Cited on page 8.)
- [Chen 2014a] Chang-Wen Chen, Hao-Wei Kang, Sheng-Yi Hsiao, Po-Fan Yang, Kai-Ming Chiang and Hao-Wu Lin. *Efficient and Uniform Planar-Type Perovskite Solar Cells by Simple Sequential Vacuum Deposition*. Advanced Materials, vol. 26, no. 38, pages 6647–6652, 2014. (Cited on page 37.)
- [Chen 2014b] Qi Chen, Huanping Zhou, Tze-Bin Song, Song Luo, Ziruo Hong, Hsin-Sheng Duan, Letian Dou, Yongsheng Liu and Yang Yang. *Controllable Self-Induced Passivation of Hybrid Lead Iodide Perovskites toward High Performance Solar Cells*. Nano Letters, vol. 14, no. 7, pages 4158–4163, 2014. PMID: 24960309. (Cited on pages 67 and 104.)

- [Chiba 2006] Yasuo Chiba, Ashraful Islam, Yuki Watanabe, Ryoichi Komiya, Naoki Koide and Liyuan Han. *Dye-Sensitized Solar Cells with Conversion Efficiency of 11.1%*. Japanese Journal of Applied Physics, vol. 45, no. 7L, page L638, 2006. (Cited on page 19.)
- [Chuang 1995] S. Chuang. Physics of optoelectronic devices. Wiley: New York, 1995. (Cited on pages 64 and 102.)
- [Conings 2015] Bert Conings, Jeroen Drijkoningen, Nicolas Gauquelin, Aslihan Babayigit, Jan DHaen, Lien DOlieslaeger, Anitha Ethirajan, Jo Verbeeck, Jean Manca, Edoardo Mosconi, Filippo De Angelis and Hans-Gerd Boyen. *Intrinsic Thermal Instability of Methylammonium Lead Trihalide Perovskite*. Advanced Energy Materials, vol. 5, no. 15, page 1500477, jun 2015. (Cited on page 14.)
- [Correa Baena 2015] Juan Pablo Correa Baena, Ludmilla Steier, Wolfgang Tress, Michael Saliba, Stefanie Neutzner, Taisuke Matsui, Fabrizio Giordano, T. Jesper Jacobsson, Ajay Ram Srimath Kandada, Shaik M. Zakeeruddin, Annamaria Petrozza, Antonio Abate, Mohammad Khaja Nazeeruddin, Michael Gratzel and Anders Hagfeldt. *Highly efficient planar perovskite solar cells through band alignment engineering*. Energy Environ. Sci., vol. 8, pages 2928–2934, 2015. (Cited on page 22.)
- [da Silva 2015] E. Lora da Silva, Jonathan M. Skelton, Stephen C. Parker and Aron Walsh. *Phase stability and transformations in the halide perovskite CsSnI₃*. Phys. Rev. B, vol. 91, page 144107, Apr 2015. (Cited on pages 12, 81 and 83.)
- [Dar 2014] M. Ibrahim Dar, Neha Arora, Peng Gao, Shahzada Ahmad, Michael Grätzel and Mohammad Khaja Nazeeruddin. *Investigation Regarding the Role of Chloride in Organic-Inorganic Halide Perovskites Obtained from Chloride Containing Precursors*. Nano Letters, vol. 14, no. 12, pages 6991–6996, dec 2014. (Cited on page 21.)
- [de Quilettes 2015] Dane W. de Quilettes, Sarah M. Vorpahl, Samuel D. Stranks, Hirokazu Nagaoka, Giles E. Eperon, Mark E. Ziffer, Henry J. Snaith and David S. Ginger. *Impact of microstructure on local carrier lifetime in perovskite solar cells*. Science, vol. 348, no. 6235, pages 683–686, 2015. (Cited on pages 68, 71, 104 and 105.)
- [Debray 2013] Francois Debray and Paul Frings. *State of the art and developments of high field magnets at the Laboratoire National des Champs Magnétiques Intenses*. Comptes Rendus Physique, vol. 14, no. 1, pages 2 – 14, 2013. (Cited on page 26.)
- [deQuilettes 2016] Dane W. deQuilettes, Wei Zhang, Victor M. Burlakov, Daniel J. Graham, Tomas Leijtens, Anna Osherov, Vladimir Bulović, Henry J. Snaith, David S. Ginger and Samuel D. Stranks. *Photo-induced halide redistribution*

- in organic–inorganic perovskite films.* Nature Communications, vol. 7, page 11683, may 2016. (Cited on pages 71, 78, 105 and 108.)
- [Deschler 2014] Felix Deschler, Michael Price, Sandeep Pathak, Lina E. Klintberg, David-Dominik Jarausch, Ruben Higler, Sven Hüttner, Tomas Leijtens, Samuel D. Stranks, Henry J. Snaith, Mete Atatüre, Richard T. Phillips and Richard H. Friend. *High Photoluminescence Efficiency and Optically Pumped Lasing in Solution-Processed Mixed Halide Perovskite Semiconductors.* The Journal of Physical Chemistry Letters, vol. 5, no. 8, pages 1421–1426, 2014. PMID: 26269988. (Cited on pages 21 and 71.)
- [DIInnocenzo 2014] Valerio DIInnocenzo, Giulia Grancini, Marcelo J.P. Alcocer, Ajay Ram Srimath Kandada, Samuel D. Stranks, Michael M. Lee, Guglielmo Lanzani, Henry J. Snaith and Annamaria Petrozza. *Excitons versus free charges in "organo-lead tri-halide" perovskites.* Nature Communications, vol. 5, April 2014. (Cited on pages 5 and 46.)
- [Dong 2015] Qingfeng Dong, Yanjun Fang, Yuchuan Shao, Padhraic Mulligan, Jie Qiu, Lei Cao and Jinsong Huang. *Electron-hole diffusion lengths > 175 μm in solution-grown CH₃NH₃PbI₃ single crystals.* Science, vol. 347, no. 6225, pages 967–970, 2015. (Cited on pages 18 and 20.)
- [Edelman 1992] P Edelman, W Henley and J Lagowski. *Photoluminescence and minority carrier diffusion length imaging in silicon and GaAs.* Semiconductor Science and Technology, vol. 7, no. 1A, page A22, 1992. (Cited on page 18.)
- [Eperon 2014a] Giles E. Eperon, Victor M. Burlakov, Pablo Docampo, Alain Goriely and Henry J. Snaith. *Morphological Control for High Performance, Solution-Processed Planar Heterojunction Perovskite Solar Cells.* Advanced Functional Materials, vol. 24, no. 1, pages 151–157, 2014. (Cited on pages 9, 23 and 36.)
- [Eperon 2014b] Giles E. Eperon, Samuel D. Stranks, Christopher Menelaou, Michael B. Johnston, Laura M. Herz and Henry J. Snaith. *Formamidinium lead trihalide: a broadly tunable perovskite for efficient planar heterojunction solar cells.* Energy Environ. Sci., vol. 7, pages 982–988, 2014. (Cited on pages 13, 21, 22, 67 and 104.)
- [Eperon 2015] Giles E. Eperon, Giuseppe M. Paternò, Rebecca J. Sutton, Andrea Zampetti, Amir Abbas Haghhighirad, Franco Cacialli and Henry J. Snaith. *Inorganic caesium lead iodide perovskite solar cells.* J. Mater. Chem. A, vol. 3, no. 39, pages 19688–19695, 2015. (Cited on pages 81, 82 and 83.)
- [Etgar 2012] Lioz Etgar, Peng Gao, Zhaosheng Xue, Qin Peng, Aravind Kumar Chandiran, Bin Liu, Md. K. Nazeeruddin and Michael Grätzel. *Mesoscopic CH₃NH₃PbI₃/TiO₂ Heterojunction Solar Cells.* Journal of the American Chemical Society, vol. 134, no. 42, pages 17396–17399, 2012. PMID: 23043296. (Cited on page 18.)

- [Etienne 2016] Thibaud Etienne, Edoardo Mosconi and Filippo De Angelis. *Dynamical Origin of the Rashba Effect in Organohalide Lead Perovskites: A Key to Suppressed Carrier Recombination in Perovskite Solar Cells?* J. Phys. Chem. Lett., vol. 7, no. 9, pages 1638–1645, may 2016. (Cited on page 11.)
- [Even 2012] J. Even, L Pedesseau, A. Dupertuis M, J.-M Jancu and C. Katan. *Electronic model for self-assembled hybrid organic/perovskite semiconductors: Reverse band edge electronic states ordering and spin-orbit coupling.* Phys. Rev. B, vol. 86, page 205301, 2012. (Cited on pages 15 and 64.)
- [Even 2013] Jacky Even, Laurent Pedesseau, Jean-Marc Jancu and Claudine Katan. *Importance of Spin-Orbit Coupling in Hybrid Organic/Inorganic Perovskites for Photovoltaic Applications.* The Journal of Physical Chemistry Letters, vol. 4, no. 17, pages 2999–3005, 2013. (Cited on page 17.)
- [Even 2014a] Jacky Even, Laurent Pedesseau, Jean-Marc Jancu and Claudine Katan. *DFT and $k \cdot p$ modelling of the phase transitions of lead and tin halide perovskites for photovoltaic cells.* physica status solidi (RRL) Rapid Research Letters, vol. 8, no. 1, pages 31–35, 2014. (Cited on pages 15 and 17.)
- [Even 2014b] Jacky Even, Laurent Pedesseau and Claudine Katan. *Analysis of Multivalley and Multibandgap Absorption and Enhancement of Free Carriers Related to Exciton Screening in Hybrid Perovskites.* The Journal of Physical Chemistry C, vol. 118, no. 22, pages 11566–11572, 2014. (Cited on pages 12, 15, 16, 17, 46, 61, 64, 65, 66, 103 and 104.)
- [Even 2015] Jacky Even, Laurent Pedesseau, Claudine Katan, Mikaël Kepenekian, Jean-Sébastien Lauret, Daniel Sapiro and Emmanuelle Deleporte. *Solid-State Physics Perspective on Hybrid Perovskite Semiconductors.* J. Phys. Chem. C, vol. 119, no. 19, pages 10161–10177, may 2015. (Cited on pages 59, 63 and 102.)
- [Facchetti 2011] Antonio Facchetti. *π -Conjugated Polymers for Organic Electronics and Photovoltaic Cell Applications.* Chemistry of Materials, vol. 23, no. 3, pages 733–758, 2011. (Cited on page 19.)
- [Fang 2015] H-H. Fang, R. Raissa, M. Abdu-Aguye, S. Adjokatse, G.R. Blake, J. Even and M.A. Loi. *Photophysics of Organic-Inorganic Hybrid Lead Iodide Perovskite Single Crystals.* Adv. Funct. Mater., vol. 25, no. 16, pages 2378–2385, APR 22 2015. (Cited on page 64.)
- [Frenkel 1931] J. Frenkel. *On the Transformation of light into Heat in Solids. I.* Phys. Rev., vol. 37, pages 17–44, Jan 1931. (Cited on page 3.)
- [Frings 2008] Paul Frings, Holger Witte, Harry Jones, Jérôme Béard and Thomas Hermannsdoerfer. *Rapid Cooling Methods for Pulsed Magnets.* IEEE Transactions on Applied Superconductivity, vol. 18, no. 2, pages 612–615, 2008. (Cited on page 28.)

- [Frost 2016] J.M. Frost and A. Walsh. Organic-inorganic halide perovskite photovoltaics, chapitre 3, pages 2–6. Springer Nature, 2016. (Cited on page 11.)
- [Gong 2015] Ke Gong and David F. Kelley. *Surface Charging and Trion Dynamics in CdSe-Based Core/Shell Quantum Dots*. The Journal of Physical Chemistry C, vol. 119, no. 17, pages 9637–9645, 2015. (Cited on page 6.)
- [Gordon 2016] Elijah E. Gordon, Ke Xu, Hongjun Xiang, Annette Bussmann-Holder, Reinhard K. Kremer, Arndt Simon, Jürgen Köhler and Myung-Hwan Whangbo. *Structure and Composition of the 200 K-Superconducting Phase of H₂S at Ultrahigh Pressure: The Perovskite (SH⁻)(H₃S⁺)*. Angewandte Chemie International Edition, vol. 55, no. 11, pages 3682–3684, feb 2016. (Cited on page 6.)
- [Green 2014] Martin A. Green, Anita Ho-Baillie and Henry J. Snaith. *The emergence of perovskite solar cells*. Nature Photonics, vol. 8, pages 506–514, 2014. (Cited on page 37.)
- [Green 2015a] Martin A. Green, Keith Emery, Yoshihiro Hishikawa, Wilhelm Warta and Ewan D. Dunlop. *Solar cell efficiency tables (version 47)*. Prog. Photovolt: Res. Appl., vol. 24, no. 1, pages 3–11, nov 2015. (Cited on pages 19 and 22.)
- [Green 2015b] Martin A. Green, Yajie Jiang, Arman Mahboubi Soufiani and Anita Ho-Baillie. *Optical Properties of Photovoltaic Organic-Inorganic Lead Halide Perovskites*. The Journal of Physical Chemistry Letters, vol. 6, no. 23, pages 4774–4785, 2015. and other references cited there. (Cited on page 17.)
- [Habisreutinger 2014] Severin N. Habisreutinger, Tomas Leijtens, Giles E. Eperon, Samuel D. Stranks, Robin J. Nicholas and Henry J. Snaith. *Carbon Nanotube/Polymer Composites as a Highly Stable Hole Collection Layer in Perovskite Solar Cells*. Nano Letters, vol. 14, no. 10, pages 5561–5568, oct 2014. (Cited on pages 13 and 14.)
- [Haldane 1988] F. D. M. Haldane. *Model for a Quantum Hall Effect without Landau Levels: Condensed-Matter Realization of the "Parity Anomaly"*. Physical Review Letters, vol. 61, no. 18, pages 2015–2018, oct 1988. (Cited on page 6.)
- [Han 2012] Liyuan Han, Ashraful Islam, Han Chen, Chandrasekharam Malapaka, Barreddi Chiranjeevi, Shufang Zhang, Xudong Yang and Masatoshi Yanagida. *High-efficiency dye-sensitized solar cell with a novel co-adsorbent*. Energy Environ. Sci., vol. 5, pages 6057–6060, 2012. (Cited on page 19.)
- [Haugeneder 1999] A. Haugeneder, M. Neges, C. Kallinger, W. Spirk, U. Lemmer, J. Feldmann, U. Scherf, E. Harth, A. Gügel and K. Müllen. *Exciton diffusion and dissociation in conjugated polymer/fullerene blends and heterostructures*. Phys. Rev. B, vol. 59, pages 15346–15351, Jun 1999. (Cited on page 19.)

- [Hayashi 1950] Masakazu Hayashi and Kiichiro Katsuki. *Absorption Spectrum of Cuprous Oxide*. Journal of the Physical Society of Japan, vol. 5, no. 5, pages 380B–381, sep 1950. (Cited on page 3.)
- [He 2001] T. He, Q. Huang, A. P. Ramirez, Y. Wang, K. A. Regan, N. Rogado, M. A. Hayward, M. K. Haas, J. S. Slusky, K. Inumara, H. W. Zandbergen, N. P. Ong and R. J. Cava. *Superconductivity in the non-oxide perovskite $MgCNi_3$* . Nature, vol. 411, no. 6833, pages 54–56, may 2001. (Cited on page 6.)
- [Hirasawa 1994] M. Hirasawa, T. Ishihara, T. Goto, K. Uchida and N. Miura. *Magnetoabsorption of the lowest exciton in perovskite-type compound $(CH_3NH_3)PbI_3$* . Physica B: Condensed Matter, vol. 201, pages 427–430, jul 1994. (Cited on page 46.)
- [Hoke 2015] Eric T. Hoke, Daniel J. Slotcavage, Emma R. Dohner, Andrea R. Bowring, Hemamala I. Karunadasa and Michael D. McGehee. *Reversible photo-induced trap formation in mixed-halide hybrid perovskites for photovoltaics*. Chem. Sci., vol. 6, pages 613–617, 2015. (Cited on pages 9, 10 and 14.)
- [Huang 2013] Ling-yi Huang and Walter R. L. Lambrecht. *Electronic band structure, phonons, and exciton binding energies of halide perovskites $CsSnCl_3$, $CsSnBr_3$, and $CsSnI_3$* . Physical Review B, vol. 88, no. 16, oct 2013. (Cited on page 16.)
- [Jeon 2014] Nam Joong Jeon, Jun Hong Noh, Young Chan Kim, Woon Seok Yang, Seungchan Ryu and Sang Il Seok. *Solvent engineering for high-performance inorganic–organic hybrid perovskite solar cells*. Nature materials, vol. 13, no. 9, pages 897–903, 2014. (Cited on pages 20 and 37.)
- [Jeon 2015] Nam Joong Jeon, Jun Hong Noh, Woon Seok Yang, Young Chan Kim, Seungchan Ryu, Jangwon Seo and Sang Il Seok. *Compositional engineering of perovskite materials for high-performance solar cells*. Nature, vol. 517, no. 7535, pages 476–480, jan 2015. (Cited on pages 13 and 22.)
- [Jha 2009] Praket P. Jha and Philippe Guyot-Sionnest. *Trion Decay in Colloidal Quantum Dots*. ACS Nano, vol. 3, no. 4, pages 1011–1015, 2009. PMID: 19341263. (Cited on page 6.)
- [Jin 2012] Hosub Jin, Jino Im and Arthur J. Freeman. *Topological insulator phase in halide perovskite structures*. Phys. Rev. B, vol. 86, no. 12, sep 2012. (Cited on page 6.)
- [Johnsson 2007] Mats Johnsson and Peter Lemmens. Crystallography and chemistry of perovskites. John Wiley & Sons, Ltd, 2007. and other cited there. (Cited on pages 6, 7, 8, 9 and 94.)

- [Jones 2004] Harry Jones, Paul H Frings, Michael von Ortenberg, Alex Lagutin, Luc Van Bockstal, Oliver Portugall and Fritz Herlach. *First experiments in fields above 75 T in the European "coilin-coilex" magnet.* Physica B: Condensed Matter, vol. 346347, pages 553 – 560, 2004. Proceedings of the 7th International Symposium on Research in High Magnetic Fields. (Cited on page 27.)
- [Kalt 2013] H. Kalt and M. Hetterich. Optics of semiconductors and their nanostructures. Springer Series in Solid-State Sciences. Springer Berlin Heidelberg, 2013. and otherreferences cited there. (Cited on page 6.)
- [Kane 1978] E.O. Kane. *Pollmann-Büttner variational method for excitonic polarons.* Phys. Rev. B, vol. 18, pages 6849–6855, 1978. (Cited on page 65.)
- [Kawabata 1977] T. Kawabata, K. Muro and S. Narita. *Observation of cyclotron resonance absorptions due to excitonic ion and excitonic molecule ion in silicon.* Solid State Communications, vol. 23, no. 4, pages 267–270, jul 1977. (Cited on page 6.)
- [Kheng 1993] K. Kheng, R. T. Cox, Merle Y. d' Aubigné, Franck Bassani, K. Saminadayar and S. Tatarenko. *Observation of negatively charged excitons X^- in semiconductor quantum wells.* Phys. Rev. Lett., vol. 71, pages 1752–1755, Sep 1993. (Cited on page 6.)
- [Kieslich 2015] Gregor Kieslich, Shijing Sun and Anthony K. Cheetham. *An extended Tolerance Factor approach for organic-inorganic perovskites.* Chem. Sci., vol. 6, pages 3430–3433, 2015. (Cited on pages 7 and 8.)
- [Kim 2012] Hui-Seon Kim, Chang-Ryul Lee, Jeong-Hyeok Im, Ki-Beom Lee, Thomas Moehl, Arianna Marchioro, Soo-Jin Moon, Robin Humphry-Baker, Jun-Ho Yum, Jacques E. Moser, Michael Grätzel and Nam-Gyu Park. *Lead Iodide Perovskite Sensitized All-Solid-State Submicron Thin Film Mesoscopic Solar Cell with Efficiency Exceeding 9%.* Sci. Rep., vol. 2, aug 2012. (Cited on page 14.)
- [Kim 2014] Minsung Kim, Jino Im, Arthur J. Freeman, Jisoon Ihm and Hosub Jin. *Switchable $S = 1/2$ and $J = 1/2$ Rashba bands in ferroelectric halide perovskites.* Proceedings of the National Academy of Sciences, vol. 111, no. 19, pages 6900–6904, 2014. (Cited on page 59.)
- [Koh 2014] Teck Ming Koh, Kunwu Fu, Yanan Fang, Shi Chen, T. C. Sum, Nripan Mathews, Subodh G. Mhaisalkar, Pablo P. Boix and Tom Baikie. *Formamidinium-Containing Metal-Halide: An Alternative Material for Near-IR Absorption Perovskite Solar Cells.* J. Phys. Chem. C, vol. 118, no. 30, pages 16458–16462, jul 2014. (Cited on pages 21 and 22.)
- [Kojima 2009] Akihiro Kojima, Kenjiro Teshima, Yasuo Shirai and Tsutomu Miyasaka. *Organometal Halide Perovskites as Visible-Light Sensitizers for*

- Photovoltaic Cells.* J. Am. Chem. Soc., vol. 131, no. 17, pages 6050–6051, may 2009. (Cited on pages 9 and 13.)
- [Kong 2015] Weiguang Kong, Zhenyu Ye, Zhen Qi, Bingpo Zhang, Miao Wang, Arash Rahimi-Iman and Huizhen Wu. *Characterization of an abnormal photoluminescence behavior upon crystal-phase transition of perovskite $CH_3NH_3PbI_3$.* Phys. Chem. Chem. Phys., vol. 17, pages 16405–16411, 2015. (Cited on pages 12, 68 and 69.)
- [Kossacki 2000] P Kossacki, V Ciulin, J Cibert, Y Merle d'Aubigné, A Arnoult, C Bourgognon, A Wasiela, S Tatarenko, J.-L Staehli, J.D Ganière, B Deveaud and J.A Gaj. *Oscillator strengths of charged excitons: combining magnetoabsorption and photoluminescence dynamics in semimagnetic quantum wells.* Journal of Crystal Growth, vol. 214-215, pages 837–841, jun 2000. (Cited on page 6.)
- [Kroeze 2003] Jessica E. Kroeze, * Tom J. Savenije, Martien J. W. Vermeulen, and John M. Warman. *Contactless Determination of the Photoconductivity Action Spectrum, Exciton Diffusion Length, and Charge Separation Efficiency in Polythiophene-Sensitized TiO_2 Bilayers.* The Journal of Physical Chemistry B, vol. 107, no. 31, pages 7696–7705, 2003. (Cited on page 19.)
- [Kulbak 2015] Michael Kulbak, David Cahen and Gary Hodes. *How Important Is the Organic Part of Lead Halide Perovskite Photovoltaic Cells? Efficient $CsPbBr_3$ Cells.* J. Phys. Chem. Lett., vol. 6, no. 13, pages 2452–2456, jul 2015. (Cited on pages 81 and 82.)
- [Kulbak 2016] Michael Kulbak, Satyajit Gupta, Nir Kedem, Igal Levine, Tatyana Bendikov, Gary Hodes and David Cahen. *Cesium Enhances Long-Term Stability of Lead Bromide Perovskite-Based Solar Cells.* J. Phys. Chem. Lett., vol. 7, no. 1, pages 167–172, jan 2016. (Cited on page 81.)
- [Kulkarni 2014] Sneha A. Kulkarni, Tom Baikie, Pablo P. Boix, Natalia Yantara, Nripan Mathews and Subodh Mhaisalkar. *Band-gap tuning of lead halide perovskites using a sequential deposition process.* J. Mater. Chem. A, vol. 2, pages 9221–9225, 2014. (Cited on page 9.)
- [Kunugita 2015] Hideyuki Kunugita, Tsubasa Hashimoto, Yuki Kiyota, Yosuke Udagawa, Yuko Takeoka, Yuiga Nakamura, Junro Sano, Tomonori Matsushita, Takashi Kondo, Tsutomu Miyasaka and Kazuhiro Ema. *Excitonic Feature in Hybrid Perovskite $CH_3NH_3PbBr_3$ Single Crystals.* Chemistry Letters, vol. 44, no. 6, pages 852–854, 2015. (Cited on page 77.)
- [Lampert 1958] Murray A. Lampert. *Mobile and Immobile Effective-Mass-Particle Complexes in Nonmetallic Solids.* Phys. Rev. Lett., vol. 1, pages 450–453, Dec 1958. (Cited on page 6.)

- [Landau 1977] L. D. Landau and E. M. Lifschitz. Quantum mechanics: Non-relativistic theory. course of theoretical physics. vol.3. Pergamon Press, London, 1977. (Cited on page 47.)
- [Lee 2015] Jin-Wook Lee, Deok-Hwan Kim, Hui-Seon Kim, Seung-Woo Seo, Sung Min Cho and Nam-Gyu Park. *Formamidinium and Cesium Hybridization for Photo- and Moisture-Stable Perovskite Solar Cell*. Advanced Energy Materials, vol. 5, no. 20, pages 1501310–n/a, 2015. 1501310. (Cited on page 23.)
- [Leguy 2015] Aurélien M. A. Leguy, Yinghong Hu, Mariano Campoy-Quiles, M. Isabel Alonso, Oliver J. Weber, Pooya Azarhoosh, Mark van Schilfgaarde, Mark T. Weller, Thomas Bein, Jenny Nelson, Pablo Docampo and Piers R. F. Barnes. *Reversible Hydration of $CH_3NH_3PbI_3$ in Films, Single Crystals, and Solar Cells*. Chemistry of Materials, vol. 27, no. 9, pages 3397–3407, may 2015. (Cited on pages 13 and 14.)
- [Leijtens 2015] Tomas Leijtens, Giles E. Eperon, Nakita K. Noel, Severin N. Haberreutinger, Annamaria Petrozza and Henry J. Snaith. *Stability of Metal Halide Perovskite Solar Cells*. Advanced Energy Materials, vol. 5, no. 20, page 1500963, 2015. and other cited there. (Cited on pages 13, 14 and 21.)
- [Li 2016] Dehui Li, Gongming Wang, Hung-Chieh Cheng, Chih-Yen Chen, Hao Wu, Yuan Liu, Yu Huang and Xiangfeng Duan. *Size-dependent phase transition in methylammonium lead iodide perovskite microplate crystals*. Nature Communications, vol. 7, page 11330, apr 2016. (Cited on page 12.)
- [Liang 1970] W Y Liang. *Excitons*. Physics Education, vol. 5, no. 4, page 226, 1970. (Cited on page 4.)
- [Lidzey 2000] David G. Lidzey, Donal D. C. Bradley, Adam Armitage, Steve Walker and Maurice S. Skolnick. *Photon-Mediated Hybridization of Frenkel Excitons in Organic Semiconductor Microcavities*. Science, vol. 288, no. 5471, pages 1620–1623, 2000. (Cited on page 4.)
- [Lin 015] Q. Lin, Ardalan Armin, Ravi Chandra Raju Nagiri, PL. Burn and P. Meredith. *Electro-optics of perovskite solar cells*. Nature Photonics, vol. 9, no. 2, pages 106–112, FEB 2015. (Cited on pages 5 and 45.)
- [Liu 2013] Mingzhen Liu, Michael B. Johnston and Henry J. Snaith. *Efficient planar heterojunction perovskite solar cells by vapour deposition*. Nature, vol. 501, pages 395–398, 2013. (Cited on page 37.)
- [Liu 2015] Jiewei Liu, Sandeep Pathak, Thomas Stergiopoulos, Tomas Leijtens, Konrad Wojciechowski, Stefan Schumann, Nina Kausch-Busies and Henry J. Snaith. *Employing PEDOT as the p-Type Charge Collection Layer in Regular Organic-Inorganic Perovskite Solar Cells*. J. Phys. Chem. Lett., vol. 6, no. 9, pages 1666–1673, may 2015. (Cited on page 13.)

- [LNCMP-team 2004] The LNCMP-team. *The LNCMP: a pulsed-field user-facility in Toulouse*. Physica B: Condensed Matter, vol. 346347, pages 668 – 672, 2004. Proceedings of the 7th International Symposium on Research in High Magnetic Fields. (Cited on page 26.)
- [Mak 2012] Kin Fai Mak, Keliang He, Changgu Lee, Gwan Hyoung Lee, James Hone, Tony F. Heinz and Jie Shan. *Tightly bound trions in monolayer MoS₂*. Nature Materials, vol. 12, no. 3, pages 207–211, dec 2012. (Cited on page 6.)
- [Makado 1986] P C Makado and N C McGill. *Energy levels of a neutral hydrogen-like system in a constant magnetic field of arbitrary strength*. Journal of Physics C: Solid State Physics, vol. 19, no. 6, page 873, 1986. (Cited on pages 49 and 50.)
- [Marco 2016] Nicholas De Marco, Huanping Zhou, Qi Chen, Pengyu Sun, Zonghao Liu, Lei Meng, En-Ping Yao, Yongsheng Liu, Andy Schiffer and Yang Yang. *Guaniidinium: A Route to Enhanced Carrier Lifetime and Open-Circuit Voltage in Hybrid Perovskite Solar Cells*. Nano Letters, vol. 16, no. 2, pages 1009–1016, 2016. PMID: 26790037. (Cited on page 68.)
- [Matteocci 2014] F. Matteocci, S. Razza, F. Di Giacomo, S. Casaluci, G. Mincuzzi, T. M. Brown, A. D'Epifanio, S. Licoccia and A. Di Carlo. *Solid-state solar modules based on mesoscopic organometal halide perovskite: a route towards the up-scaling process*. Phys. Chem. Chem. Phys., vol. 16, pages 3918–3923, 2014. (Cited on page 14.)
- [McMeekin 2016] D. P. McMeekin, G. Sadoughi, W. Rehman, G. E. Eperon, M. Saliba, M. T. Horantner, A. Haghhighirad, N. Sakai, L. Korte, B. Rech, M. B. Johnston, L. M. Herz and H. J. Snaith. *A mixed-cation lead mixed-halide perovskite absorber for tandem solar cells*. Science, vol. 351, no. 6269, pages 151–155, jan 2016. (Cited on pages 20 and 23.)
- [Menéndez-Proupin 2014] E. Menéndez-Proupin, P. Palacios, P. Wahnón and J. C. Conesa. *Self-consistent relativistic band structure of the CH₃NH₃PbI₃ perovskite*. Phys. Rev. B, vol. 90, page 045207, Jul 2014. (Cited on pages 63 and 64.)
- [Mitioglu 2013] A. A. Mitioglu, P. Plochocka, J. N. Jadczak, W. Escoffier, G. L. J. A. Rikken, L. Kulyuk and D. K. Maude. *Optical manipulation of the exciton charge state in single-layer tungsten disulfide*. Phys. Rev. B, vol. 88, page 245403, Dec 2013. (Cited on page 6.)
- [Miyata 2015] Atsuhiko Miyata, Anatolie Mitioglu, Paulina Plochocka, Oliver Portugall, Jacob Tse-Wei Wang, Samuel D. Stranks, Henry J. Snaith and Robin J. Nicholas. *Direct measurement of the exciton binding energy and effective masses for charge carriers in organic-inorganic tri-halide perovskites*.

- Nature Physics, vol. 11, pages 582–587, 2015. (Cited on pages 5, 46, 56, 61, 62, 66 and 96.)
- [Mizusaki 1983] J. Mizusaki, K. Arai and K. Fueki. *Ionic conduction of the perovskite-type halides*. Solid State Ionics, vol. 11, no. 3, pages 203–211, nov 1983. (Cited on page 14.)
- [Møller 1958] C. K. Møller. *Crystal Structure and Photoconductivity of Cæsium Plumbohalides*. Nature, vol. 182, no. 4647, pages 1436–1436, nov 1958. (Cited on pages 81 and 82.)
- [Motta 2015] Carlo Motta, Fedwa El-Mellouhi, Sabre Kais, Nouar Tabet, Fahhad Alharbi and Stefano Sanvito. *Revealing the role of organic cations in hybrid halide perovskite $CH_3NH_3PbI_3$* . Nature Communications, vol. 6, page 7026, apr 2015. (Cited on page 11.)
- [Muto 1958] Toshinosuke Muto, Seiichi Oyama and Hiroshi Okuno. *Electronic Structure of the Exciton in Ionic Crystal*. Progress of Theoretical Physics, vol. 20, no. 6, pages 804–821, dec 1958. (Cited on page 4.)
- [Noel 2014] Nakita K. Noel, Samuel D. Stranks, Antonio Abate, Christian Wehrenfennig, Simone Guarnera, Amir-Abbas Haghhighirad, Aditya Sadhanala, Giles E. Eperon, Sandeep K. Pathak, Michael B. Johnston, Annamaria Petrozzi, Laura M. Herz and Henry J. Snaith. *Lead-free organic-inorganic tin halide perovskites for photovoltaic applications*. Energy Environ. Sci., vol. 7, pages 3061–3068, 2014. (Cited on pages 9 and 14.)
- [Noh 2013] Jun Hong Noh, Sang Hyuk Im, Jin Hyuck Heo, Tarak N. Mandal and Sang Il Seok. *Chemical Management for Colorful, Efficient, and Stable Inorganic-Organic Hybrid Nanostructured Solar Cells*. Nano Letters, vol. 13, no. 4, pages 1764–1769, 2013. PMID: 23517331. (Cited on pages 9 and 22.)
- [Oku 2015] Takeo Oku. *Crystal Structures of $CH_3NH_3PbI_3$ and Related Perovskite Compounds Used for Solar Cells*. In Solar Cells - New Approaches and Reviews. InTech, oct 2015. , and other references cited there. (Cited on pages 11 and 12.)
- [Ong 2015] Khuong P. Ong, Teck Wee Goh, Qiang Xu and Alfred Huan. *Mechanical Origin of the Structural Phase Transition in Methylammonium Lead Iodide $CH_3NH_3PbI_3$* . The Journal of Physical Chemistry Letters, vol. 6, no. 4, pages 681–685, 2015. PMID: 26262485. (Cited on pages 11 and 12.)
- [Onida 2002] Giovanni Onida, Lucia Reining and Angel Rubio. *Electronic excitations: density-functional versus many-body Green's-function approaches*. Rev. Mod. Phys., vol. 74, pages 601–659, Jun 2002. (Cited on page 15.)
- [Onoda-Yamamuro 1990] Noriko Onoda-Yamamuro, Takasuke Matsuo and Hiroshi Suga. *Calorimetric and IR spectroscopic studies of phase transitions in*

- methylammonium trihalogenoplumbates (II)*†. Journal of Physics and Chemistry of Solids, vol. 51, no. 12, pages 1383–1395, jan 1990. (Cited on page 13.)
- [Osherov 2016] Anna Osherov, Eline M. Hutter, Krzysztof Galkowski, Roberto Brenes, Duncan K. Maude, Robin J. Nicholas, Paulina Plochocka, Vladimir Bulović, Tom J. Savenije and Samuel D. Stranks. *The Impact of Phase Retention on the Structural and Optoelectronic Properties of Metal Halide Perovskites*. Advanced Materials, oct 2016. (Cited on page 13.)
- [Pang 2014] Shuping Pang, Hao Hu, Jiliang Zhang, Siliu Lv, Yaming Yu, Feng Wei, Tianshi Qin, Hongxia Xu, Zhihong Liu and Guanglei Cui. *NH₂CH₂NH₂PbI₃ : An Alternative Organolead Iodide Perovskite Sensitizer for Mesoscopic Solar Cells*. Chemistry of Materials, vol. 26, no. 3, pages 1485–1491, feb 2014. (Cited on page 10.)
- [Peierls 1932] R. Peierls. *Zur Theorie der Absorptionsspektren fester Körper*. Annalen der Physik, vol. 405, no. 8, pages 905–952, 1932. (Cited on page 3.)
- [Pelant 2012] Ivan Pelant and Jan Valenta. Luminescence of excitons, chapitre 7, pages 180–182. John Wiley & Sons, Inc., 2012. (Cited on page 6.)
- [Pellet 2014] Norman Pellet, Peng Gao, Giuliano Gregori, Tae-Youl Yang, Mohammad K. Nazeeruddin, Joachim Maier and Michael Grätzel. *Mixed-Organic-Cation Perovskite Photovoltaics for Enhanced Solar-Light Harvesting*. Angewandte Chemie International Edition, vol. 53, no. 12, pages 3151–3157, feb 2014. (Cited on page 22.)
- [Poglitsch 1987] A. Poglitsch and D. Weber. *Dynamic disorder in methylammoniumtrihalogenoplumbates (II) observed by millimeter wave spectroscopy*. The Journal of Chemical Physics, vol. 87, no. 11, pages 6373–6378, 1987. (Cited on pages 65 and 103.)
- [Pollman 1975] J. Pollman and H. Büttner. *Upper bounds for the ground-state energy of the exciton-phonon system*. Solid State Communications, vol. 17, pages 1171–1174, 1975. (Cited on page 65.)
- [Rehman 2015] Waqaas Rehman, Rebecca L. Milot, Giles E. Eperon, Christian Wehrenfennig, Jessica L. Boland, Henry J. Snaith, Michael B. Johnston and Laura M. Herz. *Charge-Carrier Dynamics and Mobilities in Formamidinium Lead Mixed-Halide Perovskites*. Advanced Materials, vol. 27, no. 48, pages 7938–7944, sep 2015. (Cited on page 23.)
- [Sakata 1979] Makoto Sakata, Takashi Nishiwaki and Jimpei Harada. *Neutron Diffraction Study of the Structure of Cubic CsPbBr₃*. Journal of the Physical Society of Japan, vol. 47, no. 1, pages 232–233, jul 1979. (Cited on page 82.)
- [Saliba 2014] Michael Saliba, Kwan Wee Tan, Hiroaki Sai, David T. Moore, Trent Scott, Wei Zhang, Lara A. Estroff, Ulrich Wiesner and Henry J. Snaith.

- Influence of Thermal Processing Protocol upon the Crystallization and Photovoltaic Performance of Organic-Inorganic Lead Trihalide Perovskites.* The Journal of Physical Chemistry C, vol. 118, no. 30, pages 17171–17177, 2014. (Cited on page 36.)
- [Saliba 2016a] Michael Saliba, Taisuke Matsui, Konrad Domanski, Ji-Youn Seo, Amita Ummadisingu, Shaik M. Zakeeruddin, Juan-Pablo Correa-Baena, Wolfgang R. Tress, Antonio Abate, Anders Hagfeldt and Michael Grätzel. *Incorporation of rubidium cations into perovskite solar cells improves photovoltaic performance.* Science, 2016. (Cited on page 23.)
- [Saliba 2016b] Michael Saliba, Taisuke Matsui, Ji-Youn Seo, Konrad Domanski, Juan-Pablo Correa-Baena, Mohammad Khaja Nazeeruddin, Shaik M. Zakeeruddin, Wolfgang Tress, Antonio Abate, Anders Hagfeldt and Michael Gratzel. *Cesium-containing triple cation perovskite solar cells: improved stability, reproducibility and high efficiency.* Energy Environ. Sci., vol. 9, pages 1989–1997, 2016. (Cited on pages 19, 22 and 23.)
- [Saliba 2016c] Michael Saliba, Simonetta Orlandi, Taisuke Matsui, Sadig Aghazada, Marco Cavazzini, Juan-Pablo Correa-Baena, Peng Gao, Rosario Scopelliti, Edoardo Mosconi, Klaus-Hermann Dahmen, Filippo De Angelis, Antonio Abate, Anders Hagfeldt, Gianluca Pozzi, Michael Graetzel and Mohammad Khaja Nazeeruddin. *A molecularly engineered hole-transporting material for efficient perovskite solar cells.* Nature Energy, vol. 1, no. 2, page 15017, jan 2016. (Cited on page 22.)
- [Selinsky 2013] Rachel S. Selinsky, Qi Ding, Matthew S. Faber, John C. Wright and Song Jin. *Quantum dot nanoscale heterostructures for solar energy conversion.* Chem. Soc. Rev., vol. 42, pages 2963–2985, 2013. (Cited on page 19.)
- [Shah 1999] A. Shah, P. Torres, R. Tscharner, N. Wyrsch and H. Keppner. *Photovoltaic Technology: The Case for Thin-Film Solar Cells.* Science, vol. 285, no. 5428, pages 692–698, 1999. (Cited on page 20.)
- [Shaw 2008] Paul Edward Shaw, Arvydas Ruseckas and Ifor David William Samuel. *Exciton diffusion measurements in poly(3-hexylthiophene).* Advanced Materials, vol. 20, no. 18, pages 3516–3520, 9 2008. (Cited on page 19.)
- [Shi 2015] Dong Shi, Valerio Adinolfi, Riccardo Comin, Mingjian Yuan, Erkki Alarousu, Andrei Buin, Yin Chen, Sjoerd Hoogland, Alexander Rothenberger, Khabiboulakh Katsiev, Yaroslav Losovyj, Xin Zhang, Peter A. Dowben, Omar F. Mohammed, Edward H. Sargent and Osman M. Bakr. *Low trap-state density and long carrier diffusion in organolead trihalide perovskite single crystals.* Science, vol. 347, no. 6221, pages 519–522, 2015. (Cited on pages 18 and 20.)

- [Shkrob 2014] Ilya A. Shkrob and Timothy W. Marin. *Charge Trapping in Photovoltaically Active Perovskites and Related Halogenoplumbate Compounds*. J. Phys. Chem. Lett., vol. 5, no. 7, pages 1066–1071, apr 2014. (Cited on page 20.)
- [Shockley 1961] William Shockley and Hans J. Queisser. *Detailed Balance Limit of Efficiency of "p-n" Junction Solar Cells*. Journal of Applied Physics, vol. 32, no. 3, pages 510–519, 1961. (Cited on page 20.)
- [Singh 2016] Shivam Singh, Cheng Li, Fabian Panzer, K. L. Narasimhan, Anna Graeser, Tanaji P. Gujar, Anna Köhler, Mukundan Thelakkat, Sven Huettnner and Dinesh Kabra. *Effect of Thermal and Structural Disorder on the Electronic Structure of Hybrid Perovskite Semiconductor $CH_3NH_3PbI_3$* . J. Phys. Chem. Lett., vol. 7, no. 15, pages 3014–3021, aug 2016. (Cited on page 16.)
- [Sivaram 2015] Varun Sivaram, Samuel D. Stranks and Henry J. Snaith. *Outshining Silicon*. Sci Am, vol. 313, no. 1, pages 54–59, jun 2015. (Cited on page 20.)
- [Soufiani 2015] Arman Mahboubi Soufiani, Fuzhi Huang, Peter Reece, Rui Sheng, Anita Ho-Baillie and Martin A. Green. *Polaronic exciton binding energy in iodide and bromide organic-inorganic lead halide perovskites*. Applied Physics Letters, vol. 107, no. 23, 2015. (Cited on page 66.)
- [Spencer 2004] K. Spencer, F. Lecouturier, L. Thilly and J.D. Embury. *Established and Emerging Materials for use as High-Field Magnet Conductors*. Advanced Engineering Materials, vol. 6, no. 5, pages 290–297, 2004. (Cited on page 28.)
- [Stoumpos 2013] Constantinos C. Stoumpos, Christos D. Malliakas and Mercouri G. Kanatzidis. *Semiconducting Tin and Lead Iodide Perovskites with Organic Cations: Phase Transitions, High Mobilities, and Near-Infrared Photoluminescent Properties*. Inorganic Chemistry, vol. 52, no. 15, pages 9019–9038, 2013. PMID: 23834108. (Cited on pages 13 and 18.)
- [Stranks 2013] Samuel D. Stranks, Giles E. Eperon, Giulia Grancini, Christopher Menelaou, Marcelo J. P. Alcocer, Tomas Leijtens, Laura M. Herz, Annamaria Petrozza and Henry J. Snaith. *Electron-Hole Diffusion Lengths Exceeding 1 Micrometer in an Organometal Trihalide Perovskite Absorber*. Science, vol. 342, no. 6156, pages 341–344, 2013. (Cited on pages 17, 18, 19, 35, 36, 74 and 94.)
- [Stranks 2015] Samuel D. Stranks, Pabitra K. Nayak, Wei Zhang, Thomas Stergiopoulos and Henry J. Snaith. *Formation of Thin Films of OrganicInorganic Perovskites for High-Efficiency Solar Cells*. Angewandte Chemie International Edition, vol. 54, no. 11, pages 3240–3248, 2015. (Cited on page 37.)
- [Suarez 2014] Belen Suarez, Victoria Gonzalez-Pedro, Teresa S. Ripolles, Rafael S. Sanchez, Luis Otero and Ivan Mora-Sero. *Recombination Study of Combined*

- Halides (Cl, Br, I) Perovskite Solar Cells.* The Journal of Physical Chemistry Letters, vol. 5, no. 10, pages 1628–1635, 2014. PMID: 26270357. (Cited on page 9.)
- [Swainson 2003] I.P. Swainson, R.P. Hammond, C. Soullière, O. Knop and W. Massa. *Phase transitions in the perovskite methylammonium lead bromide, $CH_3ND_3PbBr_3$.* Journal of Solid State Chemistry, vol. 176, no. 1, pages 97–104, nov 2003. (Cited on page 13.)
- [Tanaka 2003] Kenichiro Tanaka, Takayuki Takahashi, Takuma Ban, Takashi Kondo, Kazuhito Uchida and Noboru Miura. *Comparative study on the excitons in lead-halide-based perovskite-type crystals $CH_3NH_3PbBr_3$, $CH_3NH_3PbI_3$.* Solid State Communications, vol. 127, no. 910, pages 619 – 623, 2003. (Cited on pages 46, 59 and 64.)
- [Thomas 1977] G.A. Thomas and T.M. Rice. *Trions, molecules and excitons above the Mott density in Ge.* Solid State Communications, vol. 23, no. 6, pages 359–363, aug 1977. (Cited on page 6.)
- [Trots 2008] D.M. Trots and S.V. Myagkota. *High-temperature structural evolution of caesium and rubidium triiodoplumbates.* Journal of Physics and Chemistry of Solids, vol. 69, no. 10, pages 2520–2526, oct 2008. (Cited on page 81.)
- [Uchino 2015] Kenji Uchino. *Glory of piezoelectric perovskites.* Science and Technology of Advanced Materials, vol. 16, no. 4, page 046001, jul 2015. and other references cited there. (Cited on page 6.)
- [Umari 2014] Paolo Umari, Edoardo Mosconi and Filippo De Angelis. *Relativistic GW calculations on $CH_3NH_3PbI_3$ and $CH_3NH_3SnI_3$ Perovskites for Solar Cell Applications.* Scientific Reports, vol. 4, no. 4467, 2014. (Cited on pages 15, 63, 64, 65 and 103.)
- [Umebayashi 2003] T. Umebayashi, K. Asai, T. Kondo and A. Nakao. *Electronic structures of lead iodide based low-dimensional crystals.* Physical Review B, vol. 67, no. 15, apr 2003. (Cited on pages 9 and 15.)
- [Valverde-Chavez 2015] David A. Valverde-Chavez, Carlito S. Poncea, Constantinos C. Stoumpos, Arkady Yartsev, Mercouri G. Kanatzidis, Villy Sundstrom and David G. Cooke. *Intrinsic femtosecond charge generation dynamics in single crystal $CH_3NH_3PbI_3$.* Energy Environ. Sci., vol. 8, pages 3700–3707, 2015. (Cited on page 20.)
- [Vidyasagar 1985] Kanamaluru Vidyasagar, Armin Reller, Jagannatha Gopalakrishnan and C. N. Ramachandra Rao. *Oxygen vacancy ordering in superlattices of the two novel oxides, $La_2Ni_2O_5$ and $La_2Co_2O_5$, prepared by low temperature reduction of the parent perovskites.* J. Chem. Soc., Chem. Commun., pages 7–8, 1985. (Cited on page 8.)

- [Wang 2015a] He Wang, Luisa Whittaker-Brooks and Graham R. Fleming. *Exciton and Free Charge Dynamics of Methylammonium Lead Iodide Perovskites Are Different in the Tetragonal and Orthorhombic Phases.* J. Phys. Chem. C, vol. 119, no. 34, pages 19590–19595, aug 2015. (Cited on pages 12 and 69.)
- [Wang 2015b] Qiong Wang, Miaoqiang Lyu, Meng Zhang, Jung-Ho Yun, Hongjun Chen and Lianzhou Wang. *Transition from the Tetragonal to Cubic Phase of Organohalide Perovskite: The Role of Chlorine in Crystal Formation of $CH_3NH_3PbI_3$ on TiO_2 Substrates.* J. Phys. Chem. Lett., vol. 6, no. 21, pages 4379–4384, nov 2015. (Cited on page 13.)
- [Wang 2015c] Youwei Wang, Yubo Zhang, Peihong Zhang and Wenqing Zhang. *High intrinsic carrier mobility and photon absorption in the perovskite $CH_3NH_3PbI_3$.* Phys. Chem. Chem. Phys., vol. 17, pages 11516–11520, 2015. (Cited on page 19.)
- [Wang 2016] Jacob Tse-Wei Wang, Zhiping Wang, Sandeep Pathak, Wei Zhang, Dane W. deQuilettes, Florencia Wisnivesky-Rocca-Rivarola, Jian Huang, Pabitra K. Nayak, Jay B. Patel, Hanis A. Mohd Yusof, Yana Vaynzof, Rui Zhu, Ivan Ramirez, Jin Zhang, Caterina Ducati, Chris Grovenor, Michael B. Johnston, David S. Ginger, Robin J. Nicholas and Henry J. Snaith. *Efficient perovskite solar cells by metal ion doping.* Energy Environ. Sci., vol. 9, no. 9, pages 2892–2901, 2016. (Cited on page 21.)
- [Wannier 1937] Gregory H. Wannier. *The Structure of Electronic Excitation Levels in Insulating Crystals.* Phys. Rev., vol. 52, pages 191–197, Aug 1937. (Cited on page 3.)
- [Wehrenfennig 2014a] C. Wehrenfennig, M. Liu, H.J. Snaith, M.B. Johnston and L.M. Herz. *Charge carrier dynamics in vapour-deposited films of the organolead halide perovskite $CH_3NH_3PbI_{3-x}Cl_x$.* Energ. Environ. Sci., vol. 7, pages 2269–2275, 2014. (Cited on pages 65 and 103.)
- [Wehrenfennig 2014b] Christian Wehrenfennig, Mingzhen Liu, Henry J. Snaith, Michael B. Johnston and Laura M. Herz. *Charge carrier recombination channels in the low-temperature phase of organic-inorganic lead halide perovskite thin films.* APL Mater., vol. 2, no. 8, 2014. (Cited on page 74.)
- [Weller 2015] Mark T. Weller, Oliver J. Weber, Paul F. Henry, Antonietta M. Di Pumbo and Thomas C. Hansen. *Complete structure and cation orientation in the perovskite photovoltaic methylammonium lead iodide between 100 and 352 K.* Chem. Commun., vol. 51, pages 4180–4183, 2015. (Cited on pages 12 and 13.)
- [wook Park 2015] Byung wook Park, Bertrand Philippe, Sagar M. Jain, Xiaoliang Zhang, Tomas Edvinsson, Håkan Rensmo, Burkhard Zietz and Gerrit Boschloo. *Chemical engineering of methylammonium lead iodide/bromide*

- perovskites: tuning of opto-electronic properties and photovoltaic performance.* J. Mater. Chem. A, vol. 3, no. 43, pages 21760–21771, 2015. (Cited on page 21.)
- [Xiao 2014] Zhengguo Xiao, Cheng Bi, Yuchuan Shao, Qingfeng Dong, Qi Wang, Yongbo Yuan, Chenggong Wang, Yongli Gao and Jinsong Huang. *Efficient, high yield perovskite photovoltaic devices grown by interdiffusion of solution-processed precursor stacking layers.* Energy Environ. Sci., vol. 7, pages 2619–2623, 2014. (Cited on pages 14 and 37.)
- [Xing 2013] Guichuan Xing, Nripan Mathews, Shuangyong Sun, Swee Sien Lim, Yeng Ming Lam, Michael Grätzel, Subodh Mhaisalkar and Tze Chien Sum. *Long-Range Balanced Electron- and Hole-Transport Lengths in Organic-Inorganic $CH_3NH_3PbI_3$.* Science, vol. 342, no. 6156, pages 344–347, 2013. (Cited on pages 18 and 74.)
- [Yamada 2015] Y. Yamada, T. Nakamura, M. Endo, M. Endo, A. Wakamiya and Y. Kanemitsu. *Photoelectronic Responses in Solution-Processed Perovskite $CH_3NH_3PbI_3$ Solar Cells Studied by Photoluminescence and Photoabsorption Spectroscopy.* Photovoltaics, IEEE Journal of, vol. 5, no. 1, pages 401–405, Jan 2015. (Cited on pages 65 and 69.)
- [Yang 2003] Gai Ying Yang, Elizabeth C. Dickey and Clive A. Randall. *Insights into Degradation Mechanisms and Vacancy Ordering in $BaTiO_3$.* Microscopy and Microanalysis, vol. 9, pages 850–851, 8 2003. (Cited on page 8.)
- [Yang 2015] Jinli Yang, Braden D. Siempelkamp, Dianyi Liu and Timothy L. Kelly. *Investigation of $CH_3NH_3PbI_3$ Degradation Rates and Mechanisms in Controlled Humidity Environments Using in Situ Techniques.* ACS Nano, vol. 9, no. 2, pages 1955–1963, feb 2015. (Cited on page 13.)
- [yi Huang 2016] Ling yi Huang and Walter R. L. Lambrecht. *Electronic band structure trends of perovskite halides: Beyond Pb and Sn to Ge and Si.* Phys. Rev. B, vol. 93, no. 19, may 2016. (Cited on page 9.)
- [Yu 2010] M. Yu Peter Y. & Cardona. Fundamentals of semiconductors: Physics and materials properties. Graduate Texts in Physics. Springer Berlin Heidelberg, 2010. (Cited on pages 3, 4, 5 and 6.)
- [Yuan 2015] Yongbo Yuan, Jungseok Chae, Yuchuan Shao, Qi Wang, Zhengguo Xiao, Andrea Centrone and Jinsong Huang. *Photovoltaic Switching Mechanism in Lateral Structure Hybrid Perovskite Solar Cells.* Advanced Energy Materials, vol. 5, no. 15, page 1500615, jun 2015. (Cited on page 14.)
- [Zhang 2015] Huimin Zhang, Chunjun Liang, Yong Zhao, Mengjie Sun, Hong Liu, Jingjing Liang, Dan Li, Fujun Zhang and Zhiqun He. *Dynamic interface charge governing the current–voltage hysteresis in perovskite solar cells.* Phys.

- Chem. Chem. Phys., vol. 17, no. 15, pages 9613–9618, 2015. (Cited on page 14.)
- [Zhao 2015] Yong Zhao, Chunjun Liang, Huimin Zhang, Dan Li, Ding Tian, Guobao Li, Xiping Jing, Wenguan Zhang, Weikang Xiao, Qian Liu, Fujun Zhang and Zhiqun He. *Anomalously large interface charge in polarity-switchable photovoltaic devices: an indication of mobile ions in organic–inorganic halide perovskites*. Energy Environ. Sci., vol. 8, no. 4, pages 1256–1260, 2015. (Cited on page 14.)
- [Zheng 2016] Xiaojia Zheng, Bo Chen, Mengjin Yang, Congcong Wu, Bruce Orler, Robert B. Moore, Kai Zhu and Shashank Priya. *The Controlling Mechanism for Potential Loss in $CH_3NH_3PbBr_3$ Hybrid Solar Cells*. ACS Energy Lett., vol. 1, no. 2, pages 424–430, aug 2016. (Cited on page 22.)
- [Zhou 2014] Huanping Zhou, Qi Chen, Gang Li, Song Luo, Tze-bing Song, Hsin-Sheng Duan, Ziruo Hong, Jingbi You, Yongsheng Liu and Yang Yang. *Interface engineering of highly efficient perovskite solar cells*. Science, vol. 345, no. 6196, pages 542–546, 2014. (Cited on pages 15, 64, 67 and 104.)

